

# **Metal-oxide nanostructures for energy applications**

**A thesis submitted for the degree of  
Doctor of Philosophy**

**Andrea Lamberti**

**Supervisor: Prof. Candido Fabrizio Pirri**



**PhD course in Electronic devices - XXV cycle**

**Politecnico di Torino**

**February 2013**

“[...]fatti non foste a viver come bruti,  
ma per seguir virtute e canoscenza.”

*Dante Alighieri, Divina Commedia, Inferno canto XXVI, 119-120*

“It is not our part to master all the tides of the world, but to do what is in us for the succour of  
those years wherein we are set, uprooting the evil in the fields that we know, so that those who  
live after may have clean earth to till.”

*J.R.R. Tolkien, The Lord of the Rings*

**SELECTION PANEL**  
**for the PhD title in Electron Devices (XXV Cycle)**

Mr LAMBERTI Andrea has defended on 21-2-2013 in the Department of Applied Science and Technology of the Politecnico di Torino, a thesis with the following title: *'Metal-oxide nanostructures for dye-sensitized solar cell application'*

The research object of the dissertation is of high scientific interest.

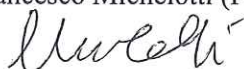
The methodology was assessed as effective.

The research yielded interesting results and showed very good critical thinking skills.

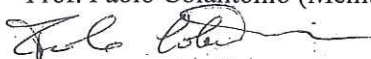
During the interview the candidate showed an excellent knowledge and understanding of the problems dealt with.

The Board unanimously assessed excellent the research work and decided to award the **degree of Research Doctor** to the candidate: LAMBERTI Andrea

Prof. Francesco Michelotti (President)



Prof. Paolo Colantonio (Member)



Prof. Fabrizio Giorgis (Secretary)



Cepia Center  
Torino, II 26 FEB. 2013  


# Acknowledgements

First of all I've to acknowledge the people that more than everyone else have contributed to the success of my PhD: my parents and the woman I love - my wife Luisa.

Special thanks to past and present laboratory members of the CSHR@PoliTO (Italian Institute of Technology).

I am especially grateful to Adriano, for his tireless assistance on our experiments and papers, for all the time spent in obtaining great results with the unique objective: go to a conference!

Appreciations go to the following people for their continuing advice and friendship: Giancarlo, Stefano, Valentina, Rossana, Nadia and Diego; thank you for all the pleasant lunches together and the nice breaks.

Special thanks go to Marzia and Stefano, my tutors, for the confidence and freedom accorded me during the PhD period.

I am also really thankful to Claudio for the clarity that you use to express concepts, scientific and not.

Thank you also to Angelica, Chiole, Ale Ricci and all the people working at the ground and first floor for the friendly environment in which you have welcomed me.

I would like to extend my gratitude to past and present Chilab laboratory (Materials and Microsystems) staff: Matteo, Simone, Denis and Alessandro, all is started here; thanks to you I've learned what a technologist means.

Special thanks go to Davide, the Prince of Panier (or the Red guy of Pont), the person with whom I spent more time dressed in cleanroom clothing illuminated by yellow light.

Special big thanks go to the Materials and Processes for Micro and Nano Technology group of Politecnico di Torino for their friendship and assistance: Monica, Alessandro, Micaela, Diego, Pietro, Giancarlo, Ivan and Max.

I would like to express my sincere gratitude to Prof. Elena Tresso and Prof. Fabrizio Pirri for believing in me.

Last but not least, special thanks go to my friends outside the labs: Gully, Roby, Paul, Giorgia, Bubux, Dani, Edo, Fra, Dav, Ste, Diè, my brother-in-law Davide, Noir, Milly, Mauri, Cava, Valentina, Marta, Marianna, Elena, Stefania, Gloria and Federica, thank you for the laughs, for spending your time in listening and helping me with my ups and downs and for all the pleasant moments spent together.

# Abstract

One of the most important challenges for our society is providing powerful devices for energy conversion and storage. The number of proposed technologies in today's green and renewable energy science is large and still increasing: among all the dye-sensitized solar cells (for energy generation) and Li-ions batteries (for energy storage) have attracted a lot of interest thanks to the easy fabrication processes and the cheap materials involved.

Great attention has been paid on the investigation of one-dimensional metal-oxide nanostructures for a new generation of power sources, because of their unique electronic properties, such as high electron mobility and low carrier recombination rate, high surface-to-volume ratio and excellent surface activity.

Among the large number of semiconductive metal oxide nanostructures,  $\text{TiO}_2$  and  $\text{ZnO}$  are of particular interest due to the fact that they are the best candidates as active materials in electrochemical devices thanks to their chemical and electronic properties.

Several approaches have been proposed for  $\text{TiO}_2$  nanostructure synthesis and among them anodic oxidation is now a well-established technique that can provide large area uniform nanotubular arrays on Ti foil with relatively high specific surface.

Regarding zinc oxide, many papers report on the synthesis of  $\text{ZnO}$  nanostructures performed by means of different techniques. Most of them exploits high temperature processes often using catalyst particles, requires the presence of a sacrificial template, introduces chemical contamination or exhibit slow kinetics.

This PhD thesis investigates the fabrication of different metal-oxide nanostructures and their integration as electrodes into DSCs and LiBs: in particular the work deals with  $\text{TiO}_2$  nanotube arrays obtained by anodic oxidation and with  $\text{ZnO}$  sponge-like films obtained by combined sputtering/thermal oxidation techniques.

Vertically oriented  $\text{TiO}_2$  NTs were obtained by anodic oxidation of titanium foil and fully characterized in terms of stoichiometry, crystalline phase and morphology.  $\text{TiO}_2$  nanotubes were tested both in DSC and in LiBs showing improved charge transport properties due to the 1-dimensional structures and a reduced recombination rate (and a subsequent higher carrier lifetime value) that could be attributed to the reduced presence of defects and trap-sites in the nanotubes with respect to the nanoparticle-based electrodes.

As competitive alternative to  $\text{TiO}_2$  nanotubes, porous  $\text{ZnO}$  films were obtained by a simple two-step method, involving the sputtering deposition of a sponge-like layer of metallic zinc, followed by a low-temperature treatment allowing for the complete oxidation of zinc, thus forming sponge-like  $\text{ZnO}$  films. Also in this case  $\text{ZnO}$  nanostructured films were fully characterized tested both in DSC and in LiBs showing interesting performance. Thanks to the its 3D nanostructuration, the superimposition of small branches able to grow in length almost isotropically and forming a complex topography,  $\text{ZnO}$  sponge-like can combine the fast transport properties of one dimensional material and the needed surface area usually provided by nanocrystalline electrodes.

# Table of Contents

<b>Acknowledgements</b>	i
<b>Abstract</b>	ii
<b>Table of contents</b>	iii
<b>Chapter 1. Introduction</b>	<b>1</b>
<b>1.1 Worldwide energy demand</b>	1
<b>1.2 Devices for energy production and storage</b>	2
1.2.1 <u>Dye-sensitized solar cells</u>	3
1.2.2 <u>Lithium-ions batteries</u>	4
<b>1.3 Nanostructured metal-oxide semiconductors</b>	5
1.3.1 <u>Nanomaterials applications</u>	5
1.3.2 <u>Nanomaterials synthesis and deposition</u>	6
<b>1.4 Objectives and structure of the thesis</b>	9
<b>1.5 References</b>	10
<b>Chapter 2. Electrochemical devices for energy conversion and storage</b>	<b>13</b>
<b>2.1 Dye sensitized solar cells</b>	13
2.1.1 <u>Structure and materials</u>	13
2.1.1.1 <i>Transparent conductive substrates</i>	14
2.1.1.2 <i>Photoanode</i>	15
2.1.1.3 <i>Dyes</i>	15
2.1.1.4 <i>Electrolyte</i>	16
2.1.1.5 <i>Counter electrode</i>	17
2.1.2 <u>Working principles</u>	17
2.1.3 <u>Photovoltaic parameters and characterization techniques</u>	18
2.1.3.1 <i>Current-Voltage measurements</i>	18
2.1.3.2 <i>Incident photons to current conversion efficiency</i>	19
2.1.3.3 <i>Open Circuit Voltage Decay</i>	20
2.1.3.4 <i>Electrochemical Impedance Spectroscopy</i>	21
<b>2.2 Li-ions microbatteries</b>	23
2.2.1 <u>Structure and materials</u>	23
2.2.1.1 <i>Anode</i>	24
2.2.1.2 <i>Cathode</i>	25
2.2.1.3 <i>Separator</i>	25
2.2.1.4 <i>Electrolyte</i>	25
2.2.2 <u>Working principles</u>	27
2.2.3 <u>Battery parameters</u>	28

2.2.4	<u>Characterization techniques</u>	28
<b>2.3</b>	<b>References</b>	29
<b>Chapter 3.</b>	<b>Metal-oxide nanostructures: growth and characterization</b>	<b>31</b>
<b>3.1</b>	<b>Materials and characterizations</b>	31
3.1.1	<u>TiO<sub>2</sub> nanotubes</u>	31
3.1.2	<u>Sponge-like ZnO</u>	31
3.1.3	<u>Characterization techniques</u>	31
<b>3.2</b>	<b>TiO<sub>2</sub> nanotubes</b>	32
3.2.1	<u>Growth mechanism</u>	32
3.2.2	<u>Synthesis procedure</u>	35
3.2.3	<u>Results and discussion</u>	36
3.2.3.1	<i>Field emission scanning electron microscopy</i>	36
3.2.3.2	<i>Energy dispersive X-ray spectrometry</i>	38
3.2.3.3	<i>Surface area analysis</i>	39
3.2.3.4	<i>X-ray diffraction analysis</i>	40
3.2.3.5	<i>Transmission electron microscopy</i>	41
3.2.3.6	<i>UV/Vis measurements</i>	41
3.2.3.7	<i>Contact angle measurements</i>	42
3.2.3.8	<i>Electrical measurements</i>	43
<b>3.3</b>	<b>Sponge-like ZnO</b>	44
3.3.1	<u>Growth process</u>	44
3.3.2	<u>Synthesis procedure</u>	45
3.3.3	<u>Results and discussion</u>	45
3.3.3.1	<i>Field emission scanning electron microscopy</i>	45
3.3.3.2	<i>Energy dispersive X-ray spectrometry</i>	48
3.3.3.3	<i>Surface area analysis</i>	48
3.3.3.4	<i>X-ray diffraction analysis</i>	49
3.3.3.5	<i>Transmission electron microscopy</i>	49
3.3.3.6	<i>UV/Vis measurements</i>	50
3.3.3.7	<i>Contact angle measurements</i>	50
3.3.3.8	<i>Electrical measurements</i>	51
<b>3.4</b>	<b>References</b>	51
<b>Chapter 4.</b>	<b>Technological processes for DSC fabrication and characterization</b>	<b>53</b>
<b>4.1</b>	<b>Microfluidic housing system</b>	53
<b>4.2</b>	<b>Device characterization</b>	55
<b>4.3</b>	<b>TiO<sub>2</sub> based photoanodes</b>	55
4.3.1	Fabrication/Technology	56
4.3.1.1	<u>TiO<sub>2</sub> nanotubes</u>	57
4.3.1.1.1	<i>Nanotubes array detachment and bonding on transparent substrate</i>	58

4.3.1.1.2	<i>TiO<sub>2</sub> nanotubes/nanoparticles composite</i>	59
4.3.2	<u>Evaluation of photovoltaic parameters</u>	60
4.3.2.1	<i>NTs bonding using commercial TiO<sub>2</sub> paste</i>	60
4.3.2.2	<i>Nanotube bonding using homemade TiO<sub>2</sub> sol</i>	63
4.3.2.3	<i>TiO<sub>2</sub> nanotubes/nanoparticles composite</i>	66
4.4	<b>Sponge-like ZnO based photoanodes</b>	69
4.4.1	<u>Evaluation of photovoltaic behavior</u>	69
4.4.1.1	<i>Immersion time</i>	70
4.4.1.2	<i>Effect of PH</i>	72
4.4.1.3	<i>ZnO thickness</i>	73
4.5	<b>References</b>	76
<b>Chapter 5. Technological process for Li-Ions batteries fabrication and characterization</b>		<b>78</b>
5.1	<b>Cell components and assembling</b>	78
5.2	<b>Device characterization</b>	79
5.3	<b>Anodes fabrication</b>	79
5.3.1	<u>TiO<sub>2</sub> nanotubes</u>	79
5.3.2	<u>Sponge-like ZnO</u>	80
5.4	<b>Results and discussion</b>	81
5.4.1	<u>TiO<sub>2</sub> nanotubes</u>	81
5.4.2	<u>Sponge-like ZnO</u>	88
5.5	<b>References</b>	91
<b>Chapter 6. Conclusions and consideration for future work</b>		<b>92</b>
6.1	<b>Metal-oxide nanostructures</b>	92
6.1.1	<u>TiO<sub>2</sub> nanotubes array</u>	92
6.1.2	<u>ZnO Sponge-like</u>	93
6.2	<b>Dye sensitized solar cells</b>	93
6.2.1	<u>TiO<sub>2</sub> nanotubes array</u>	93
6.2.2	<u>ZnO Sponge-like</u>	94
6.3	<b>Li-Ions batteries</b>	94
6.3.1	<u>TiO<sub>2</sub> nanotubes array</u>	94
6.3.2	<u>ZnO Sponge-like</u>	95
6.4	<b>List of publications related with this research project</b>	95



# Chapter 1

## Introduction

In this introductive Chapter information on devices for energy production and storage and on nanostructured metal-oxide semiconductors is provided together with a description of the structure and the targets of the work. To clarify the scenario in which this work is contextualized an overview on the worldwide energy demand is reported.

### 1.1 Worldwide energy demand

“Perhaps the largest challenge for our global society is to find ways to replace the slowly but inevitably vanishing fossil fuel supplies by renewable resources [...]” [1].

With these words Micheal Graetzel, professor at the École Polytechnique Fédérale de Lausanne and inventor of the dye-sensitized solar cell, deals with the worldwide energy situation. The need for power is nowadays mainly satisfied by the use of conventional energy sources based on oil, coal, natural gas and nuclear power that have proven to be highly effective drivers of economic progress. Unfortunately the environmental impact of most of these energy sources is tremendous, mainly because of the emission of greenhouse gases, which causes the increase in the global averaged temperature affecting the equilibrium in all the ecosystems.

Moreover, the worldwide power consumption (whose 2011 data are reported in Figure 1) is expected to double in the next 3 decades because of the increase in world population and the rising demand of energy in the developing countries, leading to an expected planetary emergency of gigantic dimensions.

In this panorama the potential impact of renewable energy sources is enormous as they can in principle meet many times the world’s energy demand providing sustainable energy services based on the use of routinely available, indigenous resources. A transition to renewable energy systems is likely as the costs of solar and wind power systems have dropped substantially in the past 30 years, and continue to decline, while the price of oil and gas continues to fluctuate.

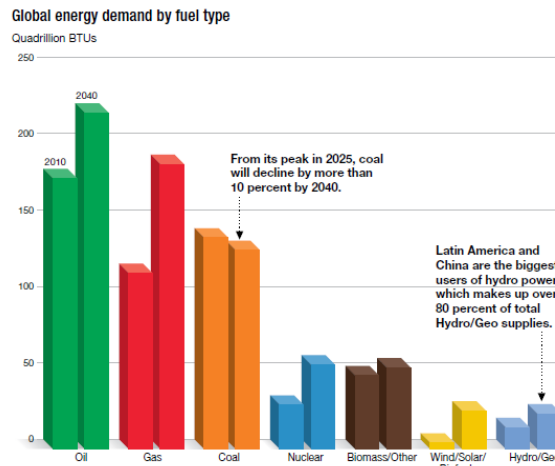


**Figure 1.1** Global energy demand [2]

## 1.2 Devices for energy production and storage

The traditional approach to energy supply is based on the generation of huge amounts of energy in localized production sites and its following delivery for minute use: this causes significant losses across the distribution net. Typical examples of this approach are petroleum and coal industry, nuclear power stations, hydroelectric dams, wind farms, and geothermal power installations. However, for a huge class of applications, like mobile systems, low power electronic devices or for use in rural area where the electric net is not available, it is always more interesting to supply a localized energy production. Therefore, the centralized production of high quantities of energy can successfully be accompanied by a distributed system of energetic hot spots, able to produce very low amounts of energy, with high spatial density.

Recent studies have revealed that widespread adoption of distributed generation technologies in power systems can play a key role in creating a clean, reliable energy with substantial environmental and other benefits [3].

A huge interest lies in the development of energy harvesting systems able to gather low amount of energy which is usually not collected or dispersed, like for instance in building integrated solar facades or smart windows. In such case, the efficiency of the single energy harvester still remains a crucial point, but other aspects gain importance, such as flexibility, integration in complex systems, and even aesthetics.

Two complementary strategies can be considered to manage energy in energy supply systems. A first class of devices, as batteries, fuel cells, and supercapacitors, need a finite quantity or a continuous supply of an active material or fuel to properly work. Devices of this kind can be classified as non-regenerative power supplies. A second class of tools, as photovoltaic cells, mechanical harvesters, and thermoelectric devices, do not need any material or fuel to work and can be classified as regenerative devices. Fig. 1.2 illustrates the technologies that can support distributed energy resources systems.

The number of proposed devices is large, and still increasing: among all the dye-sensitized solar cells (for energy generation) and Li-ions batteries (for energy storage) have attracted a lot of attention thanks to the easy fabrication processes, the cheap materials involved and the possibility to play an important role in the above mentioned application fields.

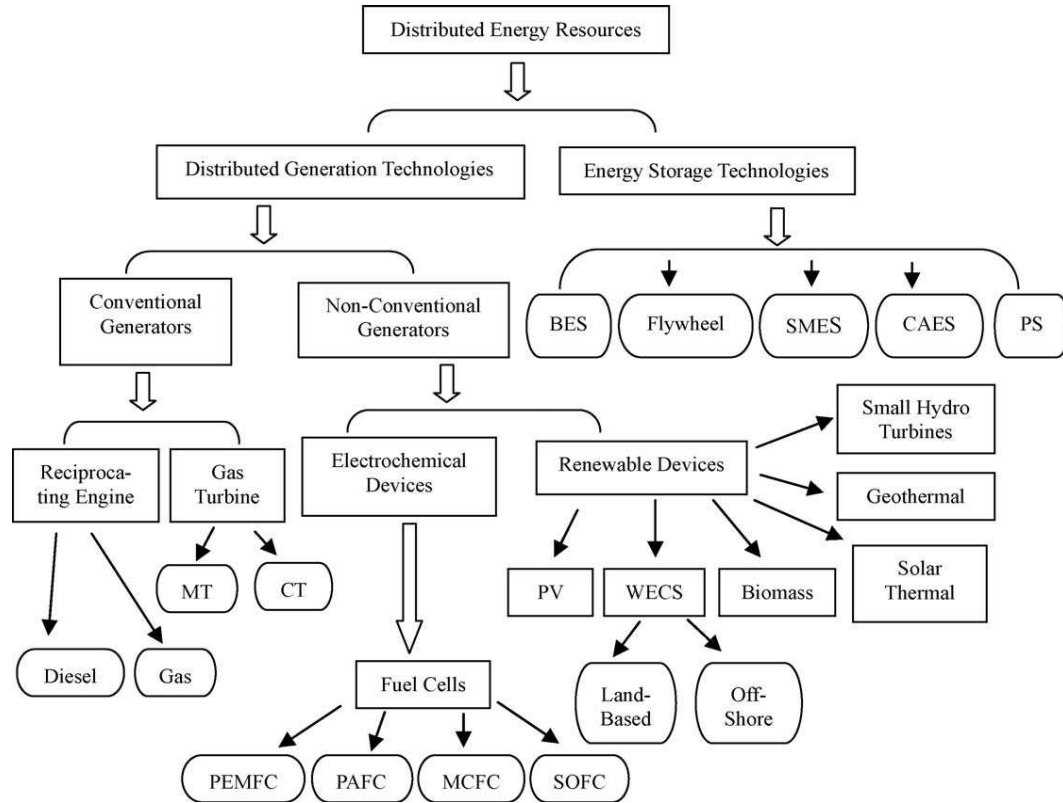


**Figure 1.2** Distributed energy resources technologies [3]

### 1.2.1 Dye-sensitized solar cells

Dye-sensitized Solar Cells (DSCs) have received considerable attention since the original work of O'Regan and Grätzel in 1991, as a cheap and effective alternative for a new generation of photovoltaic devices [4]. The major benefits lie in the materials and the technologies needed for DSCs production, such as low temperature and atmospheric pressure based manufacturing processes, making them compatible with roll-to-roll mass production [5]. Moreover DSCs work effectively even in diffuse light conditions being suitable for indoor application [6].

The standard DSC structure consists of a  $\text{TiO}_2$  nanocrystalline layer deposited on a transparent conducting oxide (TCO) covered glass, a ruthenium complex dye, an electrolytic solution containing an iodide/tri-iodide ( $\text{I}/\text{I}_3^-$ ) redox couple and a Pt-covered counter electrode. The light-to-electricity conversion mechanism starts with the adsorption of visible light by means

of the sensitizer molecules; photoexcited electrons are injected from the dye into the conduction band of the semiconductor and collected at the anode. The ground state of the dye is reinstated by electron donation from the electrolyte, while the holes are transported to the cathode where the Pt layer acts as catalyst for reduction of triiodide. The state of the art overall energy conversion efficiency under AM 1.5 sun light ( $100 \text{ mW/cm}^2$ ) is higher than 11% for such system [7] and exceeds 12% employing a porphyrin dye and Co-based redox shuttle [8]. Although  $\text{TiO}_2$  nanoparticles (NPs) can provide remarkable harvesting properties thanks to the high surface area for dye loading, the electron path to reach the conducting substrate is longer if compared to low-dimensional system, with a higher chance of interfacial losses [9,10]. For this reason great attention has been paid on the investigation of one-dimensional metal-oxide nanostructures for a new generation of power sources, because of their unique electronic properties, such as high electron mobility and low carrier recombination rate, high surface-to-volume ratio and excellent surface activity [11, 12].

Zinc oxide is a promising material for the fabrication of DSC photoanodes. Is it possible to easily grow a great number of one-dimensional ZnO nanostructures like nanowires or nanorods [13] or more complicated three-dimensional structures such as branched and dendritic nanowires [14-15]. At present, the photoconversion efficiencies of ZnO-based DSCs are below 8% [16], so the suggestion of new structures and/or architectures aimed at the improvement of the cell performances is an exciting challenge.

### 1.2.2 Lithium ions batteries

Lithium-ion batteries (LiBs) are one of the great successes of modern materials electrochemistry. Pioneer work with the lithium battery began in 1912 under G.N. Lewis but it was not until the early 1970s when the first non-rechargeable lithium batteries became commercially available. Lithium is the lightest of all metals, has the greatest electrochemical potential and provides the largest energy density for weight. Attempts to develop rechargeable lithium batteries failed due to safety problems. Because of the inherent instability of lithium metal, especially during charging, research shifted to a non-metallic lithium battery using lithium ions [17]. Although slightly lower in energy density than lithium metal, lithium-ion is safe. In 1991, the Sony Corporation commercialized the first lithium-ion battery.

A lithium-ion battery consists of a lithium-ion intercalation negative electrode (generally graphite), and a lithium-ion intercalation positive electrode (generally the lithium metal oxide,  $\text{LiCoO}_2$ ), these being separated by a lithium-ion conducting electrolyte, for example a solution of  $\text{LiPF}_6$  in ethylene carbonate-diethylcarbonate [18]. Although such batteries are commercially successful, a further increase of the already reached performances is unlikely using the current electrode and electrolyte materials. Battery discharge is based on the diffusion of lithium ions from the anode to the cathode through the current collector. This moving mechanism is primarily based on diffusion processes: delivering lithium ions to the surface of the anode, transitioning to and diffusion through the electrolyte, and transitioning to and diffusion into the cathode. Diffusion is the most limiting factor in high-current discharge and charge as well as in low temperature performance. In addition, the intercalation and

deintercalation processes create a volume change in the active electrode materials. This repeated process due to cycling can initiate cracks and can lead to eventual fracture with the result of unusable active electrode material due to disconnection to the current collector [19]. Efforts in materials processing and manufacturing to increase performance and to manage unavoidable volume change have been leading toward nanostructured materials. Nanostructures can accommodate volume change with minimal risk of crack initiation, and their nano-scaled morphology results in minimal diffusion path lengths [19]. A strong focus is on packing density to maximize active material content, open porosity to access the electrolyte, and electronic continuity to guarantee charge exchange to the current collectors.

### **1.3 Nanostructured Metal Oxide semiconductors**

Almost all the energy devices presented in the previous section are limited in their performances by the properties of the employed materials. The most used semiconductors for photovoltaic cells are in fact characterized by poor carrier transport properties and narrow absorption wavelength range which limit the energy-conversion efficiency. Concerning the second class of devices (batteries, supercapacitors, and fuel cells) they present insufficient energy/power densities mainly due to the poor charge-and mass-transport properties and to the required expensive and complicated production processes. For this reason nanostructured materials are of great interest: they are expected to have a great impact in the fields of semiconductors, energy and environment.

#### **1.3.1 Nanomaterials applications**

Nanomaterials (materials with characteristic dimensions at the nanometer scale) are able to show completely different properties from conventional bulk ones. The field of energy is one of the most suitable to exploit the unique properties of these materials. Among the inorganic semiconductor materials, nanostructured metal-oxide semiconductors have recently invaded the scientific activity related to devices for energy production and storage, such as third-generation photovoltaic cells and lithium-batteries. These materials can overcome the limitation imposed by the relatively poor properties of the standard electrodes, showing high carrier mobility and significantly low charge recombination rates.

Metal-oxide nanostructures are the focus of current research efforts in nanotechnology since they are the most common minerals on the Earth thanks to their special shapes, compositions, and chemical, and physical properties [20]. They have now been widely used in the design of energy saving and harvesting devices such as Lithium ion batteries [21, 22], fuel cells [23, 24], solar cells [25, 26], and even transistors/FETs [27, 28], Light emitting devices (LEDs) [29-30], hydrogen production by water photolysis and its storage [31, 32], water and air purification by degradation of organic/inorganic pollutants [33, 34], environmental monitoring by their applications in the fabrication of gas, humidity and temperature sensors [35, 36] and photodetectors [37]. Nevertheless they have also applications in biological and medical sciences such as drug delivery, fluorescent imaging and bio labeling [38, 39]. Oxides of

transition metals have strong ferromagnetism properties with high Curie temperature and are used as magnetic read, write heads and data storage devices [40]. Transition metal doped active oxides such as ZnO, CuO, TiO<sub>2</sub>, Al<sub>2</sub>O<sub>3</sub> [41] are called diluted magnetic semiconductors and are applicable in the fabrication of spin based electronic devices. SnO<sub>2</sub> nanomaterials are regarded as one of the most important sensor materials for detecting leakage of several inflammable gases owing to their high sensitivity to low gas concentrations [42]. Indium-doped tin oxide (In:SnO<sub>2</sub>, ITO) film is an ideal material for flat panel displays because of its high electrical conductivity and high optical transparency [43], and ZnO is regarded as an ideal alternative material for ITO because of its lower cost and easier etchability [44].

Besides the great application potential, oxide-based nanomaterials such as ZnO and TiO<sub>2</sub> have recently revolutionized the nanomaterials research because of the availability of soft chemical synthesis.

The application of semiconductor oxide nanomaterials into the dye sensitized solar cells structure could lead to several advantages optimizing the mesoporous active layers and demonstrating the possibility to achieve high solar conversion efficiency. However, the attainment of sufficiently high efficiency values is still limited by consistent losses during photoinduced charge separation and charge transport across the electrode.

An important problem related to energy storage is the one of consumed batteries and accumulators. Also in this case the implementation of nanomaterials could help improving the device performances. For example MO nanostructure could significantly increase the specific capacity of traditional Li-ion batteries reducing the possibility of batteries catching fire.

### 1.3.2 Nanomaterials synthesis and deposition

Nanostructured metal oxide semiconductors can be deposited on any type of substrates such as metals, semiconductors, polymers, and flexible plastics unlike other III-V semiconductor and silicon, which requires specific and costly substrates.

All these metal-oxide materials can be produced in different shapes (such as nanowires, nanobelts, nanorods, nanotubes, nanocombs, nanorings, nanohelices/nanosprings, nanocages and nanosheets and nanostars [13-15, 45]) depending on the synthesis routes, which can range over a wide variety of techniques.

The methods usually employed for metal-oxide film deposition can be divided into two groups based on the nature of the deposition process. The physical methods include pulsed laser deposition (PLD), molecular beam epitaxy (MBE), and sputtering. The chemical methods comprise gas phase deposition methods and solution techniques. The gas phase methods are chemical vapor deposition (CVD), metal organic chemical vapor deposition (MOCVD) and atomic layer deposition (ALD), while spray pyrolysis, sol-gel, spin- and dip-coating methods employ precursor solutions.

Each method has certain advantages and disadvantages on issues ranging from ease of use to operating expense to time required for growth to quantity and quality of material produced.

In molecular beam epitaxy (MBE) [46], atomic or molecular beams are directly deposited onto a substrate in an ultrahigh vacuum (UHV) system ( $\leq 10^{-9}$  Torr). In MBE, thin films grow by

reactions between thermal-energy molecular or atomic beams of the constituent elements and a substrate surface, which can be maintained at a different temperature. The composition of the deposited film depends on the relative arrival rates of the constituent elements, which consequently depend on the evaporation rates and sticking coefficient of the appropriate materials. The growth rate is typically 1 monolayer/s ( $2\sim 3\text{\AA}/\text{s}$ ) [75], which is low enough to ensure surface movement of the impinging species on the growing surface and can result in very smooth and uniform film.

Sputter deposition [47] is another common method of metal oxide film deposition. It involves bombardment of a target (metal or metal-oxide) with a plasma (usually a noble gas, such as Argon). The relatively low target temperature makes sputtering one of the most flexible deposition techniques. The sputtered atoms ejected into the gas phase, are not in their thermodynamic equilibrium state, so they tend to condense back into the solid phase on the substrate surface. It is a good method for depositing smooth, uniform films that exhibit good adhesion to the growing substrate. Film growth rate is well controllable allowing the reproducibility of the samples thickness. Growth rate are also high and comparable to evaporation techniques. RF sputtering is considered to be a relatively low-cost, low maintenance and effective process.

Pulsed laser deposition [48] has been established as a versatile technique for the generation of nanoparticles and thin films of oxides. Similar to RF sputtering, pulsed laser deposition uses a pulsed laser beam to impinge on a target in order to deposit desired material as thin films. A high vacuum chamber is commonly necessary for the processing. Pulses of focused laser light transform the target material directly from solid to plasma. An expansion cools the plasma and it reverts to a gas that is carried to the substrate, where it condenses to a solid state and the growth happens. The crystal structure and orientation of films grown by PLD are highly dependent on thermodynamic stability. In PLD, the precise control of the processing parameters (such as species fluxes) is also difficult to realize, which is helpful for understanding the nucleation and growth mechanisms of thin films.

In chemical vapor deposition (CVD) [49], one or more precursors, usually activated by temperature, react at a substrate to form a film. To deposit pure films by CVD method there are strict requirements for the precursor. The molecules must have a vapor pressure high enough to be transported to the reaction chamber, but yet they must have a high thermal stability to prevent particles formation in the gas phase. In this method, controllable film growth rate and smooth films are attainable. Significant drawbacks include high cost and high temperatures for many materials.

MOCVD [50] is a growth method especially suited for compound semiconductors that rely on the surface reaction of organic or metal-organic compounds and metal hydrides containing the required chemical elements. Formation of the epitaxial layer occurs by final pyrolysis of the constituent chemicals at the substrate surface, i.e. requires relatively high growth temperatures. In contrast to PLD or MBE processes, MOCVD growth is driven by chemical reactions and takes place in the gas phase at moderate pressures under near-equilibrium conditions. This powerful and inexpensive technique has been developed mainly for the production of highly stoichiometric materials of virtually all III/V semiconductor compounds

but it has also been successfully used for the growth of other semiconductor materials such as complex oxides.

Atomic Layer Deposition (ALD) [51], also known as atomic layer epitaxy (ALE) or atomic layer chemical vapor deposition (ALCVD), is a chemical gas phase deposition technique developed in Finland in the 1970's by T. Suntola. In ALD the reactant gases are separately introduced to the substrates and growth is achieved through self-limiting surface reactions. This results in the high uniformity and an excellent thickness control for which the ALD technique is known, enabling deposition of very thin films with a uniform thickness. The ALD technique allows to deposit a wide variety of compounds such as oxides, nitrides and sulphides, as well as pure elements, mostly metals. Furthermore, using the ALD technique, reactant species are enabled to reach into open cavities and evenly cover complicated structures.

Spray pyrolysis [52] is a processing technique to prepare dense and porous oxide films, ceramic coatings, and powders. Unlike many other film deposition techniques, spray pyrolysis represents a very simple and relatively cost-effective method, especially regarding equipment cost. Spray pyrolysis does not require high quality substrates or chemicals. The method has been employed for the deposition of dense films, porous films, and for powder production. Even multi-layered films can be easily prepared using this versatile technique. Typical spray pyrolysis equipment consists of an atomizer, precursor solution, substrate heater, and temperature controller.

The sol-gel process [53] is a good method for the deposition of pure, homogeneous metal-oxide films. A sol is a colloidal suspension of particles in a liquid. The sol undergoes a sol-gel transition to a rigid two component system of solid and solvent, followed by removal of the solvent. In a typical sol-gel process, the precursor undergoes a series of hydrolysis and polymerization reactions to form a colloidal suspension. Then the particles condense in a new phase, the gel, which is a solid macromolecule immersed in a solvent. To obtain a film, the sol can be spin or dip coated onto a substrate. The desired film thickness is obtained by repeating the process. After the "gel" film is crystallized, the substrate and film are placed in a furnace to be annealed.

Hydrothermal processing [54] can be defined as any heterogeneous reaction in an aqueous solvent (or non-aqueous solvent for solvo-thermal processing) under high pressure and temperature conditions, which induces the dissolution and re-crystallization of materials that are relatively insoluble under ordinary conditions. In the context of nanotechnology, the hydrothermal technique provides an ideal method for producing 'designer particulates', i.e. mono-dispersed particles with high purity, high crystallinity and controlled physicochemical characteristics.

Electrodeposition [55] is a simple method for achieving high quality films at low temperatures and low production cost. In an electrodeposition process, ions are moved through a solution by an electric field to coat an electrode. The simplest form of an electrochemical cell is performed using a 2-electrode system, consisting of a cathode and an anode. In the 2-electrode system, the voltage is measured between these two electrodes, and the current is measured anywhere in the circuit. Research has deepened the understanding of the deposition processes

and electrochemical deposition today provides many exciting routes for the synthesis of metal oxides, alloys and nanostructured materials. Fundamental aspects of electrochemical deposition include the heterogeneous electron transfer step between the electrode and the electroactive species present in the solution as well as the transition of the discharged metal atoms into the crystalline state. The deposition is inexpensive and fast. The deposition of metal oxides from aqueous solutions is mainly performed in alkaline solutions containing metal complexes. Electrochemical deposition of metal oxides can be carried out under oxidizing conditions as well as reducing conditions from alkaline solutions. In both cases, the metal ion dissociates from the complex and precipitates on the electrode as the oxide. What controls the ability to deposit an oxide is the stability of that oxide under the experimental conditions, i.e. the potential, temperature and pH.

Anodic oxidation [56] is the process of forming an oxide ( $M_xO_y$ ) on a metal surface by applying an electrical current or potential through a cell containing a suitable electrolyte. The metals that can be anodized belong to the so-called valve-metals group. The main feature of the metals is the ability to form a highly resistant protective oxide film that grows when an electric field is applied. The characteristics of a layer treated with anodic oxidation can vary according to the type and concentration of the electrolytes as well as the processing variables used during anodic oxidation. Compared with other synthesis approaches, electrochemical anodization is a simple and convenient technique to fabricate uniform layers of vertically self-oriented nanostructures.

## 1.4 Targets and Structure of the thesis

This PhD thesis investigates the fabrication of different metal oxide nanostructures and their integration as electrodes into DSCs and LiBs: in particular the thesis deals with  $TiO_2$  nanotube arrays obtained by anodic oxidation and with ZnO sponge-like films obtained by combined sputtering/thermal oxidation techniques.

The  $TiO_2$  nanotube-based photoanodes for dye sensitized solar cells can be fabricated directly using the NTs film on opaque Ti foil, with a cell backside illumination, but in that configuration, the number of photons that can reach the active part of the cell is reduced. An alternative is based on nanotubes derived from thin films deposited on transparent conductive substrate that can overcome this drawback but in that case it is difficult to obtain long NT arrays starting from thin Ti layers. A new and valuable approach is proposed and followed in this work: it consists in the fabrication of self-standing  $TiO_2$  NT membranes that can be transferred to transparent conductive sheets employing a bonding interlayer.

Zinc oxide is well known as a promising alternative to titanium dioxide for the fabrication of photoanodes in DSCs. With respect to titania, ZnO presents higher electron mobility and carrier lifetime, being these parameters very important to improve the performances of DSCs. In this work a novel method for the synthesis of porous nanocrystalline layers of ZnO will be presented.

Therefore, the first objective of this work is devoted to the efficient synthesis of  $TiO_2$  NT membranes and ZnO sponge-like film on transparent conductive glasses in view of the

evaluation of DSCs performances when these films are employed for the photoanode fabrication.

Nowadays research efforts for anode materials of lithium ion batteries have been focused on the safety and capacity retention: the metal-oxide nanostructures can work well also into LiBs. Thus the second objective of this work is to integrate the developed nanostructured materials as electrodes into LiBs.

This thesis aims to provide readers an overview on electrochemical device for energy production and storage, focusing the attention on the experimental fabrication and characterization of alternative electrode morphology and materials for DSCs and LiBs.

The manuscript is divided in 6 Chapters: Chapter 1 provides introductive information on energy production and storage devices and nanostructured metal-oxide semiconductors and describes the objectives and the structure of this work; Chapter 2 presents the detailed description of the two devices investigated in this work, i.e. DSCs and LiBs, focusing the attention on the different components and the working principles. The experimental part starts with Chapter 3, which presents the synthesis and the material characterization of TiO<sub>2</sub> nanotube array by anodic oxidation and ZnO sponge-like films by combined sputtering/thermal oxidation techniques. Chapter 4 and Chapter 5 describe the technological approaches and the results of the characterization of metal-oxide nanostructures integrated into DSCs and LiBs respectively. Finally, Chapter 6 provides the concluding remarks and outlooks of this PhD thesis.

This work is the result of collaboration among the “Center for Space Human Robotics IIT@PoliTo” of Istituto Italiano di Tecnologia, the “Applied Science and Technology Department” of Politecnico di Torino and “Electronics and Telecommunications Department” of Politecnico di Torino.

## 1.5 References

- [1] M. Grätzel. *Acc. Chem. Res.*, 42 (2009) 1788.
- [2] [exxonmobil.com/energyoutlook](http://exxonmobil.com/energyoutlook): Outlook for Energy: A View to 2040.
- [3] M. F. Akorede, H. Hizam, E. Pouresmaeil. *Renew. Sust. Energ. Rev.* 14 (2010) 724.
- [4] A. Hagfeldt, M. Grätzel. *Acc. Chem. Res.* 33 (2000) 269.
- [5] G. Hashmi, K. Miettunen, T. Peltola, J. Halme, I. Asghar, K. Aitola, M. Toivola, P. Lund. *Renew. Sust. Energ. Rev.* 15 (2011) 3717.
- [6] A. Sacco, L. Rolle, L. Scaltrito, E. Tresso, C.F. Pirri. *Appl. Energ.* (2012) DOI 10.1016/j.apenergy.2012.07.001.
- [7] M. K. Nazeeruddin, F. De Angelis, S. Fantacci, A. Selloni, G. Viscardi, P. Liska, S. Ito, B. Takeru and M. Graetzel. *J. Am. Chem. Soc.* 127 (2005) 16835.
- [8] A. Yella, H. W. Lee, H. N. Tsao, C. Yi, A.K. Chandiran, M.K. Nazeeruddin, E. W. G. Diau, C. Y. Yeh, S. M. Zakeeruddin, M. Grätzel. *Science* 334 (2011) 629.
- [9] J. Xia, S. Yanagida. *Solar Energy* 85 (2011) 3143.
- [10] D. R. Baker, P. V. Kamat. *Adv. Funct. Mater.* 19 (2009) 805.

- [11] Z. R. Dai, Z. W. Pan, Z. L. Wang. *Adv. Funct. Mater.* 13 (2003) 9.
- [12] X. Wang, H. Li, Y. Liu, W. Zhao, C. Liang, H. Huang, D. Moa, Z. Liu, X. Yu, Y. Deng, H. Shen. *Appl. Energ.* (2012) DOI 10.1016/j.apenergy.2012.05.014
- [13] M. Law, L. E. Greene, J. C. Johnson, R. Saykally, P. Yang. *Nat. Mater.* 4 (2005) 455
- [14] T. Zhang, W. Dong, M. Keeter-Brewer, S. Konar, R. N. Njabon, Z. R. Tian. *J. Am. Chem. Soc.* 128 (2006) 10960.
- [15] J. B. Baxter, E. S. Aydil. *Sol. Energ. Mat. Sol. C.* 90 (2006) 607.
- [16] N. Memarian, I. Concina, A. Braga, S. M. Rozati, A. Vomiero, G. Sberveglieri. *Angew. Chem.-Int. Edit.* 50 (2011) 1.
- [17] I. Buchmann. (2001) *Cadex Electronics Inc.* Richmond, BC, Canada.
- [18] B. Scrosati, J. Garche. *Journal of Power Sources* 195 (2010) 2419.
- [19] C. K. Chan, H. Peng, G. Liu, K. McIlwrath, X. F. Zhang, R. A. Huggins, Y. Cui. *Nat. Nanotechnol.* 3 (2008) 31.
- [20] T. Zhai, X. Fang, M. Liao. *Sensors* 9 (2009) 6504.
- [21] P. Poizot, S. Laruelle, S. Grugeon, L. Dupont, J. M. Tarascon. *Nature* 407 (2000) 496.
- [22] H. Huang, E. M. Kelder, J. Schoonman. *J. Power Sources* 97-98 (2001) 114.
- [23] M. Asamoto, S. Miyake, K. Sugihara, H. Yahiro. *Electrochem. Comm.* 11 (2009) 1508.
- [24] M. Mamak, N. Coombs, G. Ozin. *J. Am. Chem. Soc.* 122 (2000) 8932.
- [25] H. J. Snaith, L. S. Mende. *Adv. Mater.* 19 (2007) 3187.
- [26] M. Gratzel. *Nature*, 414 (2001) 338.
- [27] B. Sun, H. Sirringhaus. *Nanolett.* 5 (2005) 2408.
- [28] B. J. Norris, J. Anderson, J. F. Wager, D. A. Keszler. *J. Phys. D: Appl. Phys.* 36 (2003) L105
- [29] B. J. Kim, Y. R. Ryu, T. S. Lee, H. W. White. *Appl. Phys. Lett.* 94 (2009) 103506
- [30] I.P. Won, G.C. Yi. *Adv. Mater.* 1 (2004) 687.
- [31] J.S. Im, S-J Park, T. Kim, Y-S Lee, *Int. J. Hydrogen Energy*, 34, 3382 (2009)
- [32] Q. Wan, C. L. Lin, X. B. Yu, T. H. Wang. *Appl. Phys. Lett.* 84 (2004) 124.
- [33] M. Hepel, S. Hazelton. *Electrochim. Acta*, 50 (2005) 5278.
- [34] M. Quintana, E. Ricra, J. Rodriguez, W. Estrada. *Catalysis Today* 76 (2002) 141.
- [35] C. S. Rout, M. Hegde, A. Govindaraj, C. N. R. Rao. *Nanotech.* 18 (2007) 205504.
- [36] S. Zhao, P. Wei, S. Chen. *Sensor Actu. B* 62 (2000) 117.
- [37] Y. Li, F. D. Valle, M. Simonnet, I. Yamada J. J. Delaunay. *Nanotech.* 20 (2009) 045501
- [38] S. Bae, S. W. Lee, Y. Takemura. *Appl. Phys. Lett.* 89 (2006) 252503.
- [39] S.I. Stoeva, J.S. Lee, J.E. Smith, C.A. Mirkin. *J. Am. Chem. Soc.* 128 (2006) 8378.
- [40] Z. Yang, Z. H. Lin, C. Y. Tang, H. T. Chang. *Nanotech.* 18 (2007) 155606.
- [41] K. C. Barick, M. Aslam, V. P. Dravid, D. Bahadur. *J. Phys. Chem. C* 112 (2008) 15163
- [42] H. R. Fallah, M. Ghasemi, A. Hassanzadeh, H. Steki. *Phys. B* 373 (2006) 274.
- [43] H. Y. Kim, J. H. Kim, M. O. Park, S. Im. *Thin Solid Films* 93 (2001) 398.
- [44] Q. Yang, X. Jiang, X. Guo, Y. Chen, L. Tong. *Appl. Phys. Lett.* 94 (2009) 101108.
- [45] L. Schmidt-Mende, J. L. MacManus-Driscoll. *Materials Today* 10 (2007) 40.
- [46] J. R. Arthur. *Surface Science* 500 (2002) 189.

- [47] K. Wasa, S. Hayakawa. *Handbook of Sputter Deposition Technology* (1992) Noyes, Park Ridge.
- [48] D. B. Chrisey, G. K. Hubler. *Pulsed Laser Deposition of Thin Film* (1994) Wiley, New York.
- [49] J. H. Park, T. S. Sudarshan. *Chemical vapor deposition* (1st ed. 2001) ASM International, Scarborough
- [50] R. L. Adams. Metal Organic Chemical Vapor Deposition, in *Inorganic Reactions and Methods: For Formation of Bonds* (2007) to N, P, As, Sb, Bi (Part 2), Volume 8 (eds J. J. Zuckerman and A. D. Norman), John Wiley & Sons, Inc., Hoboken, NJ.
- [51] M. Leskel, M. Ritala. *Angew. Chem. Int. Ed.* 42 (2003) 5548.
- [52] P. S. Patil. *Materials Chemistry and Physics* 59 (1999) 185.
- [53] L. L. Hench, J. K. West. *Chem. Rev.* 90 (1990) 33.
- [54] G. P. Fotou, Y. S. Lin, S. E. Pratsinis. *Journal of Materials Science* 30 (1995) 2803.
- [55] M. Paunovic, M. Schlesinger. *Fundamentals of Electrochemical Deposition* (1998) Wiley, New York.
- [56] G. E. Thompson, Y. Xu, P. Skeldon, K. Shimizu, S. H. Han, G. C. Wood. *Phil. Mag. B* 55 (1987) 651

## Chapter 2

### Electrochemical devices for energy conversion and storage

In this chapter a detailed description of the two devices investigated in this work, i.e. DSCs and LiBs, is provided, focusing the attention on the different components and the working principles.

#### 2.1 Dye sensitized solar cells

Dye-sensitized Solar Cells have received considerable attention since the original work of O'Regan and Grätzel in 1991 [1], following the extensive research in semiconductor photo-electrochemistry started in the 1970s.

The major benefits lie in the materials and technologies needed for DSCs production. In fact, these kinds of solar harvesters can be produced with abundantly available organic materials and widely diffused inexpensive semiconductors, using simple and scalable technologies and avoiding high temperature and high-vacuum treatments, making them compatible with roll-to-roll mass production [2]. Moreover DSCs work effectively even in diffuse-light conditions being suitable for indoor application [3].

The working principle of the cell [4] is based on the presence of dye molecules, which are able to harvest photons from sunlight (mainly in the visible range) and convert them to electrons. The molecules of the sensitizer are excited from a lower to a higher energetic level, thus creating an electric potential that can be used to produce current. The light absorber is anchored as a monolayer on the surface of a nanocrystal-based film of a wide band gap semiconductor (usually  $\text{TiO}_2$  in the most common DSC architecture). The semiconductor works as electron collector, since the photogenerated charges are quickly injected in the conduction band of the nanostructured metal-oxide. A careful design of the molecular energy levels of the dye makes the charge transfer toward the oxide strongly favored from an energetic point of view, thus drastically reducing the electron hole recombination process. The dye is electrically regenerated by electrons donation from an electrolyte (usually a solvent-based liquid in which redox shuttles are dissolved), which penetrates the pores of the nanostructures to have a close proximity with the molecules of the sensitizer, creating 3D interpenetrating junctions. The electrolyte is an ionic conductor able to accept hole from (or donate electrons to) the oxidized dye. The most diffused redox couple is the  $\text{I}^-/\text{I}_3^-$ , which is able to guarantee excellent efficiency (around 11 %) [5], while the record performances (12

%) have recently been obtained with liquid electrolytes containing Co-based redox shuttles [6]. The electrons percolate through the nanoparticles, which are interconnected thanks to a sintering process, and are collected by an external circuit. Electric power is generated without causing any permanent chemical transformation inside the cell.

The role of the nanostructures in obtaining highly performing photoanodes is crucial. In fact, as reported by Graetzel during its experiments, it emerges that it is possible to move from a sunlight-to-current conversion efficiency of 1.2% using a polycrystalline anatase film [7] to 7.9% using a nanostructured mesoporous  $\text{TiO}_2$  layer [8], just varying the active exposed surface area of the electrode. The monolayer of dye anchored on a flat surface is able to absorb only a little percentage of the impinging photons, since its optical cross-section is smaller with respect to the occupied area. By using nanostructured semiconductive materials, it is possible to enhance the charge transport properties and to enlarge the surface area available for dye anchoring, thus increasing the energy harvesting efficiency of the DSC.

### 2.1.1 Structure and materials

The standard DSC structure is depicted in Figure 2.1: it mainly consists of a wide band gap nanocrystalline semiconductor deposited onto a glass covered by a transparent conducting oxide (TCO), a ruthenium-complex dye, an electrolytic solution containing an iodide/tri-iodide ( $\text{I}/\text{I}_3$ ) redox couple and a Pt-covered counter electrode.

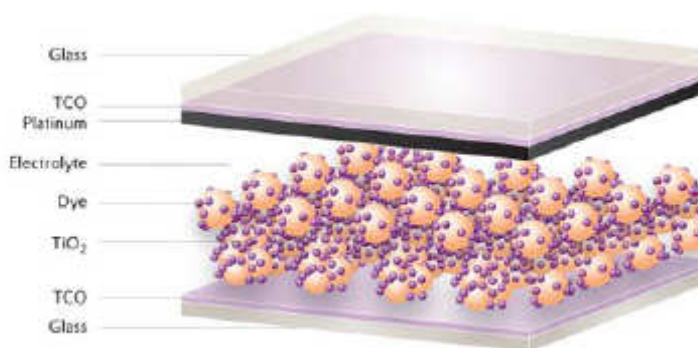


**Figure 2.1** Typical Dye-sensitized solar cell structure [9]

#### 2.1.1.1 Transparent conductive substrate

TCO-coated glasses are the standard substrates to fabricate DSC electrodes. The reason lies in their high transparency in the visible range and low sheet resistance, which are fundamental properties in this kind of photo-electrochemical devices. This class of materials belongs to n-type semiconductors, with a large band gap (around 4 eV), in which conduction is guaranteed by three fundamental sources: interstitial metal ion impurities, oxygen vacancies, and doping ions. Moreover, they show high thermal and chemical stability, other two important features since during photoanode fabrication relatively high temperature treatments (around 450 °C) are needed and the cell environment is quite aggressive (since electrochemical reactions occur). A lot of TCOs were developed and studied in the last thirty years and, among them, Fluorine-doped Tin Oxide (FTO) and Indium Tin Oxide (ITO) are mostly used because they are considered the best compromise in terms of fabrication process, optical and electrical properties.

### 2.1.1.2 Photoanode

The wide band gap semiconductor deposited onto TCO is usually called photoanode, being the support material on which the dye-molecules (i.e., those absorbing the light photo-generating electrons) are anchored. The semiconductor mainly receives photo-generated carriers from the dye and, thanks to suitable diffusion properties, collects them at the TCO layer.

Plenty of materials can be considered good candidates to do that job. Historically, the first proposed material was titanium dioxide ( $\text{TiO}_2$ ) in the form of nanocrystals.  $\text{TiO}_2$  has some unique properties that make it the semiconductor of choice for DSSC application. Its conduction band edge lies slightly below the excited state energy level of many dyes, which is a crucial condition for an efficient electron injection. Another positive aspect is the high dielectric constant of  $\text{TiO}_2$  ( $\epsilon = 80$  for anatase phase) that provides good electrostatic shielding of the injected electrons from the oxidized dye molecules, thus preventing their recombination before dye reduction. Moreover, its refractive index has a suitable value ( $n = 2.5$  for anatase) resulting in an efficient diffused scattering of the impinging light enhancing the light absorption. Most important in view of its practical application,  $\text{TiO}_2$  is a low cost, easily available, non-toxic material.

Zinc oxide ( $\text{ZnO}$ ) is well known as a promising alternative to titanium dioxide for the fabrication of Dye-sensitized Solar Cells photoanodes [10].  $\text{ZnO}$  is a wide band gap semiconductor (energy gap 3.37 eV), with a conduction band edge positioned approximately at the same level as for  $\text{TiO}_2$ . This means that ruthenium-based dyes developed for  $\text{TiO}_2$  can efficiently work also when anchored to  $\text{ZnO}$ . With respect to titanium dioxide,  $\text{ZnO}$  presents higher electron mobility and carrier lifetime, these parameters being very important to improve the performances of DSCs. Moreover, zinc oxide is well known for its ability to easily grow in a wide variety of nanostructures, like for instance nanoparticles[11], nanowires or nanorods[12], nanotubes[13], nanosheets[14], nanoplates[15] and nanotetrapods[16].

The ability to tune the morphology at the nanoscale can open up wide opportunities in the control of charge transfer dynamics in the photoelectrode. In fact, by appropriately tuning the morphology, it is possible to combine the fast direct transport in 1D or quasi 1D nanostructures (like nanowires and nanorods) with the wide exposed area for dye sensitization typical of mesoporous layers. The 1-D structures are characterized by superior charge transport properties along the c-axis direction but suffer for the reduced value of surface area if compared to nanoparticles. In fact, the specific area is one of the most important features in DSC photoanode since it can affect the number of anchored dye molecules: the resulting photovoltaic performances of low-dimensional nanostructured  $\text{ZnO}$  electrodes are therefore rather poor [17]. On the other hand, 3D structures possess the same good transport properties, maintaining, at the same time, a discrete number of sites for the dye sensitization. The great issue is the higher degree of complexity, which limits the reproducibility of the fabrication and the scalability towards larger area devices[17]. At present, the photoconversion efficiencies of  $\text{ZnO}$ -based DSCs are below 8% [11, 17, 18], so the suggestion of new structures and/or architectures aimed at the improvement of the cell performances is an exciting challenge.

### 2.1.1.3 Dye

The sensitizer, i.e. the dye, constitutes the heart of the DSC: it uses sunlight to pump electrons from a lower towards a higher energy level and in this way it generates an electric potential difference, which can be exploited to produce electric work.

A lot of attention is dedicated to its synthesis in order to optimize the light absorption and the charge transfer dynamics. The most common sensitizers employed in DSCs are ruthenium (Ru) complexes, due to the easily tunable photo-electrochemical properties of these molecules and the favorable oxidation states of the metal. When a photon of proper wavelength is absorbed by the dye molecule, an electron is excited from its fundamental state, i.e. the highest occupied molecular orbital (HOMO), to the lowest unoccupied molecular orbital (LUMO).

An ideal sensitizer for highly efficient DSCs should satisfy some basic requirements [19]: it should contain an anchoring group that strongly bonds to the  $\text{TiO}_2$  surface, thus ensuring electron coupling with the substrate, and it should absorb the largest fraction of the visible and near-IR region. Moreover, the molecule should be engineered in such a way that a suitable match between its discrete energy levels and the electronic bands of the oxide would be realized (see Fig. 2.2a), with the formation of a staggered (or type II) heterojunction [20]. Here, the LUMO of the dye has to be sufficiently high for efficient electron injection into the  $\text{TiO}_2$  conduction band, while the HOMO has to be positioned inside the semiconductor forbidden band-gap to avoid direct recombination from the semiconductor valence band. Moreover, it has to be sufficiently low for efficient regeneration of the oxidized states by accepting electrons from the redox mediator. Finally, the synthetic pathway should be easy and economical, also in terms of sustainability and life-cycle assessment.

#### 2.1.1.4 Electrolyte

The electrolytic solution that fills a DSC must regenerate the dye molecules (oxidized after photo excited electron injection into the semiconductor) and transport holes at the counter electrode to close the circuit.

Electrolytes employed in DSSC can be classified as liquid, quasi-solid and solid, depending on their viscosity. Several aspects are essential for any electrolyte to be used in DSCs:

1. it must be chosen in a proper way in order to take into account the redox potential and recombination properties of the dye;
2. the electrolyte must allow fast diffusion of the charge carriers into the device and have intimate contact with the porous nanocrystalline oxide layer and the counter electrode.
3. it must have long-term stability, including chemical, thermal, optical and electrochemical properties, to prevent degradation of the dye from the oxide surface;
4. the electrolyte should not exhibit a significant absorption in the range of visible light.

Any type of liquid electrolyte is composed by two main components: organic solvent and redox couple. In order to reduce recombination losses in the electrolyte, some additives are added. The most popular one is 4-tert-butyl pyridine [21]. It is adsorbed onto the  $\text{TiO}_2$  surface acting as barrier to the recombination between injected electrons in the oxide and oxidized species of the redox couple. The most important component of the ionic liquid electrolyte is the redox couple: it has the charge transfer function in the device.

In cells based on the  $\text{I}^-/\text{I}_3^-$  redox couple, the transfer of electrons from the oxide material to the  $\text{I}_3^-$  ions is a two electron process governed by the chemical dissociation of the  $\text{I}_3^-$ . This step is very slow with respect to the one occurring at the counter electrode: the recombination of  $\text{I}_3^-$  into  $\text{I}^-$  [22]. The regeneration process is accelerated by the presence of the catalyst (generally Pt) on the electrode and the fast diffusion of  $\text{I}^-/\text{I}_3^-$  into the liquid media.

#### 2.1.1.5 Counter electrode

The counter electrode is fundamental to close the electrical circuit through the reduction of triiodide into iodide. This reaction needs to be catalyzed, thus a thin layer of platinum (Pt) is deposited onto the TCO/glass substrate. Pt is the most used material for this task since it guarantees a low charge transfer and shows a good chemical stability against the various kinds of electrolytes usually employed in DSCs.

### 2.1.2 Working principle

Figure 2.2a recalls the main structure of a DSC underlying the charge transfer mechanisms involved in photocurrent generation. Sunlight is harvested by the sensitizer that is attached to the surface of a large band gap semiconductor. Photo-excitation of the dye (1) results in the injection of electrons into the conduction band of the oxide (3). The dye is regenerated by electron donation from an electrolyte (8) that is infiltrated into the porous films. Reduction of  $S^{+}$  by iodide regenerates the original form of the dye while producing triiodide ions.

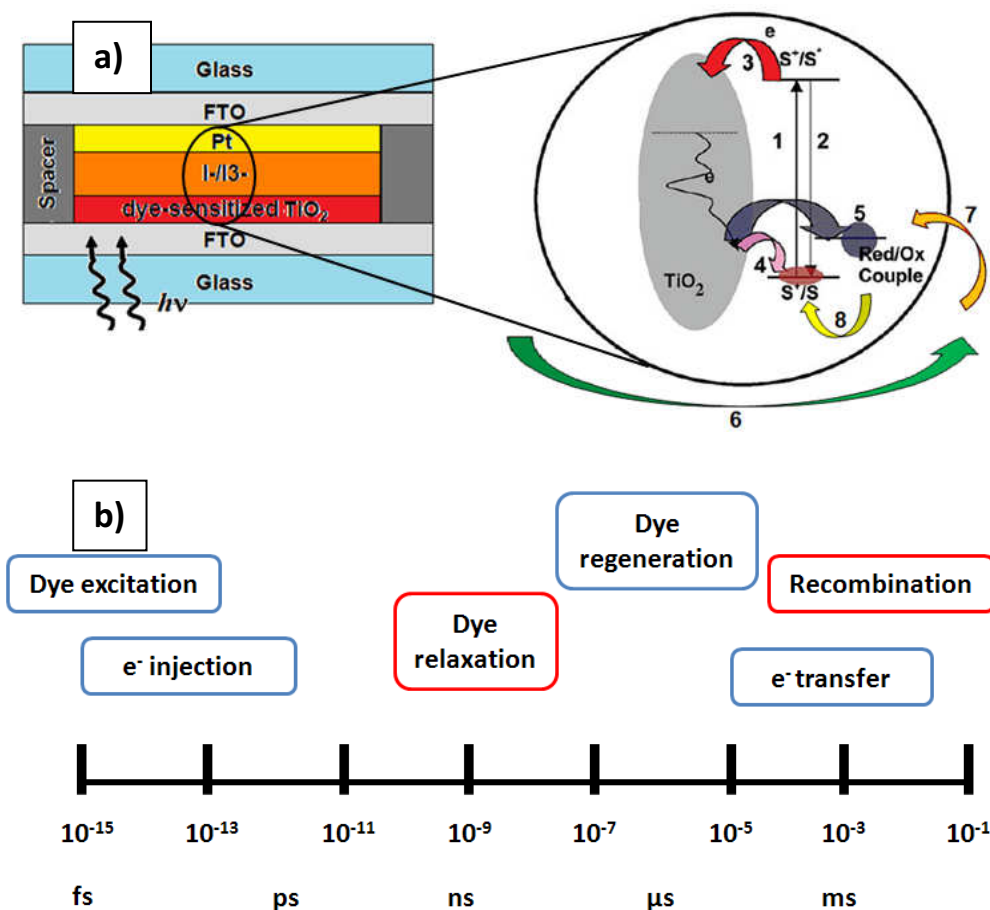


**Figure 2.2** schematic of DSC structure and corresponding charge transport mechanism (a); timescale of charge dynamics into a DSC (b); favorable processes in light blue and recombination in red.

This prevents any significant buildup of  $S^+$ , which could recapture the conduction band electron at the surface (4). The iodide is regenerated in turn by the reduction of the triiodide ions at the counter-electrode (7), where the electrons are supplied via migration through the external load completing the cycle (6). Thus, the device is generating electricity from light without any permanent chemical transformation.

The parallel electron transfer processes occur in competition with each other and having different characteristic times (see Fig. 2.2b). When illuminated, the dye molecule is excited in few femtoseconds [23] and the electron injection from LUMO to the photoanode conduction band is in the sub picosecond range [23]. The nanosecond-ranged relaxation of excited states is rather slow compared to that of injection, ensuring sufficient time for the favorable process to take place [24]. The ground state of the sensitizer is then reinstated by  $I^-$  in the microsecond domain. This time scale effectively reduces the chance of recombination of the injected electron to LUMO level, which usually takes few milliseconds [24]. This is followed by the two other important processes: electron percolation across the photoanode structure and collection of electrons by the oxidized  $I^-$  (which forms  $I_3^-$ ) within milliseconds.[25] The perfect matching of time constants of these processes is the key for achieving high conversion efficiencies in DSCs.[24]

### 2.1.3 Photovoltaic parameters and characterization techniques

#### 2.1.3.1 Current-Voltage measurements

A solar cell is a device able to contemporarily generates power and current on an external load upon illumination. In order to explain and completely understand a solar device, some important parameters must be introduced.

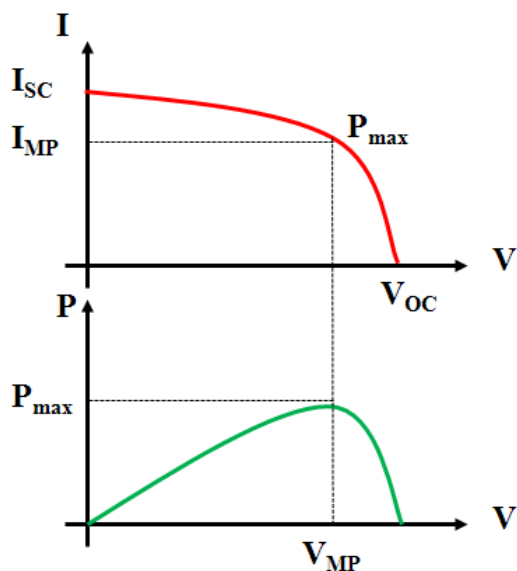


Figure 2.3 I-V characteristic of a solar cell.

When the cell is illuminated and its terminals are short-circuited, the maximum flowing current that can be measured is called short circuit current ( $I_{SC}$ ). Another measurable

parameter is the maximum voltage produced when the current flow is forbidden, called open circuit voltage ( $V_{OC}$ ). In the I-V characteristic (see the example reported in Fig. 3.2), the Maximum Power Point ( $P_{MAX}$ ) is the point of the curve in which the product between the current and the voltage is maximum. All these quantities are illustrated in Figure 2.3.

For any intermediate resistance value, the cell generates a potential between 0 and  $V_{OC}$ , and the corresponding current satisfying the relation  $V = R_L I$  (where  $R_L$  represent the external load). Generally, in order to have universally comparable quantities, instead of the current, the current density is preferable.

Having defined the Maximum Current Density ( $J_{MP}$ ) and the Maximum Voltage ( $V_{MP}$ ), another important parameter to analyze the performances of the cell is the Fill Factor (FF). It is defined as the ratio between the maximum power point and the product between the open circuit voltage and the short circuit density:

$$FF = \frac{V_{MP} J_{MP}}{V_{OC} J_{SC}} \quad (1)$$

In an ideal cell, the Fill Factor is equal to 1 and the cell has a I-V characteristic that is a perfectly rectangular. The power density generated by the cell, is defined as:

$$P_{MAX} = V_{OC} J_{SC} FF \quad (2)$$

Another important parameter is the overall photo conversion efficiency PCE (or  $\eta$ ), namely the ratio between the maximum power generated and the incident optical power  $P_{OPT}$ , i.e.:

$$\eta = PCE = \frac{P_{MAX}}{P_{OPT}} = \frac{V_{OC} J_{SC} FF}{P_{OPT}} \quad (3)$$

### 2.1.3.2 Incident photons to current conversion efficiency

The current density is related to the spectrum of the impinging light by the quantum efficiency  $QE(E)$ , defined as the probability that an absorbed photon with energy  $h\nu$  is able to produce the excitation of an electron. Using the quantum efficiency, it is possible to write an expression for the current density:

$$J_{SC} = q \int b_s(E) QE(E) dE \quad (4)$$

where  $b_s(E)$  is the flux density of incoming photons (i.e., the number of incident photons per time unit and with an energy between  $E$  and  $E + dE$ ) and  $q$  is the elementary charge.

In addition to  $\eta$ , the External Quantum efficiency (EQE, also known as Incident photons to current conversion efficiency or IPCE) can be defined

$$EQE = IPCE = \frac{\text{Number of charges collected by the solar cell}}{\text{Number of photons of a given energy shining on the solar cell from outside}} \quad (5)$$

An example of EQE curve recorded for a dye sensitized solar cell fabricated with Ru-complex dye is reported in figure 2.4.

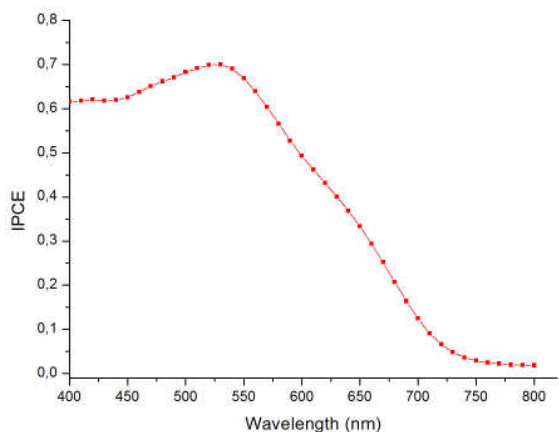


**Figure 2.4** Typical IPCE spectrum of a DSC fabricated with Ru-complex dye.

Considering the integral over all wavelengths of the spectrum:

$$J_{sc} / mAcm^{-2} = \int \frac{P_{in\lambda} \times \lambda}{1.99 \times 10^{-16}} \times \frac{IPCE_{\lambda}}{100} \times \frac{1}{6.24 \times 10^{18}} d\lambda \quad (6)$$

it is possible to obtain the  $J_{sc}$  value.

The measurement of the IPCE is very important in order to obtain information about the photoelectrical response of the DSC allowing the knowledge of the frequency range in which the dye molecules are able to absorb photons and efficiently convert them into electrons.

### 2.1.3.3 Open Circuit Voltage Decay

Open Circuit Voltage Decay (OCVD) is a well known technique used to study the recombination kinetics in DSCs [26]. The cells are kept under constant illumination at open circuit condition until they reach a steady voltage value. Then, the light is suddenly switched off and the photovoltage is measured as a function of time. Since under open circuit voltage condition all the photogenerated electrons cannot be collected by the electrode, they recombine with an approximately constant rate, thus reducing the photovoltage. Therefore, the decrease of  $V_{oc}$  depends only on charge recombination, and can be associated to the electron lifetime through the formula:

$$\tau = -\frac{k_B T}{q} \left( \frac{dV_{oc}}{dt} \right)^{-1} \quad (7)$$

where  $k_B T$  is the thermal energy.

### 2.1.3.4 Electrochemical Impedance Spectroscopy

In order to study the recombination and transport properties of DSCs, Electrochemical Impedance Spectroscopy (EIS) is one of the most widely used techniques, being at the same time a simple but powerful tool. A sinusoidal voltage of variable frequency is applied to the cell and the impedance is measured. In the typical Bode representation of phase impedance in DSCs, three main peaks can be observed (Fig. 2.5) [27]: the first one at high frequency (above 100 Hz) related to the charge transfer at the Pt/electrolyte interface, the second one at middle frequency (1-100 Hz) related to the recombination at the photoanode/electrolyte interface and to the charge transport into the semiconductor, and the third one at low frequency (below 1 Hz) related to the charge diffusion into the electrolyte.

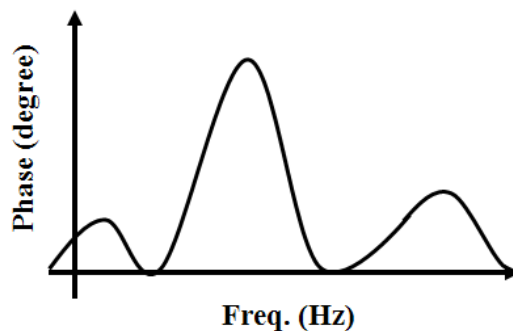


Figure 2.5 Typical Bode diagram of a DSC [28]

The experimental curves of EIS can be fitted using an equivalent circuit in order to obtain information about transport and recombination of charges. The modelling circuit is depicted in Figure 2.6: the resistance  $R_s$  represents the TCO series resistance, the parallel  $C_{CE}/R_{CE}$  takes into account the counter electrode/electrolyte interface and the impedance  $Z_{ph}$  models the photoanode behaviour. The charge diffusion into the electrolyte solution was not considered in the fitting circuit because no contribution aroused in the measured spectra at low frequencies. The photoanode impedance  $Z_{ph}$  (reported in Figure 1) was modelled though a transmission line, according to what proposed by [28]:  $R_T$  stands for the transport resistance,  $R_{CT}$  models the charge transfer resistance related to charge recombination, and the constant phase element (CPE)  $Q_\mu$  represents the generalized form of the electrochemical capacitance (CPE was introduced instead of a common capacitance to better describe the porous interface). The corresponding electrochemical capacitance  $C_\mu$  is:

$$C_\mu = (Q_\mu)^{\frac{1}{\beta}} (R_{CT})^{\frac{1}{\beta}-1} \quad (8)$$

Starting from the fitting parameters, one can compute the effective electron lifetime  $\tau$ , the diffusion coefficient  $D$  and the diffusion length  $L$  using the following formulae

$$\tau = (R_{CT} Q_\mu)^{1/\beta} \quad (9)$$

$$D = \frac{d^2}{R_T C_\mu} \quad (10)$$

$$L = (D\tau)^{1/2} \quad (11)$$

where  $d$  is the oxide thickness.

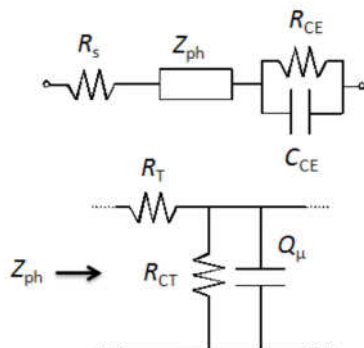


**Figure 2.6** Equivalent circuit used for the fitting of EIS data.  $Z_{ph}$  (reported below) is the transmission line model of the photoanode.

Typical DCS Nyquist plots present three arcs associated with the different cell components as depict in Figure 2.7. The first arc (above 1 kHz) is related to the interface between the electrolyte and the counter electrode, the second one (1-100 Hz) is associated to the interface between the electrolyte and the photoanode, and the third one (under 1 Hz) accounts for the charge diffusion into the electrolyte [19] [20].

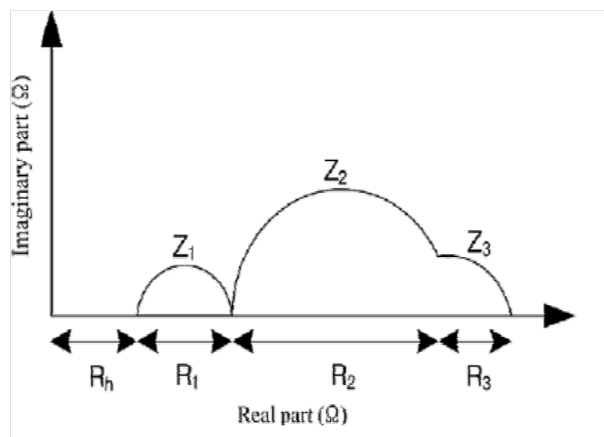


**Figure 2.7** Typical Nyquist plot of a DSC [28]

## 2.2 Li-ion microbatteries

Lithium-ion batteries (LIB) are one of the greatest successes of modern electrochemistry of materials. Their science and technology have been extensively reported in reviews [29] and dedicated books [30] to which the Reader is referred for more detailed discussion.

A commercial LIB does not contain lithium metal: it comprises a negative electrode (generally, graphitic carbon) and a positive electrode (generally, layered lithium metal oxides such as  $\text{LiCoO}_2$ ), both capable of reversibly intercalate  $\text{Li}^+$  ions, these being separated by a solvent based lithium-ion conducting electrolyte (generally, a separator diaphragm soaked in a mixed ethylene – diethyl carbonate solution of  $\text{LiPF}_6$ ).

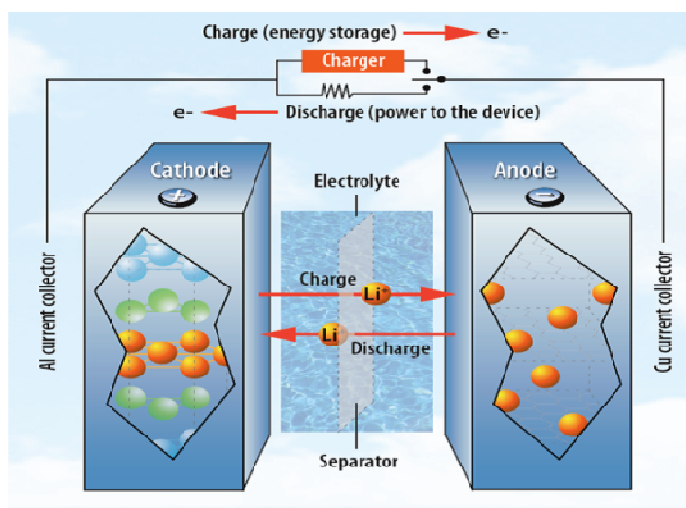


**Figure 2.8** Sketched picture of a LiB [31].

The active materials for Li-based batteries must be both electronic and ionic conductors in order to allow their correct operating, because low electronic conductivity or low mobility of  $\text{Li}^+$  would limit the current flow and, consequently, the power delivered by the device. Thus, it is important to fabricate nanostructured electrode materials that provide high surface area and short diffusion paths for ionic transport and electronic conduction. Moreover, nanoscale materials can better tolerate the typical volume changes and structural evolution upon Li ions insertion/deinsertion, which greatly affect the cycle/service life of LiBs.

Several advantages can be obtained by employing nanomaterials into LIBs:

- (a) the strain associated with lithium ions insertion/deinsertion is better accommodated (along with a wider solid-solution region), thus improving service life as shown in Figure 2.9;
- (b) new electrode reactions are enabled to occur that are not possible for materials composed of micrometer-sized particles;
- (c) a high surface area permits a more extensive electrode/ electrolyte contact area, leading to higher charge/discharge rates;
- (d) the reduced dimensions significantly reduce the path lengths for electronic and  $\text{Li}^+$  transport, thus permitting operation with low electronic conductivity and/or at higher power.

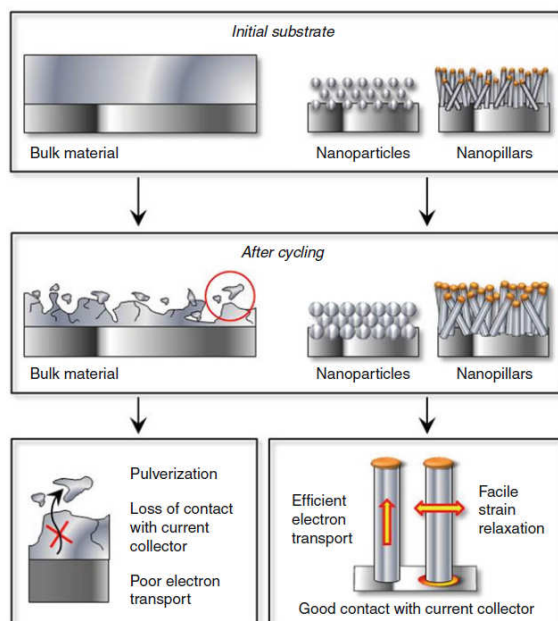


**Figure 2.9** Example of how nanostructuring can help in improving the performances of Li-ion battery electrodes by reducing the strain associated with lithium ions insertion/removal [32].

As for disadvantages, the following have been identified: (a) an increase in undesirable (side) reactions with the electrolyte due to the high electrode/electrolyte contact area, possibly leading to self-discharge, poor cycling and calendar life.

### 2.2.1 Structure and materials

Future advances in rechargeable Li-ion battery performance are strongly related to today's technologies, through a selective use of appropriate existing or new materials for the negative and positive electrodes. Actually, choosing the right materials is crucial for the battery's overall performance [33].

In order to be a successful electrode material, a compound should satisfy a number of criteria [34,35]:

- The intercalation/insertion compound should be able to accommodate a large number of lithium ions, in initially empty sites, to maximize the cell capacity. This depends on the number of available lithium sites in the host structure as well as the ability of the transition-metal to access multiple oxidation states.
- The  $\text{Li}^+$  insertion/de-insertion process has to be reversible and accompanied by no, or very small, changes in the host structure.
- It must be chemically and structurally stable over the whole voltage range, and insoluble in the electrolyte.
- It should be environmentally safe, easy to produce, with a low overall cost and high stability in air for easy handling.

It is also necessary to take into account other requirements to choose a good candidate as electrode material:

- Cathode materials should have a high potential versus  $\text{Li}^+/\text{Li}$ ; whereas anode materials should have a low potential versus  $\text{Li}^+/\text{Li}$ .
- Good performance in a wide temperature range.
- The intercalation/insertion reaction kinetics should be fast.

### 2.2.1.1 Anode

The most attractive material for use as an anode in rechargeable batteries would appear to be lithium metal because of its high potential and specific capacity. However, the poor rechargeability of the lithium anode prevents its practical use. This is due to the formation of Li dendrites after prolonged deposition/dissolution cycling, which brings about serious problems in terms of safety and cyclability [33]. The use of micro-porous separators can prevent the dendrite growth of lithium metal, but it increases the production costs of the system.

To overcome these problems, alloys of lithium with Al or Si have been considered; unfortunately, alloy electrodes survived only a limited number of cycles, owing to extreme changes in volume during operation. Besides intermetallic alloys, other systems have also been identified and intensively studied, like transition-metal oxides that can reversibly host  $\text{Li}^+$  ions and, more recently, intermetallic compounds having a strict structural relation to their lithiated products. Nowadays, the “standard” anode material for Li-ion batteries is carbon in its different layered structures. Carbon exhibits both electronic and ionic conductivity and can incorporate a large number of lithium ions. Due to their low cost, availability, low intercalation potential and good cycling properties carbonaceous materials have become, so far, the most attractive choice for anodes in practical Li-ion cells.

There are lots of modifications of carbon that can be used to produce anodes, e.g. natural and synthetic graphite, activated carbon, coke, carbon fibers, carbon nanotubes, etc.

Both the extent of lithium ions intercalation and the reversibility of the intercalation process strongly depend on the morphology and structure of the carbonaceous host material.

The electrolyte decomposition results in the formation of a surface protective film (solid electrolyte interface, SEI), consisting of a variety of solvent and salt reduction products, which allows the continuous operation of the carbonaceous anodes. SEI can be considered as a passivation layer for the carbon surface that prevents its further reaction with the electrolyte influencing the lifecycle and charge/discharge rate.

As outlined above, in the last years, various anode materials, alternative to carbonaceous compounds, have been investigated. In particular, much effort has been devoted to the use of transition-metal oxides, MO-type compounds (where  $\text{M} = \text{Co}, \text{Ni}, \text{Fe}, \text{Cu}$  or  $\text{Mn}$ ) having a rock-salt structure and containing metal elements that do not alloy with lithium [36]. The mechanism of lithium reactivity in such materials differs from the classical processes, and it is nested in the electrochemically driven, in situ formation of metal nanoparticles during the first discharge, which enables the formation and decomposition of  $\text{Li}_2\text{O}$  upon subsequent cycling. The reactions are highly reversible, providing large capacities (two to three times those of carbon) that can be maintained for hundreds of cycles.

### 2.2.1.2 Cathode

A typical cathode material for Li-ion batteries should have reasonably good electronic conductivity and provide a network of pathways for the lithium ions to diffuse in and out of the structure. The best host candidates have showed to be oxides [37,38], as they can support both high-valence-state cations, to obtain a high open circuit voltage, and good 3d-electron conductivity on a transition-metal cation array. Transition-metals are the elements that provide the redox activity to the material. Monovalent  $\text{Li}^+$  makes a primarily ionic bond with oxide ions, particularly where the oxide ions belong to polyanions, which allows rapid diffusion through a host with an interconnected interstitial free volume.

Many different crystallographic structures are presented by transition-metal oxides, but not all of them are suitable for the intercalation/insertion process. In fact, the ionic arrangement in the lattice must provide the two main requisites of intercalation compounds, namely ionic and electronic conductivity. The ionic conductivity must be guaranteed by the presence of mono-dimensional, bidimensional or tri-dimensional diffusion paths for the intercalating lithium ions (respectively defined as "tunnels" and "layers") formed by adjacent empty interstitial sites. The electronic conductivity is determined by the arrangement of the transition-metal cations in the lattice that must allow conductivity through 3d orbitals vicinity on adjacent cations.

### 2.2.1.3 Separator

The separator used in Li-ion batteries has two important functions [39]:

- avoiding the direct contact of the anode and cathode, while allowing the free mass transfer of the electrolyte;
- shutter action to stop the mass transfer in the case of accidental heat generation, which causes it to melt down, resulting in sealing the holes at the portion in question.

The material should be soft and flexible enough to be wounded by lying between both sheets of the electrodes. It should also be sufficiently stable for a long time while kept in contact with both the electrode materials and the electrolyte. Microporous polyethylene and polypropylene, are the most widely separators used.

### 2.2.1.4 Electrolyte

As previously outlined, the electrolyte, which commonly refers to a solution of salts and solvents, is the third key-component of a battery.

Under the ideal conditions, the selected electrolyte, in addition to provide a high ionic conductivity, should be able to induce the morphologically best protective film over the anode and to sustain the high operational potential of the cathode. It should also have low reactivity with the other components. Moreover, it should have a high thermal stability for Li-ion batteries to be used in devices working at relatively high temperatures.

A rechargeable Li-ion battery generally operates between  $-20$  and  $+60$  °C, thus solvents with low melting point, high boiling point and low vapor pressure are highly desirable [40].

Due to unavoidable electrolyte reduction at the anode, solvents that form a complete and stable SEI layer must be used. EC has an excellent SEI forming ability and it is frequently used to facilitate lithium-ion intercalation in graphite-based anodes. However, EC is solid at room temperature and, therefore, it must be dissolved in another solvent. A suitable choice is a solvent mixture such as EC/DEC, the same used to run the electrochemical tests shown in the experimental part of this thesis.

Soluble lithium salts are added to the solvents to act as charge carriers of the current passing in the cell during the electrochemical process. Good solubility and charge separation of anions and cations are necessary in order to obtain a high conductivity. Lithium hexafluorophosphate ( $\text{LiPF}_6$ ) is the most widely used salt in commercial Li-ion batteries. It has a high ionic conductivity in carbonate-based solutions, low toxicity and it shows excellent cycling properties at ambient temperature. However, it shows poor thermal stability [41], and it is highly moisture sensitive.

The most recent developments in the secondary Li-ion batteries technology are directed to the replacement of the liquid electrolyte with a polymer membrane capable of operating both as the separator and the electrolyte, in order to finally achieve the fabrication of batteries having a full-plastic structure [42]. This is an appealing concept since it provides the prospect of a favourable combination of high energy and long life, which are typical of the Li-ion process, with the reliability and easy processability, which are typical of the plastic configuration.

### 2.2.2 Working principle

The working principle of a secondary Li-ion battery is schematically explained in figure 2.10.

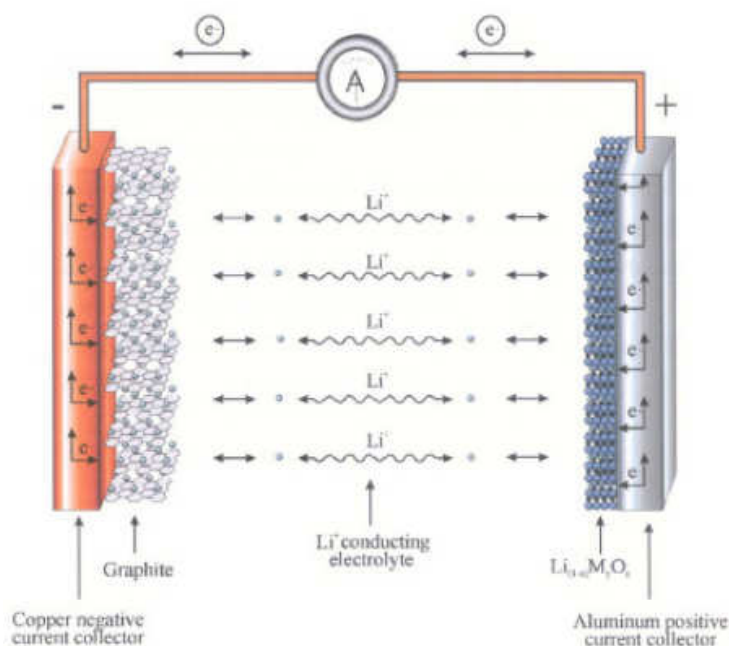
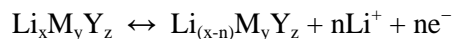


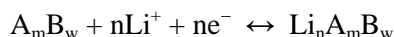
**Figure 2.10** Schematic of working principle of a LiB.

In general, both the electrodes of a lithium-ion battery have a structure capable of lithium storage. Rather than the traditional redox galvanic action, Li-ion secondary cell chemistry depends on an “intercalation/de-intercalation” mechanism.

During charge, the  $\text{Li}^+$  ions are de-inserted from the positive electrode, with relative oxidation of the active material  $\text{Li}_x\text{M}_y\text{Y}_z$ ,



they migrate across the electrolyte and are inserted into the crystal structure of the negative active material, which is reduced. At the same time, the compensating electrons travel in the external circuit and are accepted by the host to balance the reaction. The discharge process is just the opposite:



Accordingly, the overall reaction can be generalized as follows:



The process is completely reversible. Thus, the lithium ions pass back and forth between the electrodes during charging and discharging. This has given rise to the names “rocking chair”, “swing” or “shuttlecock” to describe the Li-ion cells [37].

### 2.2.3 Battery parameters

The performance of a battery is expressed by many quantities. The most important, in designing a battery, are capacity and energy density.

Capacity (Q) is defined as the total amount of electric charge supplied by the system or by the electrode materials and it is usually expressed in terms of Coulomb (C) or Ampere hour (Ah); 1 Ah = 3600 Coulombs. It can be calculated as the product of the current by the time: Specific capacity means the capacity per unit mass (Ah g<sup>-1</sup>) or per unit volume (Ah dm<sup>-3</sup>). The Theoretical capacity (Q<sub>t</sub>) is the maximum amount of charge that can be extracted from a battery with respect of the amount of active material.

The energy (E) of an electrochemical power source can supply is expressed in Joule (J) or more commonly in Watt hour (Wh). Specific energy (or usually energy density) is defined as the energy output from a battery per unit mass (Wh g<sup>-1</sup>) or per unit volume (Wh dm<sup>-3</sup>).

### 2.2.4 Characterization techniques

Galvanostatic cycling is an important method to evaluate the appropriateness of a compound to be used as electrode material. A direct and constant current (I) is here applied to the cell; simultaneously, the voltage is monitored as a function of time (t) in order to verify the potentials of the reduction/oxidation processes of the active material and the total amount of charge passed per unit mass of electrode material (i.e., the specific capacity C) during complete discharge (or charge). The potential is relative to the lithium metal used as anode. This technique gives information about, for instance, the reversibility of the electrochemical process during cycling, the long-term cycling behavior and the rate capability, measuring the amount of charge passed through the cell in the charge and discharge of each cycle. Also, the shape of the potential versus time curve can hold information on phase transitions. A gently sloping curve points to a solid solution of lithium in the host material, while discrete plateaus can identify the existence of stoichiometric phases.

Cyclic voltammetry (CV) is a potentio-dynamic technique in which a linear scan of the potential is imposed on the working electrode; then, the current flowing between the working electrode and the counter-electrode is recorded. It is important to monitor the reference electrode for the measurement of the potential from the counter-electrode through which the current passes with the aim of avoiding over-potential due to charge transfer and other

contributions of the resistance. The diagram of the current as a function of the applied potential so obtained shows the peaks corresponding to the electrochemical processes occurring in the potential range considered. The study of such diagrams allows one to obtain qualitative information about the potential at which the electrochemical processes occur (by the position of the peak) and the exchanged current during the process (by the area of the peak).

The resistance and electrochemical stability of both electrode materials and cells is generally tested by electrochemical impedance spectroscopy (EIS) analysis at ambient temperature (usually, in the frequency range from 100 mHz to 100 kHz, at open circuit potential), following the behavior of the test cell for several consecutive days and/or number of cycles.

## 2.3 References

- [1] B. O'Regan, M. Grätzel. *Nature* 353 (1991) 737.
- [2] G. Hashmi, K. Miettunen, T. Peltola, J. Halme, I. Asghar, K. Aitola, M. Toivola, P. Lund. *Renew. Sust. Energ. Rev.* 15 (2011) 3717.
- [3] A. Sacco, L. Rolle, L. Scaltrito, E. Tresso, C.F. Pirri. *Appl. Energ.* (2012) DOI 10.1016/j.apenergy.2012.07.001.
- [4] M. Grätzel. *Acc. Chem. Res.*, 42 (2009) 1788.
- [5] M. K. Nazeeruddin, F. De Angelis, S. Fantacci, A. Selloni, G. Viscardi, P. Liska, S. Ito, B. Takeru and M. Graetzel. *J. Am. Chem. Soc.* 127 (2005) 16835.
- [6] A. Yella, H. W. Lee, H. N. Tsao, C. Yi, A.K. Chandiran, M.K. Nazeeruddin, E. W. G. Diao, C. Y. Yeh, S. M. Zakeeruddin, M. Grätzel. *Science* 334 (2011) 629.
- [7] N. Vlachopoulos, P. Liska, J. Augustynski, M. Gratzel. *J. Am. Chem. Soc.* 110 (1988) 1216.
- [8] B. O'Regan, M. Grätzel, D. Fitzmaurice. *Chemical Physics Letters* (1991) 89.
- [9] <http://www.aerosil.com>
- [10] Q. Zhang, C. S. Dandeneau, X. Zhou, G. Cao. *Adv. Mater.* 21 (2009) 4087.
- [11] K. Keis, E. Magnusson, H. Lindstrom, S. E. Lindquist, A. Hagfeldt. *Sol. Energy Mater. Sol. Cells* 73 (2002) 51.
- [12] D. Calestani, M. Z. Zha, L. Zanotti, M. Villani, A. Zappettini. *Cryst. Eng. Comm.* 13 (2011) 1707.
- [13] Q. C. Li, V. Kumar, Y. Li, H. T. Zhang, T. J. Marks, R. P. H. Chang. *Chem. Mater.* 17 (2005) 1001.
- [14] J. H. Xiang, P. X. Zhu, Y. Masuda, M. Okuya, S. Kaneko, K. Koumoto. *J. Nanosci. Nanotechnol.* 6 (2006) 1797.
- [15] A. Tiwari, M. Snure. *J. Nanosci. Nanotechnol.* 8 (2008) 3981.
- [16] D. Calestani, M. Zha, R. Mosca, A. Zappettini, M. C. Carotta, V. Di Natale, L. Zanotti. *Sens. Actuat. B* 144 (2010) 472.
- [17] I. Gonzalez-Valls, M. Lira-Cantu. *Energ. Environ. Sci.* 2 (2009) 19.
- [18] N. Memarian, I. Concina, A. Braga, S. M. Rozati, A. Vomiero, G. Sberveglieri. *Angew. Chem.-Int. Edit.* 50 (2011) 1.
- [19] A. Mishra, M. K. R. Fischer, Peter Bauerle. *Angew. Chem. Int. Ed.* 48 (2009) 2474.
- [20] A. Calzolari, A. Ruini, A. Catellani. *J. Am. Chem. Soc.* 133 (2011) 5893.
- [21] A. Jena, S. P. Mohanty, P. Kumar, J. Naduvath, V. Gondane, P. Lekha, J. Das, H. K. Narula, S. Mallick, P. Bhargava. *Transactions of the Indian Ceramic Society*, 71 (2012) 116.
- [22] S. Hao, P. Li, J. Lin, M. Huang, L. Fang, J. Wu, Z. Lan, Y. Huang. *Pure Appl. Chem.* 80 (2008) 2241.

- [23] Y. Tachibana, J. E. Moser, M. Gratzel, D. R. Klug, J. R. Durrant. *J. Phys. Chem.* 100 (1996) 20056.
- [24] M. Gratzel. *Inorg. Chem.* 44 (2005) 6841.
- [25] N. J. Cherepy, G. P. Smestad, M. Gratzel, J. Z. Zhang. *J. Phys. Chem. B* 101 (1997) 9342.
- [26] A. Zaban, M. Greenshtein, J. Bisquert. *ChemPhysChem.* 4 (2003) 859.
- [27] A. Sacco, A. Lamberti, M. Quaglio, S. Bianco, E. Tresso, A.L. Alexe-Ionescu, C.F. Pirri. *Int. J. Photoenergy* 2012 (2012) 216780.
- [28] J. Bisquert, G. Garcia-Belmonte, F. Fabregat-Santiago, N. S. Ferriols, P. Bogdanoff, E. C. Pereira. *J. Phys. Chem. B* 104 (2000) 2287.
- [29] A.S. Arico, P. Bruce, B. Scrosati, J. M. Tarascon, W. van Schalkwijk. *Nat. Mater.* 4 (2005) 366.
- [30] W. van Schalkwijk, B. Scrosati (eds.): *Advances in Lithium-Ion Batteries*. Kluwer/Plenum, New York (2002)
- [31] <http://techportal.eere.energy.gov/image.xhtml?id=475&techID=600>
- [32] B. Bhushan (ed.), *Encyclopedia of Nanotechnology*, DOI 10.1007/978-90-481-9751-4
- [33] B. Scrosati, J. Garche. *Journal of Power Sources* 195 (2010) 2419.
- [34] M. M. Thackeray. *Prog. Solid. St. Chem.* 25 (1997) 1.
- [35] S. Nordlinder, Ph.D. Thesis “Nanotubes for Battery Applications”, Uppsala University, Sweden 2 (2005) 20.
- [36] P. Poizot, S. Laruelle, S. Grugeon, L. Dupont, J.-M. Tarascon. *Nature* 407 (2000) 496.
- [37] J. B. Goodenough. *Advances in Lithium Ion Batteries*, editors W.A. van Schalkwijk and B. Scrosati, Kluwer Academic/Plenum Publisher, New York 4 (2002) 135-154.
- [38] D. Guyomard in *Energy Storage Systems for Electronics*, editors T. Osaka and M. Datta, Gordon and Breach Science Publishers, Amsterdam 9 (2000) 253-350.
- [39] T. Takamura. *Solid State Ionics* 152-153 (2002) 19.
- [40] M. Wakihara. *Mat. Science and Engineer.* R 33 (2001) 109.
- [41] L. J. Krause, W. Lamanna, J. Summerfield, M. Engle, G. Korba, R. Loch. *J. Power Sources* 68 (1997) 320.
- [42] B. Scrosati. *Electrochim. Acta* 45 (2000) 2461.

## Chapter 3

### Metal-oxide nanostructures: growth and characterization

In this chapter the synthesis and material characterization of TiO<sub>2</sub> nanotube array obtained by anodic oxidation and ZnO sponge-like films by combined sputtering/thermal oxidation techniques are reported.

#### 3.1 Materials and characterizations

##### 3.1.1 TiO<sub>2</sub> nanotubes

A 250  $\mu\text{m}$  thick titanium foil (99.6 % purity, Goodfellow) and a Pt sheet (99.99 % purity, 250  $\mu\text{m}$  thick, Goodfellow) were employed as anode and cathode in a two-electrode configuration Teflon cell. The electrolytic solution was prepared adding 0.5 wt. % NH<sub>4</sub>F and 2.5 vol. % deionized water in ethylene glycol. Unless differently specified, all chemicals have been purchased from Sigma Aldrich.

##### 3.1.2 Sponge-like ZnO

Zinc films were deposited on silicon substrates and on glasses coated with fluorine-doped tin oxide (FTO, Solaronix) by the RF magnetron sputtering technique.

A zinc target, with a purity of 99.99% and a diameter of 101.6 mm (Goodfellow), was fixed on the cathode, placed at about 8 cm from the substrate holder. Argon (5.0 purity) was used as sputtering gas.

##### 3.1.3 Characterization techniques

The morphological characterizations of the TiO<sub>2</sub> NT arrays and ZnO nanostructures were performed by Field Emission Scanning Electron Microscopy (FESEM, ZEISS Supra 40 and ZEISS Auriga) equipped with an Energy Dispersive X-ray spectrometer (EDX, Oxford INCA Energy 450) for compositional analysis.

BET (Brunauer–Emmett–Teller) specific surface area was measured from N<sub>2</sub> sorption isotherms (Quantachrome Autosorb1) by multipoint method within the relative pressure range of 0.1–0.3 P/P<sub>0</sub>.

X-ray diffraction technique was used to determine the crystalline structure of the films (Panalytical PW1140–PW3020, Cu K $\alpha$  X-ray source). The scans were performed in a parallel beam geometry with a fixed angle of incidence  $\omega=1.5^\circ$ , in order to minimize the contribution of the substrate.

Contact angle measurements were performed using a OCA H200 Dataphysics equipment in ambient conditions. The sessile drop method was implemented employing distilled water droplets having a volume of 2.5  $\mu\text{L}$ .

Bright field and high resolution TEM analyses were performed with a FEI TECNAI ST 200kV S/TEM Transmission Electron Microscope (TEM) microscope equipped with Energy Dispersive X-ray spectrometer (EDX).

UV-visible spectroscopy measurements were carried out using a Varian Cary 5000 spectrophotometer equipped with an integrating sphere for diffuse and specular reflectance.

I-V electrical measurements were performed with a Keithley 2635A source measure unit both in dark and light conditions. In order to provide top contacts for electrical characterizations, circular metal electrodes (diameter of 2 mm and thickness of about 80 nm) of Gold were deposited on the sample surface by RF magnetron sputtering and patterned by means of a shadow mask.

## 3.2 TiO $_2$ Nanotubes

### 3.2.1 Growth mechanism

This paragraph presents information on perhaps the most impressive and unexpected 1D metal-oxide nanostructure: self-organized TiO $_2$  nanotube arrays. The synthesis is carried out by a simple, low-cost and straight-forward approach: conventional electrochemical anodization of a metallic titanium substrate under a specific set of “right” conditions. Currently, the publication rate on this topic shows an almost exponential trend, with more than 1000 papers being published over the last 3 years [1].

For Al and other so-called valve metals (Ti, Zr, Nb, W, Ta) it is known that it is possible to grow compact oxide layers of considerable thickness (some hundred of nm) by anodization in aqueous electrolytes [2].

The best investigated system, in which almost perfect self-organization of pores in oxide can be established, is the anodic grown porous aluminum oxide. Over 50 years ago,[3] it was realized that upon anodic treatment of aluminum in neutral and/or alkaline electrolytes, a flat, compact oxide would grow, but when acidic electrolytes are employed relatively regular porous oxide (some hundred of nanometers) structures could be grown.

In the last decade several models trying to provide a mechanistic explanation for the occurrence of hexagonal self-organization of porous alumina growth were developed attributing the cause to: 1) stress at the metal–oxide interface (volume expansion/electrostriction) [4], 2) repulsion of electric fields [5] or 3) establishing maximum current-flow conditions [6].

Particularly the case of anodization of Titanium stimulated significant research activity since TiO $_2$  is a material with a number of almost unique properties used for many years in various functional applications.

In general, the morphology and the structure of porous layers are strongly affected by the electrochemical conditions (particularly the anodization voltage) and the solution parameters (in particular the HF concentration and the water content in the electrolyte).

It is possible to distinguish three “generations” of TiO $_2$  nanotubes [7]. The first one is obtained by growing the TiO $_2$  nanotube arrays in HF electrolytes or acidic HF mixtures

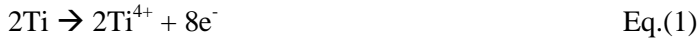
[8]. These tubes showed very rough walls and a limited thickness that would not exceed 600 nm.

By using buffered neutral electrolytes (second generation) containing NaF or NH<sub>4</sub>F instead of HF it was shown that self-organized nanotube TiO<sub>2</sub> layers with thicknesses higher than 2 µm could be grown [9].

The third generation nanotubes were grown in organic electrolytes with a very small content of water. Earlier work carried out in glycerol electrolytes showed tubes with extremely smooth walls and a tube length exceeding 7 µm [10], while using ethylene glycol electrolytes and by a further optimization of parameters, the nanotube length has reached 1mm [11] and perfectly smooth walls. Water content in the electrolyte affects the growth rate and the etching speed (chemical dissolution rate) of the nanotubes. In other words, the effect of water content is two-fold: it is required for oxide formation (tube bottom), but it also accelerates the dissolution of the nanotube layer (if the formed metal fluorides are water-soluble).

In the anodic oxidation of titanium performed in this work a potential is applied between an anode (usually a Ti foil of thin film) and a cathode (usually a Pt foil) immersed into a fluorine based electrolytic solution, in organic solvent with a little content of water.

The formation of TiO<sub>2</sub> nanotube membranes in fluorine-based electrolyte starts with the oxidation of the metallic surface which releases Ti<sup>4+</sup> ions and electrons (Eq.(1)).



An oxide layer is deposited on the metal surface from interaction of Ti<sup>4+</sup> ions and O<sub>2</sub> or OH<sup>-</sup> ions of water. Eqs.(2) and (3) describe the formation of hydrated anodic and oxide layer.



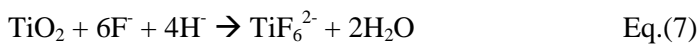
The Titanium Dioxide is produced from the hydrated anodic layer by a condensation reaction (Eq.(4)).



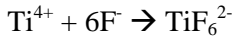
At the cathode (Eq.(5)), hydrogen evolution occurs and the entire process of oxide formation is expressed in Eq.(6).



The fluorine ions in the electrolyte attack the hydrated and oxide layer, where the F ions are mobile in the anodic layer and react with Ti<sup>4+</sup> under the applied electric field. Field-assisted dissolution of the oxide occurs therefore at the interface between oxide and electrolyte. Localized dissolution of the oxide creates small pits (Eqs.(7) and(8)).



These locally etched pits act as pore forming centers, which convert into pores uniformly distributed over the whole surface. The pores start to grow at the pore bottom with inward movement of the oxide layer, as depicted in figure 3.1. Ionic species ( $F^-$ ,  $O_2$ ,  $OH^-$ ) migrate from the electrolyte toward the metal/oxide interface. The  $TiO$  bond undergoes polarization and is weakened to assist dissolution of the metal cations. Ions  $Ti^{4+}$  migrating from the metal to the oxide/electrolyte interface dissolve in the HF electrolyte (Eq.(9)). The free  $O_2$  anions migrate toward the metal/oxide interface and further interact with the metal.



Eq.(9)

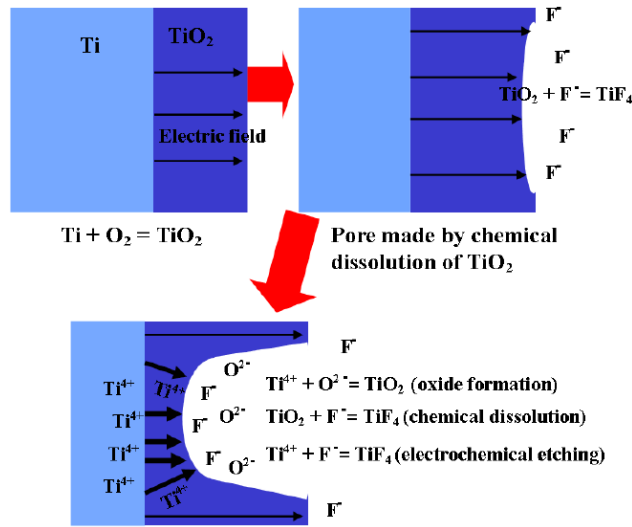


**Figure 3.1** Schematic representation of anodic oxidation process of Ti into fluorine-based electrolyte [12]

The growth of the oxide can then be monitored by recording the current–time characteristics. In Figure 3.2 a typical  $I-t$  curve for conditions that lead to nanotube formation is shown. The curve shows three stages: I) In the initial stage of anodization the curve essentially follows the fluoride-free case, and if samples are removed from the electrolyte, a compact oxide layer is present. In stage II, a current increase occurs, and irregular nanoscale pores are initially formed that penetrate the initial compact oxide (the current increases as the reactive area increases). In step III, the current drops again as a regular nanopore or nanotube layer forms.

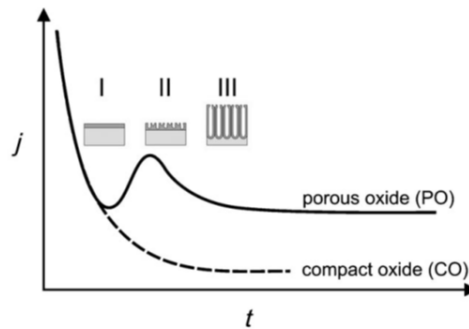


**Figure 3.2** Current density–time characteristics recorded during anodic oxidation of Ti substrate [12]

An interesting aspect of Ti anodization concerns the length of the tubes. The expected expansion factor when metal is converted into oxide is given by the ratio of the volume of the oxide to the volume of the consumed metal and is frequently called the Pilling–Bedworth ratio (PBR) [13]. This ratio for  $\text{TiO}_2$  obtained by anodic oxidation was calculated to be 2.43 [14]. However, the tubes grew much larger than expected, and an expansion factor of about 3 can be observed [12]. This unexpectedly high volume expansion is ascribed to an additional lengthening of the tubes by plastic flow. The “flow concept” was originally employed to explain the growth of anodized  $\text{Al}_2\text{O}_3$  [15]. For  $\text{Al}_2\text{O}_3$ , oxide flow is assumed to originate from the plasticity of the barrier layer generated by the substantial ionic movement in the high electric field together with the compressive stresses induced by the volume expansion and the electrostrictive forces generated during growth. The result is a force that pushes viscous oxide up the pore walls and thus extends the tube lengths. Overall, the increased volume expansion factors observed during the growth of  $\text{TiO}_2$  nanotubes suggest a similar mechanism for the growth of  $\text{TiO}_2$  nanotubes. During the growth of the oxide (and supported by plastic flow), an accumulation of fluorides takes place at cell boundaries. These regions are sensitized, as the fluoride-rich layer is prone to chemical dissolution: selective chemical dissolution (in aqueous electrolyte) of the fluoride rich layer etches out the cell boundaries and thus leads to individual tube shapes.

### 3.2.2 Synthesis procedure

A titanium foil was manually cut into 3×2 cm pieces, cleaned by ultra-sonication in acetone and rinsed in isopropyl alcohol. The  $\text{TiO}_2$  NT carpet was grown by anodic oxidation inside a Teflon electrochemical cell reported in figure 3.3.

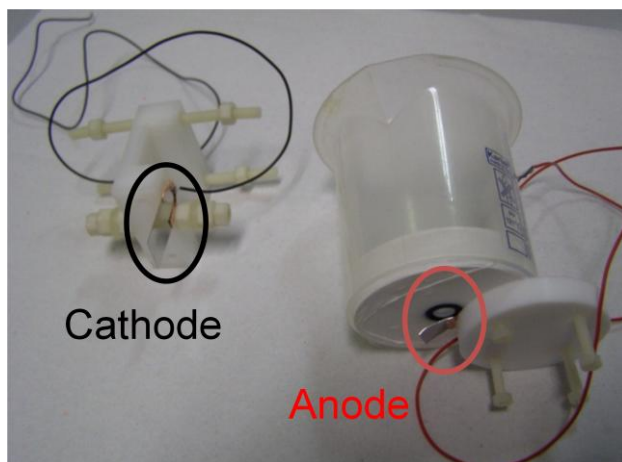


**Figure 3.3** Photograph of the Teflon O-ring electrochemical cell employed during the anodic oxidation of Ti foil.

The electrolytic solution was prepared adding 0.5 wt. %  $\text{NH}_4\text{F}$  and 2.5 vol. % deionized water in ethylene glycol and the electrochemical reaction was performed at a constant voltage of 60 V. After the anodic oxidation, the Ti foil covered with NTs was repeatedly rinsed in distilled water to remove the electrolyte residual from the tubes surface. The samples were then rapidly annealed at 450 °C for 1 hour to obtain the crystallisation of the material in the anatase phase.

### 3.2.3 Results & Discussion

#### 3.2.3.1 Field Emission Scanning Electron Microscopy

In figure 3.4, the FESEM characterization of the vertically aligned  $\text{TiO}_2$  NT arrays obtained at the end of anodic oxidation process, are reported. In Figures 3.4c-d, the top and bottom views of the NT carpet, where is clearly visible the hexagonally-packed assembly of the anodized titanium oxide, is reported. The average external diameter of the tubes can be estimated to be around 130 nm.

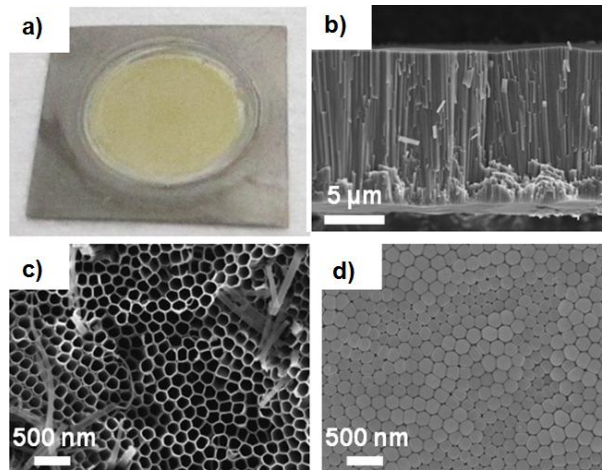


**Figure 3.4.** Photograph of as anodized Ti foil (a) FESEM micrographs showing the cross-section of  $\text{TiO}_2$  nts array (b) and the top (c) and bottom (d) views of  $\text{TiO}_2$  nts.

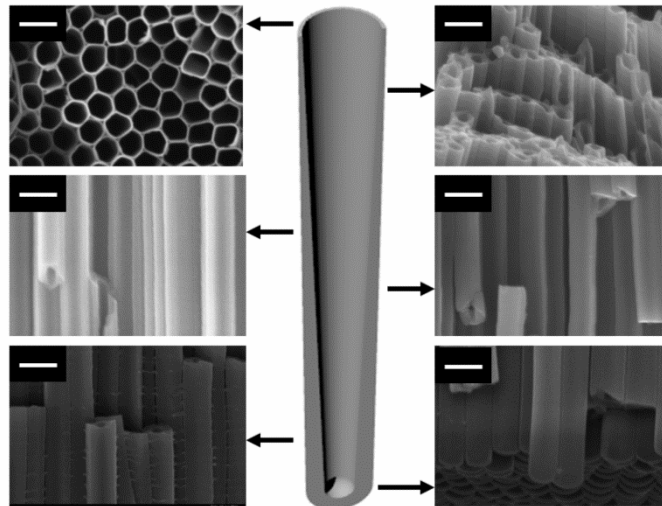


**Figure 3.5.** 3D image of  $\text{TiO}_2$  nanotube shape supported by FESEM micrographs showing cross sectional view in different section of the tubes array (scale bars are 200 nm in all the pictures).

Although the outer diameter doesn't change along the total length of the tube, the inner one decreases from  $\sim 100$  nm (top) down to  $\sim 30$  nm (bottom). Figure 3.5 clearly outlines this scenario with a 3D drawing of the  $\text{TiO}_2$  nanotube shape, supported by FESEM

micrographs showing cross sectional views at different heights (one about each 10  $\mu\text{m}$ ) of the NT membrane.

The dependence of  $\text{TiO}_2$  NT array length on the anodization time was also investigated in the range of 1 - 4 hours. The results obtained with the FESEM characterization are reported in the graph in Figure 3.6: the growth rate is linear with time and membranes up to 57  $\mu\text{m}$  thick were obtained for 4 hours of anodic oxidation. Although the linear trend is well known [16], the growth rate curves reported in the literature with the same conditions correspond to lower values of NT length [17].

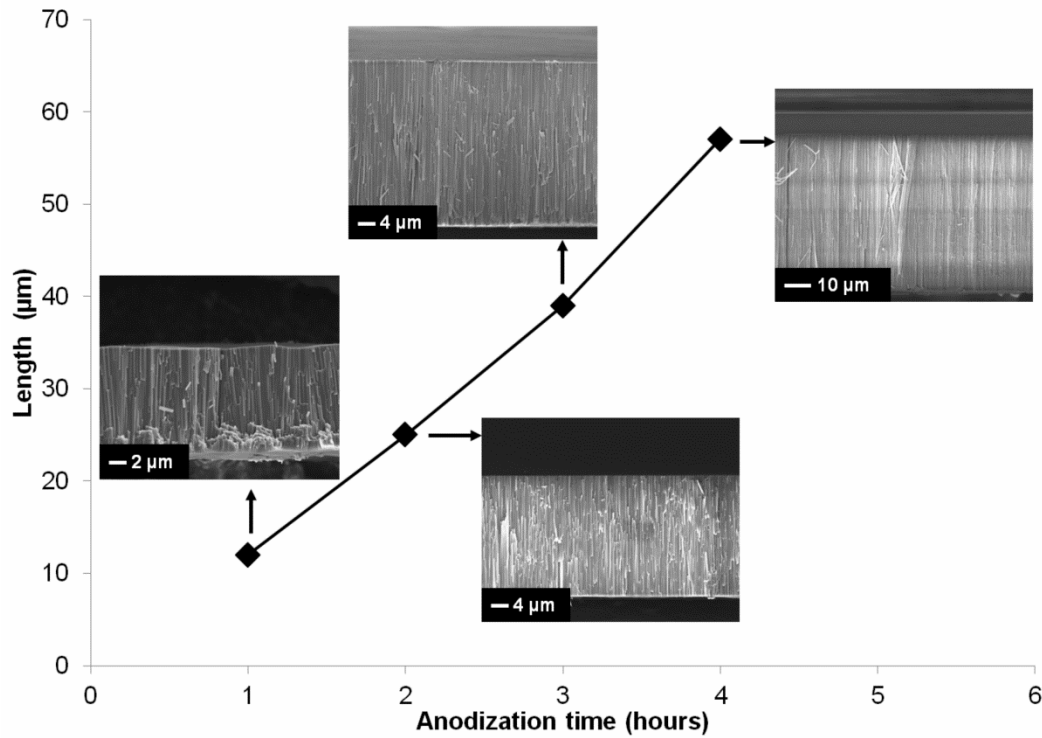


**Figure 3.6.** Dependence of  $\text{TiO}_2$  NT array length on the anodization time.

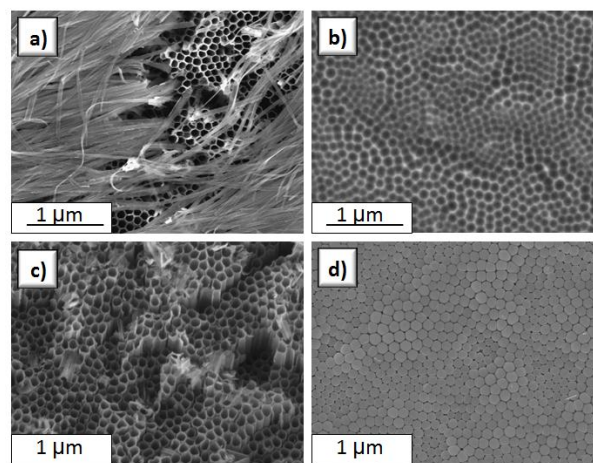


**Figure 3.7** FESEM micrographs showing the surface of the  $\text{TiO}_2$  Nts array after the first step of anodic oxidation (a) and the Ti surface after the growth and removal of the sacrificial NT layer (b); the top (c) and the bottom (d) of the  $\text{TiO}_2$  NT array grown after the second anodization.

A one-step anodic oxidation process can lead to the synthesis of disordered  $\text{TiO}_2$  nanowires (NWs) on the top of the  $\text{TiO}_2$  nanotubes (see Fig. 3.7a). The formation of NWs is due to the chemical dissolution of the tube top by means of the fluoride species. This phenomenon is detrimental for NT based electrode for electrochemical device, since NWs can hamper the infiltration of solutions (dye molecules, electrolyte, etc). In order to achieve a debris-free and well ordered array of NTs with open top surfaces and fast growth rate some expedients have to be implemented. Non-aqueous organic electrolytes are considered to be the key to successfully achieve ultra-fast growth rate at high anodization potential [11]. In addition, the morphology of the Ti foil plays a crucial role; in fact, the optimal surface should be preferably textured rather than perfectly planar and smooth. The surface morphology is crucial particularly at the beginning of the electrochemical process, thus a pre-anodization could be beneficial leading to the formation of a sacrificial  $\text{TiO}_2$  NTs layer (usually covered by thin or thick NWs layer). After removal of the preformed sacrificial layer, the resulting Ti surface is fully covered by holes previously occupied by the bottom side of the NTs. As a consequence, the electrochemical growth of the final NT array is faster and a more ordered distribution can be obtained [18] due to the presence of a preformed pathway. FESEM micrographs reported Fig. 3.7b show the surface of the Ti foil after the growth and removal of the sacrificial NT layer. The hollow-textured Ti surface was then again anodized, thus obtaining the well-ordered NT array illustrated in Fig. 3.7c (top view) and 3.7d (bottom view).

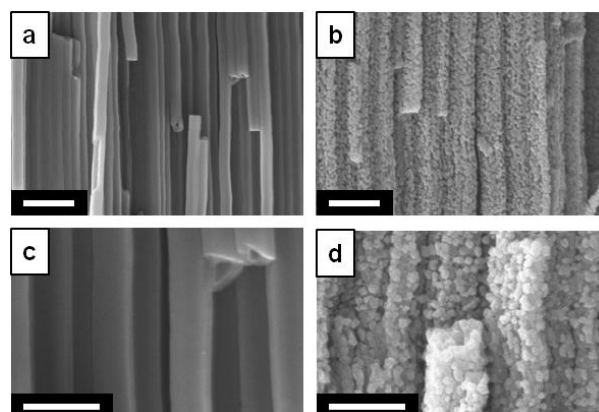


**Figure 3.8** FESEM micrographs acquired at different magnification showing the cross view of NT membrane before (a,c) and after (b, d) thermal treatment. Scale bars are 500 nm in a, b and 250 nm in c,d.

After the annealing procedure, the typically smooth walls of the nanotubes grown in nonaqueous organic electrolyte became highly rough. The FESEM micrographs (lateral view) reported in Fig. 3.8 show the morphological variation, even if the nanotubular shape was preserved. Albu et al. [19] have investigated with HRTEM the effect of temperature on the morphology of the nanotubes revealing that the crystallite formation lead to nanocracks occurrence along the walls when annealing temperatures approaches  $500^\circ\text{C}$ . Although on one hand this phenomenon can affect the electron transport properties of NTs, on the other hand it presents the advantage of an increase of the surface area, usually desirable in an electrochemical device.

### 3.2.3.2 Energy Dispersive X-ray spectrometry

Chemical composition of the nanostructured thin film was investigated using EDX analysis. The results on the as-grown material, shown in Fig. 3.9, reveal the presence of fluorine and

carbon atoms in addition to the expected titanium and oxygen atoms, as confirmed by the semi-quantitative standardless analysis (table inset in Fig. 3.9). This contamination is consistent with the results of Albu et al. [20] that describes the TiO<sub>2</sub> NTs as composed by two layers: an outer shell of pure and dense TiO<sub>2</sub>, and an inner porous core containing incorporated electrolyte components. However, EDX spectrum shows that after the annealing at 450 °C, fluorine and carbon disappear, thus resulting in an optimal control of the oxide stoichiometry.

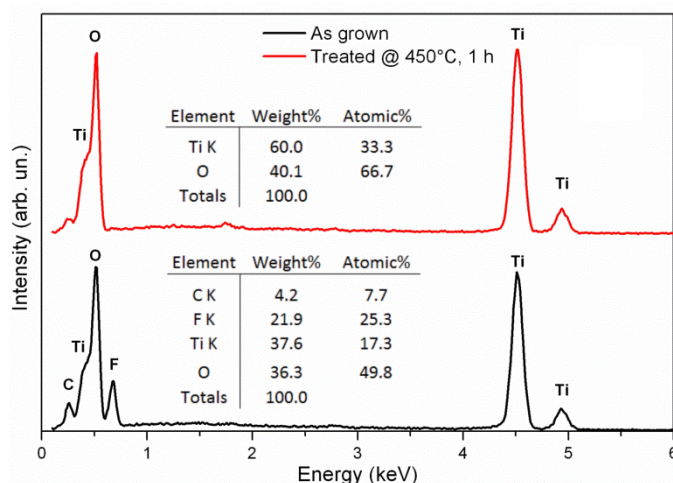


**Figure 3.9** EDX spectra of TiO<sub>2</sub> NTs before and after annealing and (insert) semi-quantitative standardless compositional analysis.

### 3.2.3.3 Surface area analysis

Figure 3.10 shows the nitrogen adsorption/desorption isotherms of TiO<sub>2</sub> NTs array. The specific surface area as measured by BET is about 40 m<sup>2</sup>/g, in line with the value measured for TiO<sub>2</sub> nanotubes array obtained by anodic oxidation in organic electrolyte [12].

The pore size analysis, reported in the inset of Fig. 3.10, shows a broad bell-shaped distribution. This result takes into account the contributions of the free volume among adjacent tubes and the roughness induced in the tube walls by the thermal treatment. After the annealing procedure, in fact, the typically smooth walls of the nanotubes grown in nonaqueous organic electrolyte became highly rough (see Fig. 3.8).

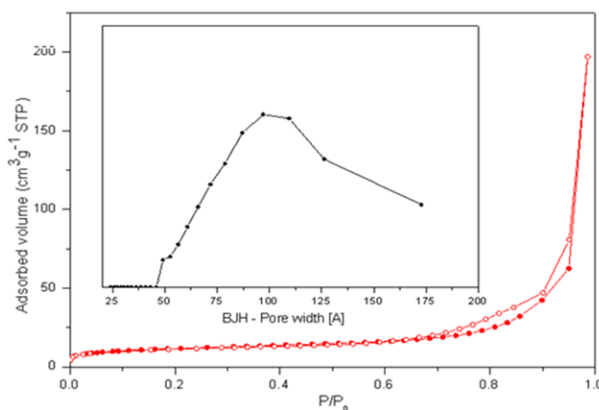


**Figure 3.10** N<sub>2</sub> adsorption/desorption isotherms for the surface area evaluation of TiO<sub>2</sub> NTs (pore size distribution is shown in the inset).

### 3.2.3.4 X-ray diffraction analysis

The XRD pattern, reported in Figure 3.11, shows the completely amorphous nature of the NT array after anodic oxidation while a crystalline anatase film was obtained after the thermal treatment.

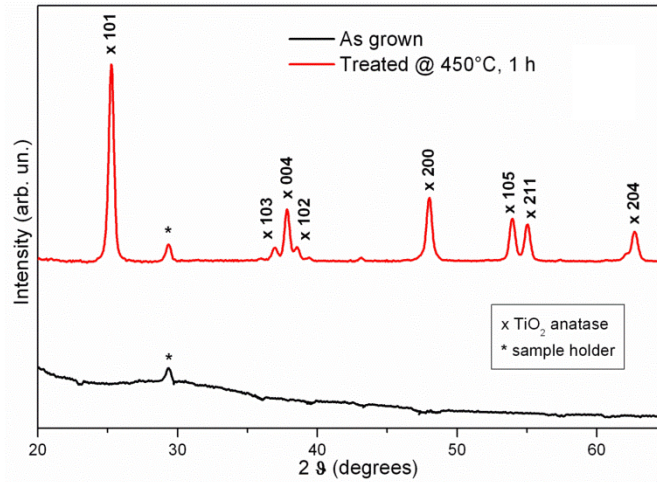


**Figure 3.11** X-ray diffraction pattern of as-grown and annealed  $\text{TiO}_2$  NT array: the experimental data are in perfect agreement with JCPDS reference patterns (89-4921), both in peak positions and relative intensities.

An interesting empirical observation is that XRD spectra are different if NTs have length lower than  $10\ \mu\text{m}$ . Measurements on bare Ti foil and upon oxidation and subsequent thermal treatment at  $450\ ^\circ\text{C}$  in air are reported in Fig. 3.12. The diffraction patterns reveal the formation of an anatase polycrystalline structure, with peaks related to the (101), (004), (200) and (105) crystal planes in the oxidized layer (JCPDS 89-4921), while the additional peaks originate from the Ti substrate (JCPDS 89-5009). The crystallites present a preferential orientation on the [004] direction, maybe related to the vertical orientation of the tubular structures. Extensive investigation is needed to verify this hypothesis.

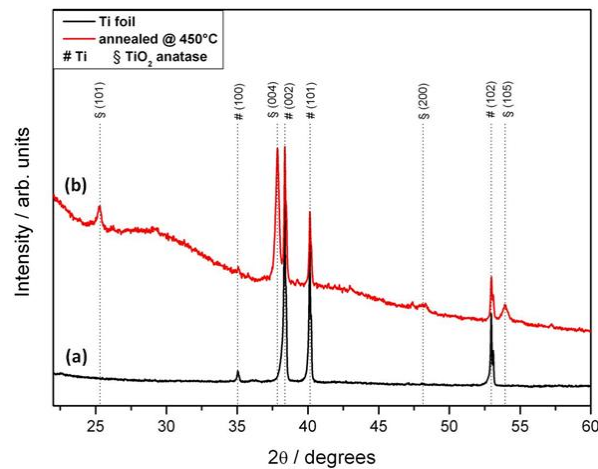


**Figure 3.12** X-ray diffraction patterns of Ti foil (a) and  $\text{TiO}_2$  NT array thermally treated at  $450\ ^\circ\text{C}$  (b). The diffractogram of the annealed material shows good agreement with the anatase phase reference pattern, with a (004) preferential orientation.

### 3.2.3.5 Transmission electron microscopy

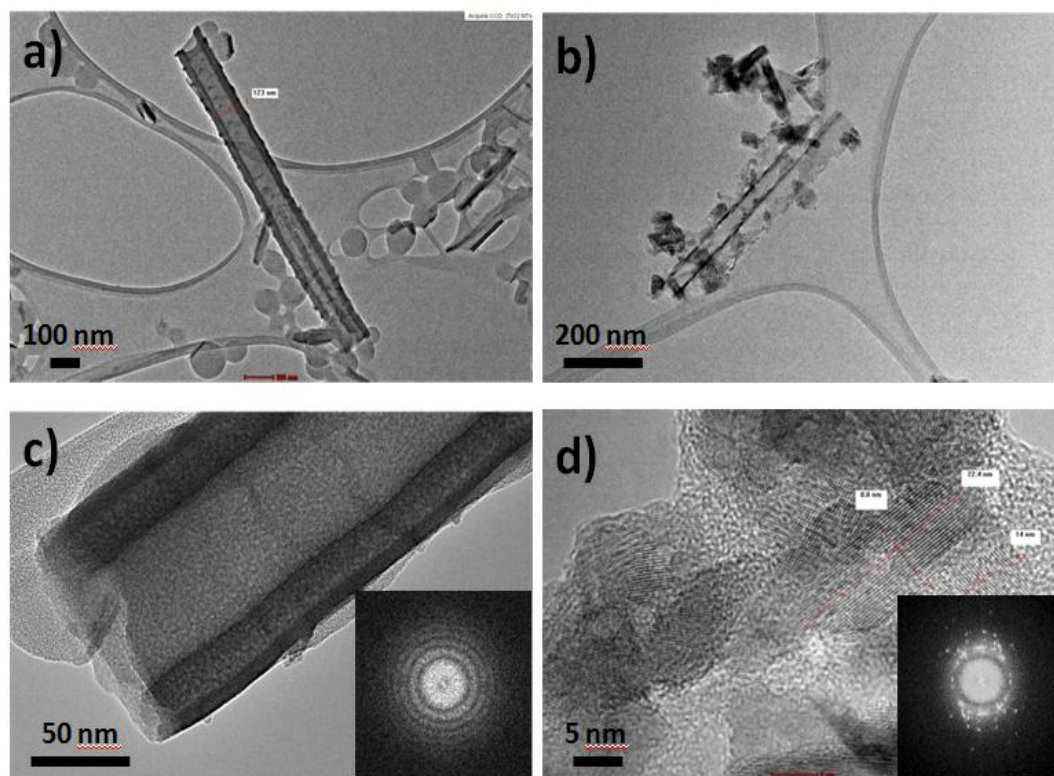


**Fig. 3.13** Bright Field TEM and HRTEM images of the as grown TiO<sub>2</sub> NTs (a-c), and of the annealed TiO<sub>2</sub> NTs (b-d). In the inset of c and d, the SAED (selected area electron diffraction) pattern related to the as grown and annealed TiO<sub>2</sub> NT respectively is reported.

In figure 3.13, some TEM images of the as-prepared and the annealed NT array are shown. In fig 3.13 a-c, a bright field TEM, a HRTEM images and the related SAED pattern of the as grown NTs are reported. From the SAED it is easy to confirm the amorphous nature of the as grown TiO<sub>2</sub> NTs.

In fig 3.13 b-d, the bright field TEM, the HRTEM images and the related SAED pattern of the NTs annealed at 450 °C are reported. The HRTEM images and a SAED pattern put in evidence the polycrystalline nature of the nanostructure. A measure of the d spacing (0.335 nm) of some selected crystal corresponds to the (101) of the anatase phase.

### 3.2.3.6 UV/Vis measurements

In order to study the optical properties of TiO<sub>2</sub> nanotubes, their UV-vis absorption and transmittance spectra were measured after detachment of the NTs membrane from the Ti foil and bonding on a glass substrate (as it will be explained in chapter 4). In Fig. 3.14(a) the transmittance results obtained on a 12 μm thick sample are reported. The membrane presents an opaque behavior and the visible transmittance is below 5%. The absorbance spectrum has been obtained from diffuse reflectance measurements and is shown in Fig. 3.14(b). The typical TiO<sub>2</sub> absorption edge -assigned to the intrinsic transition from the valence band (VB) to the conduction band (CB) is located around 390 nm and for longer wavelengths the curve is rather flat, revealing a low light absorption in the region 400-800 nm. This confirms the good quality of the material, since in nanostructured TiO<sub>2</sub>

samples the increase in the visible absorption is attributed to increased sub-gap defects and/or oxygen vacancies concentration [21].

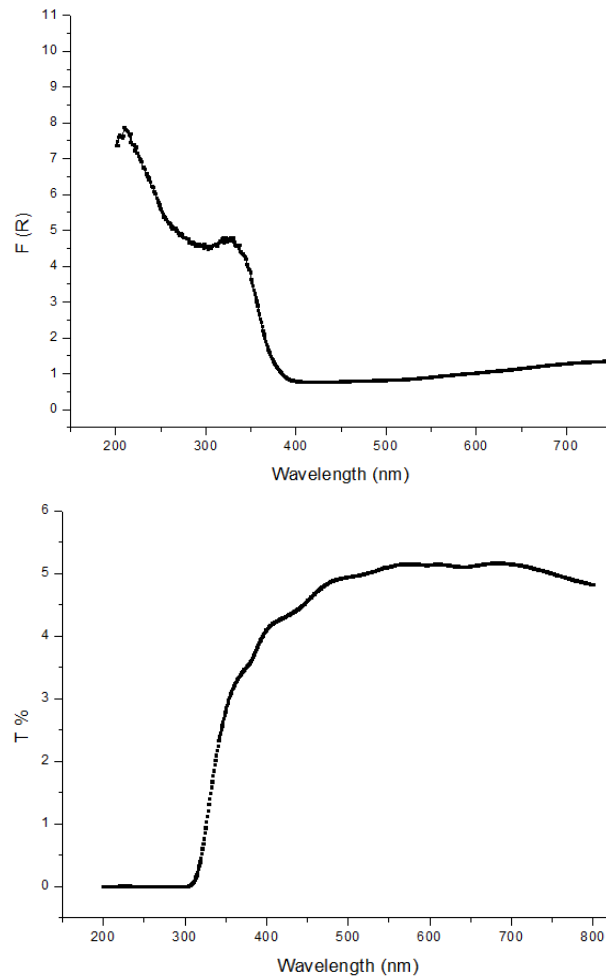


**Fig. 3.14** UV-Vis absorbance  $F(R)$  calculated with Kubelka-Munk function [22] and transmittance spectra of a 12  $\mu\text{m}$  thick  $\text{TiO}_2$  NTs membrane detached from the Ti foil and bonded on transparent substrate (as it will be explained in chapter 4).

### 3.2.3.7 Contact angle measurement

Contact angle measurements were performed to understand the wettability behavior of  $\text{TiO}_2$  NTs array on Ti substrate. The results show that after anodic oxidation of Ti foil, the amorphous NTs layer exhibits a super-hydrophobic behavior (see Fig. 3.15a). The recorded water CA value is around  $167^\circ$  and it is extremely reduced after the thermal treatment down to  $36^\circ$  as show in Fig. 3.15b. The highly super-hydrophobic behavior of as-grown NTs could be explained taking into account the carbon contaminant presence (as reported in paragraph 3.2.3.2). Organic functionalization of the NTs surface can in fact lead to an increase of the CA value [23].

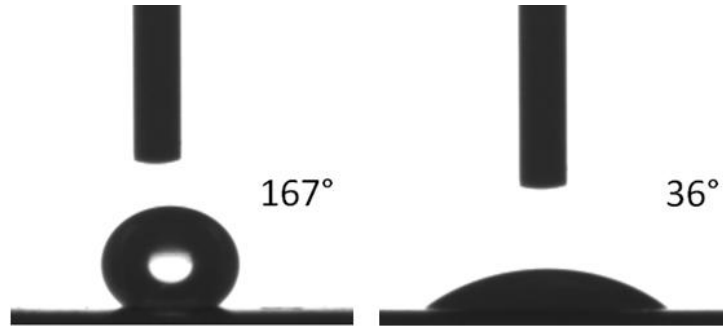


**Fig. 3.15** Photographs showing the DI-water contact angle images of TiO<sub>2</sub> NT array before (on the left) and after (on the right) the thermal treatment at 450°C.

The increase in wettability of NTs after the thermal treatment was previously reported [24]. In general, annealing metal generates a hydrophobic surface [25]. Conversely, this study produced more hydrophilic surfaces after annealing. The annealing resulted in nanotubes of anatase phase, causing more hydrophilic surfaces to be generated.

### 3.2.3.8 Electrical measurements

Around 6  $\mu\text{m}$  thick TiO<sub>2</sub> nanotube arrays on titanium foil were used as samples for electrical measurements. The I-V curves of as-grown and annealed samples are shown in Fig. 3.16. Both samples exhibit a linear relationship between the applied voltage and the measured current, evidencing the formation of an ohmic contact at the Au/TiO<sub>2</sub> interface. The as-grown sample is characterized by a higher resistance with respect to the annealed one, of the order of  $5 \cdot 10^7 \Omega$ , in line with what is reported in literature for amorphous nanotube used as oxygen sensor in ambient condition [26]. The annealed sample, instead, thanks to its polycrystalline nature, exhibits a five-order magnitude lower resistivity (as it is evident from the inset of Fig. 3.16) with a calculated value of  $2.5 \cdot 10^4 \Omega \cdot \text{cm}$ , in agreement with the typical values for polycrystalline TiO<sub>2</sub> anatase films ( $10^2$ – $10^7 \Omega \cdot \text{cm}$ ) [27]

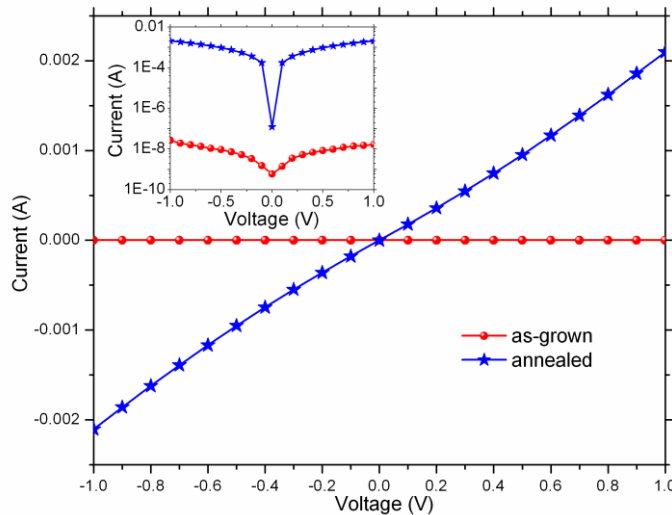


**Fig. 3.16** I-V curves of as-grown and annealed samples (semilog. scale is shown in the inset )

### 3.3 ZnO

#### 3.3.1 Growth process

The fabrication of ZnO sponge-like nanostructures starts with the RF sputtering deposition of a Zn porous layer. For a wide range of experimental condition the deposition on Zn layers gives evidence of the formation of a porous nanostructured film characterized by a spongelike morphology. This growth results can be explained in the framework of the growth model proposed by Jankowski and Hayes [28], a study that can be considered as an integration to the Thornton model [29], which is, in turn, an extension of the model proposed by Movchan and Demchinshin [29]. This model, also known as “structure zone” model (see Fig. 3.17), predicts that the structure and the morphology of a sputtered metal layer depend strongly on the ratio  $T/T_m$ , where  $T$  is the substrate temperature and  $T_m$  is the coating-material melting point, with the formation of three structural zones. Zone 1 consists of tapered crystals separated by voided boundaries. Zone 2 consists of columnar grains separated by distinct and dense intercrystalline boundaries. Zone 3 is composed of equiaxed grains with a bright surface. Thornton introduced a transition region, the so-called Zone T, standing between Zone 1 and Zone 2, characterized by a more fibrous morphology. Jankowski and Hayes introduced an additional zone corresponding to what they defined a stable “spongelike” morphology, between Zone T and Zone 2. This zone can be obtained at a substrate temperature lying in a range centered at  $T/T_m \sim 0.5$ , where surface diffusion still dominates but the onset of faceting that plays the dominant role in Zone 2 occurs. In the case of zinc, that has a low melting temperature ( $\sim 690$  K), the substrate temperature required for obtaining a value of 0.5 is  $\sim 350$  K. The substrate temperature can increase by tens of degrees Celsius during sputtering deposition because of the energy released by incident particles [30], thus the conditions for obtaining such a nanostructure are easily achieved with no intentional heating.

The effect of the subsequent thermal treatments that allow the conversion of Zn spongelike film into ZnO layer is discussed in the results and discussion section.

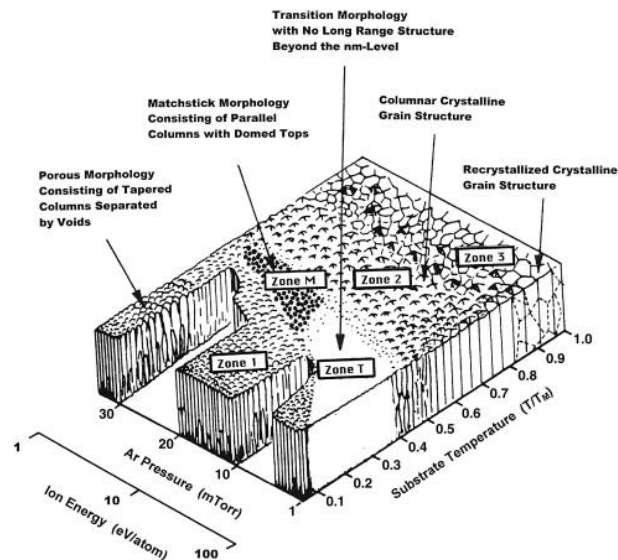


**Figure 3.17** Thornton model [29], also known as “structure zone” model, predicts three structural zones as a function of the ratio  $T/T_m$ , where  $T$  is the substrate temperature and  $T_m$  is the coating-material melting point.

### 3.3.2 Synthesis procedure

Zinc films were deposited on silicon substrates and on FTO-coated glasses by the RF magnetron sputtering technique. Substrates were cleaned in ultrasonic bath with acetone (10 min) and ethanol (10 min), and dried under direct nitrogen flow. The vacuum chamber was pumped down to a pressure ranging from about  $8 \times 10^{-6}$  Pa to about  $6 \times 10^{-5}$  Pa. A zinc target, was fixed on the cathode, placed at about 8 cm from the substrate holder. Argon was used as sputtering gas. The plasma discharge was created by applying a RF voltage at a frequency of 13.56 MHz between the target and the grounded substrate holder. Each film was grown at room temperature, i.e., no intentional heating was supplied to the substrates and at a deposition power of 100W. After the deposition by sputtering, the films were placed on a hot plate at 380°C for 60 min in ambient air, in order to oxidize the zinc and obtain zinc oxide nanostructured layers.

### 3.3.3 Results and discussion

#### 3.3.3.1 *Field emission scanning electron microscopy*

Fig. 3.18a and b shows the FESEM cross-section images of the zinc films deposited at different gas flow and pressure values (40 sccm / 0,67 Pa and 10 sccm / 2.67 Pa respectively), while the FESEM top views of the same samples are shown in Fig. 3.18c and d. For a fixed deposition time (60 min) the thickness of the films ranged between about 1.4  $\mu\text{m}$  and 4.3  $\mu\text{m}$ . The thickness values were vastly different because of the deposition conditions adopted for the growth of the films, and their variation was consistent with the mechanisms of growth involved in a sputtering process.

For every deposition condition all the samples showed the same kind of nanostructure, some effects due to the variation of gas flow and pressure could be noticed at a lower scale: in particular, in films grown at 10 sccm and 2.67 Pa of Ar, particulate formation was observed along the surface of the film structure. Moreover, the images related to the sample reported in Fig. 3.18b and d seem to suggest that this sample is characterized by a more compact structure than that of the other samples, regardless of the gas flow value. Concerning this behavior, it has been reported that an increase in the working gas pressure has the same effect as reducing the substrate temperature [28].

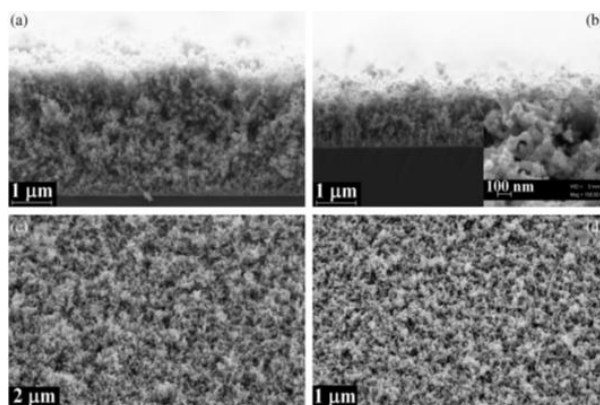


**Figure 3.18** FESEM micrographs showing the cross-sections and the top views of Zn films deposited at 40 sccm / 0,67 Pa (a, c) and sample deposited at 10 sccm / 2.67 Pa (b, d). The bottom right inset in (b) shows a high-magnification micrograph acquired on sample deposited at 10 sccm / 2.67 Pa in cross-section in which the presence of particulates along the main film structure is evident.

Therefore the shift towards a denser structure for pressures above and below 0.67 Pa corresponds to an initial transition towards Zone T and Zone 2 of the Thornton model, respectively. In all the reported conditions, the morphology of the films was found to be independent of the substrate (Si or glass covered with FTO) used for the deposition.

In order to better investigate the morphology of the first layers of the deposited material, a series of depositions with a reduced deposition time (2 min) was performed. Fig. 3.19a and b reports two examples of FESEM micrographs of zinc thin films grown at the same conditions as before (40 sccm / 0,67 Pa and 10 sccm / 2.67 Pa respectively) acquired at different magnifications.

Sample deposited at 40 sccm / 0,67 Pa for 2min (Fig. 3.19a) was composed of smooth particulates with an average diameter of about 20 nm, whereas sample deposited at 10 sccm / 2.67 Pa for 2 min, so grown at lower Ar flow, was characterized by a doubled thickness value and by a rough structure composed of agglomerated particulates (Fig. 3.19b).

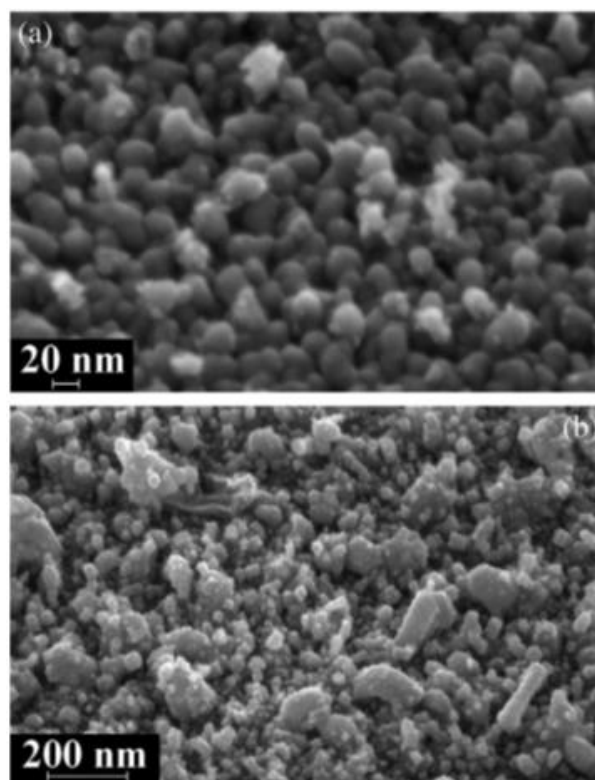


**Figure 3.19** FESEM micrographs of Zn films showing the top view of sample deposited at (a) 40 sccm / 0,67 Pa and (b) 10 sccm / 2.67 Pa respectively for 2 min, both tilted by 45°.

Moreover, numerous elongated structures, up to 200 nm in length, were present across the whole surface: their sharp morphology could indicate a higher degree of crystallinity but it could be also related to the growth mechanisms occurring at different stages of the film growth. In fact, the elongated structures might develop after the initial formation of few layers of quasi-spherical particulates.

In order to prove the possibility of obtaining ZnO nanostructured layers from the zinc films deposited by sputtering, all the thick samples were oxidized by thermal treatment in air at 380°C and examined by FESEM: their morphology was preserved after the treatment. This is an important result when considering the application of these films into

DSCs or Li-Ions battery, because this morphology is particularly suitable for dye or electrolyte impregnation.

The as-grown Zn thin film is characterized by a black appearance, due to the high light scattering at the surface indicating the nanostructured nature of the layer. After the oxidation treatment, the color of the thin film turns white, which is the typical look for ZnO porous film (see insets Fig.3.20a-b).

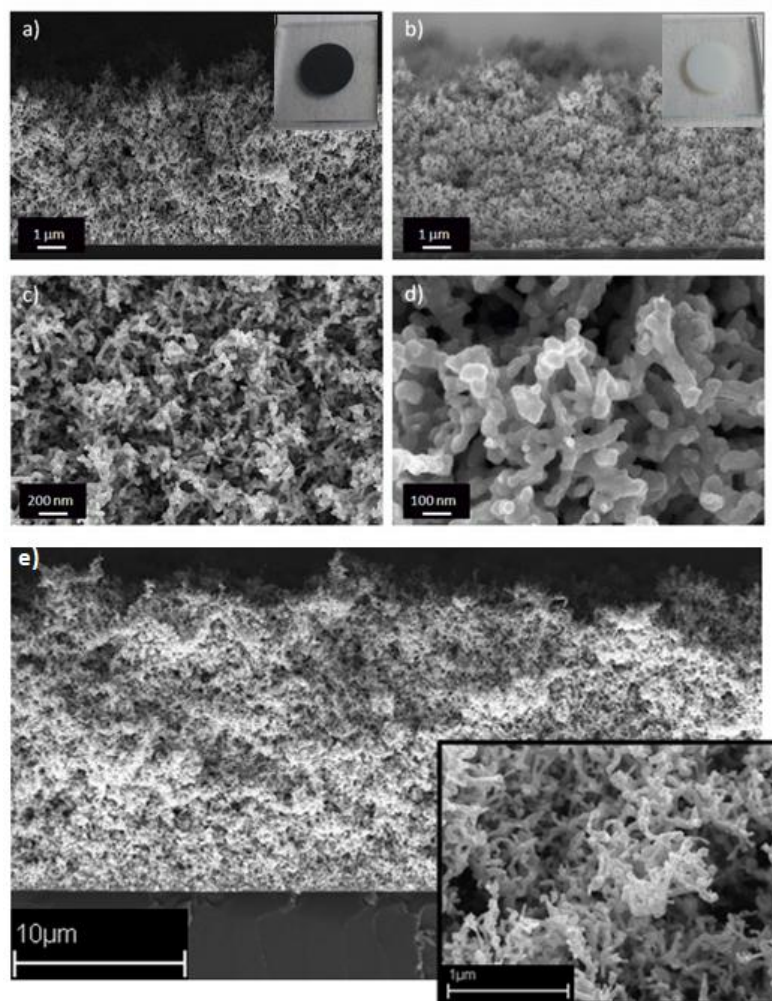


**Figure 3.20** FESEM morphological analyses of as-grown and oxidized Zn layer. (a) A cross-sectional view of 5  $\mu\text{m}$  thick nanostructured Zn and (b) ZnO; c) and d) show higher magnification of b). Increasing the deposition time up to 10 hours, a 18.5  $\mu\text{m}$  thick Zn layer could be obtained (e). In the insets of a-b photograph of photoanodes before (left) and after (right) thermal oxidation are reported.

Fig. 3.20a-d shows FESEM images of Zn (a) and ZnO (b-d) nanostructures, evidencing a sponge-like nanostructure. In Fig. 3.20a-b a cross-sectional view of the film before and after oxidation is proposed, where it is possible to notice how the films are actually constituted by a thin highly dense layer at the interface with FTO and by a thick, porous and branched structure up to the surface of the film. After the thermal oxidation, the structures maintain almost the same morphology of the as-grown sample, with a moderate volume expansion.

Although Zn and ZnO films have similar morphology, some small differences can be noticed. The as-grown Zn film consists of branches that are slightly more elongated than those of the ZnO film.

The coral-like arrangement of the thick ZnO layer is shown in higher magnification FESEM pictures in Fig. 3.20c-d. The diameter dimensions of the branches are of the order of 40 nm, with spacing in the range 10-60 nm: taking into account an exciton length of 5-20 nm [31], they should guarantee for optimal electron transfer properties for the DSC and Li-ion batteries applications.

Thicknesses up to 18.5  $\mu\text{m}$  (see fig 3.20e), maintaining almost the same sponge like morphology, can be obtained by simply increasing the deposition time (10 hours).

### 3.3.3.2 Energy dispersive X-ray spectrometry

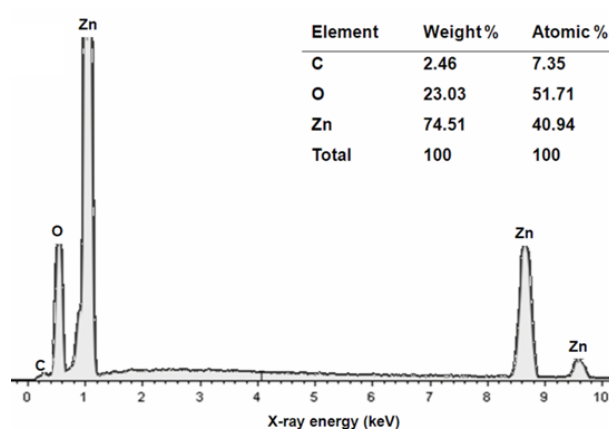


**Figure 3.21** EDX spectrum of ZnO sponge-like film and (insert) semiquantitative standardless compositional analysis.

Chemical composition of the nanostructured thin film was investigated using energy dispersive X-ray analysis. The results, shown in Fig. 3.21, confirm the presence of almost stoichiometric zinc oxide, as evidenced by the semiquantitative standardless analysis (table inset in Fig. 3.21).

### 3.3.3.3 Surface area analysis

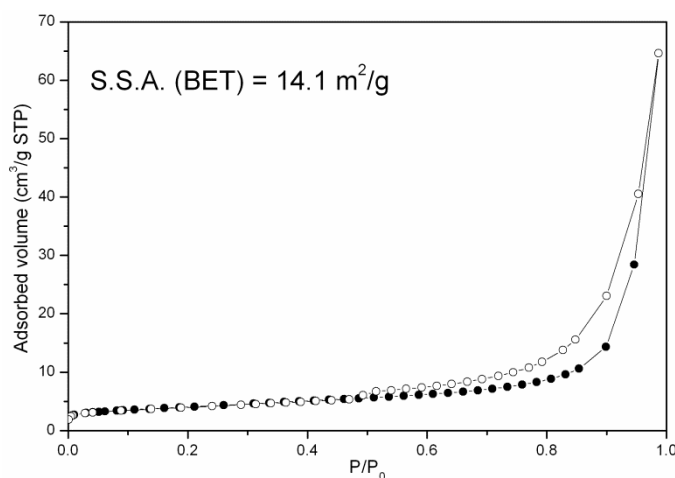


**Figure 3.22**  $\text{N}_2$  sorption isotherms for the surface area evaluation obtained on sponge-like ZnO film.

The nitrogen sorption isotherm is reported in Fig. 3.22. Shape and position of the hysteresis loops are compatible with the branched porous ZnO structure and the calculated specific area is  $14.1 \text{ m}^2/\text{g}$ . This value is lower than in nanoparticulated  $\text{TiO}_2$  electrodes usually employed in DSC, but comparable to that of other ZnO layer reported in literature [32-33].

### 3.3.3.4 X-ray diffraction analysis

The diffraction patterns of the as grown and oxidized films are reported in Fig. 3.23. The strongest peaks in the Zn XRD pattern are related to Zn (002), (100) and (101) crystalline planes, while weaker peaks correspond to ZnO (100) and ZnO (002) planes. The diffraction pattern of ZnO point out the good crystalline quality of the film, with the presence of a pure hexagonal structure. A good control of the oxide stoichiometry is evidenced, since no peaks related to metallic Zn are present after the thermal treatment (JCPDS references: Zn 87-0713, ZnO 89-1397).

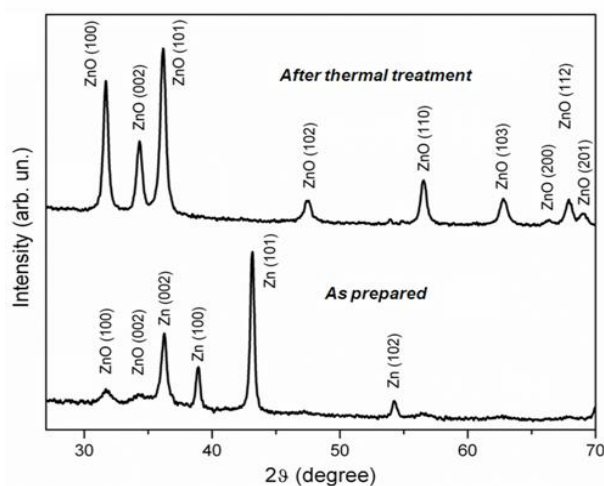


**Figure 3.23** X-ray diffraction pattern of as grown and oxidized films, showing the complete oxidation of Zn after thermal treatment. The experimental data are in perfect agreement with JCPDS reference patterns (Zn 87-0713, ZnO 89-1397), both in peak positions and relative intensities.

### 3.3.3.5 Transmission electron microscopy

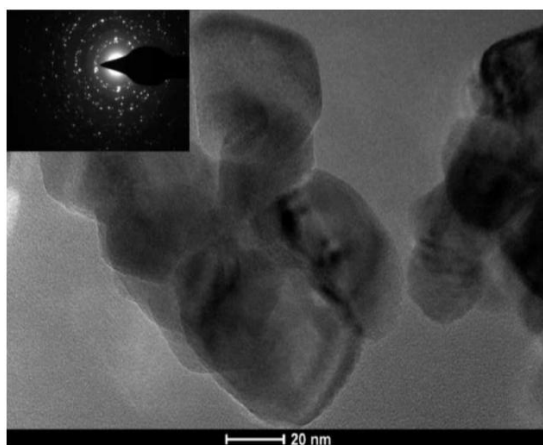


**Figure 3.24** TEM image of the ZnO powder obtained from the ZnO film synthesized on silicon. The inset represents the related SAED (selected area electron diffraction) pattern.

Fig. 3.24 shows a bright field TEM image acquired on the ZnO powder prepared according to the method described in the previous section (3.2.2). The image represents a portion of a branch of the ZnO film, in which the aggregation of different crystals is visible. The rings present in the diffraction pattern (inset of Fig. 3.24) evidence the polycrystalline nature of the material: the spongelike structure is, in fact, composed of randomly oriented crystals of few tens of nanometers ( $\approx 20$ -40). Because of the specimen preparation method, it was not possible to infer an orientation relation with the substrate.

### 3.3.3.6 UV/Vis measurements

The UV-visible transmittance spectra of spongelike Zn, ZnO and nanoparticulated TiO<sub>2</sub> films with same thickness (8  $\mu\text{m}$ , as comparison) deposited on the same kind of substrates were measured and compared. The optical spectra are reported in Fig. 3.25, where the effect of the thermal oxidation on the Zn film is evident: the transmittance was approximately zero for the metallic film while a semi-transparent layer was obtained after the oxidation. Moreover ZnO presents a transmittance of about 15% higher (for wavelengths above 500 nm) than that of TiO<sub>2</sub>. Such a higher transmittance obtained with ZnO is really promising for transparent DSC for solar windows applications.

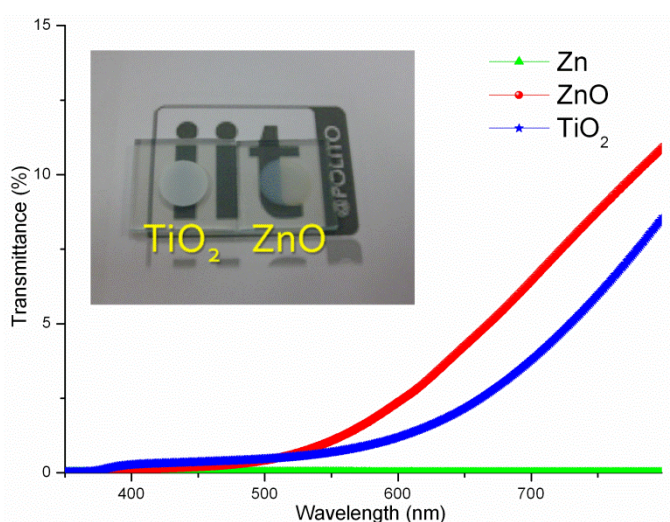


**Figure 3.25** UV-visible transmittance curves obtained for the Zn, ZnO and TiO<sub>2</sub> layers on transparent conductive substrates with the same thickness (8  $\mu\text{m}$ ). The two metal-oxide photoanodes are visualized in the inset.

### 3.3.3.7 Contact angle measurements

The wettability of the Zn layer drastically changes after oxidation, moving from superhydrophobic to superhydrophilic behavior for Zn and ZnO respectively (Fig. 3.26 a-b). Moreover, the oxide surface showed a good affinity with ethanolic solution (Fig. 3.26c), as the one used for dye impregnation step in DSCs fabrication.

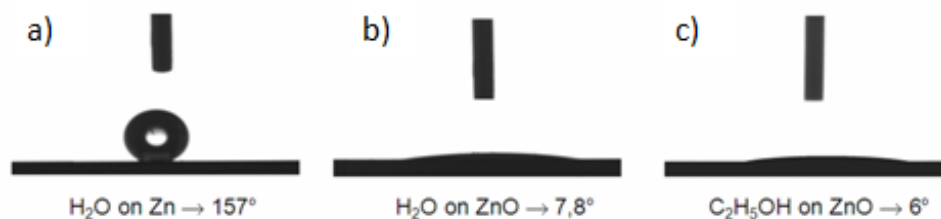


**Figure 3.26** Contact angle images of DI-water on Zn (a) and ZnO (b) and ethanol on ZnO (c).

### 3.3.3.8 Electrical measurements

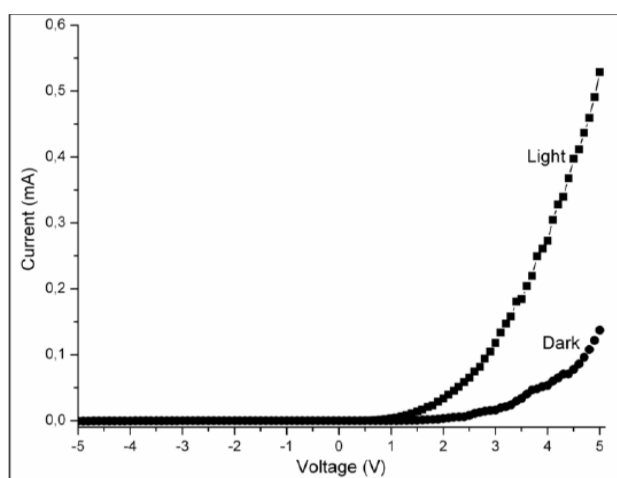


**Figure 3.27** I-V curves obtained from ZnO under dark conditions and under illumination.

Around 3  $\mu\text{m}$  thick ZnO spongelike films on silicon on insulator (SOI) wafers coated with Ti/Au (10 nm/100 nm) metal layers were used as samples for electrical measurements. I-V curves are shown in Fig. 3.27 and represent a Schottky-type potential barrier. This non-linear characteristic is frequent in ZnO-Au junctions [34], and, more in general, it is consistent with the behavior of materials with charged grain boundaries, whose electrical properties are dominated by grain-boundaries interface states [35]. Under dark conditions the current-vs-voltage characteristic is only dependent on the polarization conditions. Under illumination, the current strongly increases thanks to the contribution of the electron-hole couples photogenerated upon absorption of light in the UV range of the solar spectrum. Thus, as it has been reported for compact thin films [36], the interface between gold and spongelike ZnO can operate as photodetector.

## 3.4 References

- [1] P. Roy, S. Berger. *Angew. Chem. Int. Ed.* 50 (2011) 2904.
- [2] L. Young. *Anodic oxide films*. New York: Plenum; 1961.
- [3] F. Keller, M. S. Hunter, D. L. Robinson. *J. Electrochem. Soc.* 100 (1953) 411.
- [4] J. F. Vanhumbecq, J. Proost. *Electrochim. Acta* 53 (2008) 6165.
- [5] O. Jessensky, F. Miller, U. G. sele. *Appl. Phys. Lett.* 72 (1998) 1173.
- [6] S. Ono, M. Saito, M. Ishiguro, H. Asoh. *J. Electrochem. Soc.* 151 (2004) B473

- [7] J.M. Macak, H. Tsuchiya, A. Ghicov, K. Yasuda, R. Hahn, S. Bauer, P. Schmuki. *Current Opinion in Solid State and Materials Science* 11 (2007) 3.
- [8] V. Zwillling, E. Darque-Ceretti, A. Boutry-Forveille, D. David, M.Y. Perrin, M. Aucouturier. *Surf. Interface. Anal.* 27 (1999) 629.
- [9] J.M. Macak, H. Tsuchiya, P. Schmuki. *Angew. Chem.* 44 (2005) 2100.
- [10] J.M. Macak, H. Tsuchiya, L. Taveira, S. Aldabergero, P. Schmuki. *Angew Chem Int Ed* 44 (2005) 7463.
- [11] M. Paulose, H.F. Prakasam, O.K. Varghese. *J Phys Chem C* 111 (2007) 14992.
- [12] P. Roy, S. Berger, P. Schmuki, *Angew. Chem. Int. Ed.* 50 (2011) 2904.
- [13] N. B. Pilling, R. E. Bedworth. *J. Inst. Met.* 29 (1923) 529.
- [14] H. Habazaki, M. Uozumi, H. Konno, K. Shimizu, S. Nagata, K. Takayama, Y. Oda, P. Skeldon, G. E. Thompson. *J. Electrochem. Soc.* 152 (2005) B263
- [15] P. Skeldon, G. E. Thompson, S. J. Garcia-Vergara, L. Iglesias- Rubianes, C. E. Blanco-Pinzon. *Electrochem. Solid-State Lett.* 9 (2006) B47.
- [16] G. Liu, K. Wang, N. Hoivik, H. Jakobsen. *Sol. Energ. Mat. Sol. C.* 98 (2012) 24.
- [17] S.P. Albu, A. Ghicov, J.M. Macak, P. Schmuki. *Phys. stat. sol. (RRL)* 1 (2007) R65.
- [18] Y. Shin, S. Lee. *Nano Lett.* 8 (2008) 3171.
- [19] S. P. Albu, H. Tsuchiya, S. Fujimoto, P. Schmuki. *Eur. J. Inorg. Chem.* 2010 (2010) 4351.
- [20] S. P. Albu, A. Ghicov, S. Aldabergenova, P. Drechsel, D. LeClere, G. E. Thompson, J. M. Macak, P. Schmuki. *Adv. Mater.* 20 (2008) 4135
- [21] C.H. Chen, J. Shieh, S.M. Hsieh, C.L. Kuo, H.Y. Liao. *Acta Materialia* 60 (2012) 6429.
- [22] S. K. Loyalka, C. A. Riggs. *Applied Spectroscopy*, 49 (1995) 1107.
- [23] E. Balaur et al. *Electrochemistry Communications* 7 (2005) 1066.
- [24] D. HShin et al. *Nanotechnology* 22 (2011) 315704.
- [25] V.R. Shinde, C.D. Lokhande, R.S. Mane S.H. Han. *Appl.Surf. Sci.* 245 (2005) 407.
- [26] H.F. Lu et al. *Nanotechnology* 19 (2008) 405504.
- [27] C Fabrega et al. *Nanotechnology* 21 (2010) 445703.
- [28] A.F. Jankowski, J.P. Hayes. *J. Vac. Sci. Technol. A* 21 (2003) 422.
- [29] J.A. Thornton. *Annu. Rev. Mater. Sci.* 7 (1977) 239.
- [30] J. Musil, J. Matouš, V. Valvoda. *Vacuum* 46 (1995) 203.
- [31] Gonzalez-Valls I, Lira-Cantu M. *Energy & Environmental Science* 2 (2009) 19.
- [32] C. Cheng, Y. Shi, C. Zhu, W. Li, L. Wang, K. K. Fung, N.Wang. *Phys. Chem. Chem. Phys.* 13 (2011) 10631.
- [33] W. Chen, Y. Qiu, S. Yang. *Phys. Chem. Chem. Phys.* 12 (2010) 9494.
- [34] B.J. Coppa, R.F. Davis, R.J. Nemanich. *Appl. Phys. Lett.* 82 (2003) 400.
- [35] P.R. Bueno, J.A. Varela, E. Longo. *J. Eur. Ceram. Soc.* 28 (2008) 505.
- [36] H. Fabricius, T. Skettrup, P. Bisgaard. *Appl. Opt.* 25 (1986) 2764.

## Chapter 4

### Technological processes for DSC fabrication and characterization

In this chapter all the technological steps for the fabrication and characterization of microfluidic front-side illuminated dye-sensitized solar cells are discussed.  $\text{TiO}_2$  and  $\text{ZnO}$  photoanodes were obtained by anodic oxidation and sputtering deposition combined with thermal oxidation respectively and implemented into microfluidic DSCs. The devices were electrically characterized and the charge transport properties deeply investigated.

#### 4.1 Microfluidic housing system

Several papers have been published suggesting the best fabrication procedure of the cells [1-2] and moreover, in the papers reporting experimental results, the procedure used to obtain small laboratory cells is quite always illustrated in details. Even if sometimes a simple clips closure has been chosen, the use of hot-melt sealants is generally adopted for closure and protection from the environment. For research purposes this can be somewhat limiting. Indeed some of the fabrication steps, as dye adsorption and electrolyte filling, are often performed without any direct/active control, being difficult to ensure reproducibility and reliability while fabricating a large number of cells. Both during experiments and after them, the cell, being irreversibly sealed, does not grant the possibility of control and inspection, or post-process modifications. Recently the CSHR@PoliTo laboratory [3] has proposed a new technological procedure for DSC fabrication, which is quite familiar to the field of microfluidics (see figure 4.1). We designed a cell that is actually made by all the parts of the traditional Grätzel's device, in which a microfluidic chamber has been designed by means of a PolyDiMethylSiloxane (PDMS) membrane. PDMS exhibits a good spontaneous reversible adhesion to glass, metals and oxides. The membrane acts as a spacer between the two electrodes, defining the inner active volume of the DSC. To ensure a good sealing, the semiconductor layer ( $\text{TiO}_2$  or  $\text{ZnO}$ ) is designed having a circular shape entirely confined into the microfluidic chamber. This is obtained performing a casting step into a tape-mould having a hole with a fixed diameter into it. To definitively close the device, a housing system has been designed, with an external clamp closed by screws. In this way the sealing procedure is reversible, granting inspection and control also after the experiments. Sealing performances of such innovative structure were

successfully evaluated by dynamic fluidic tests[3]. The microfluidic device offers good flexibility and still grants low cost materials and technologies together with the use of very small amounts of reagents. This modular device enables to substitute one or more components and guarantees the reproducibility of the assembly parameters such as load distribution, screw tightening, spacer and thicknesses control.

The  $\text{TiO}_2$  NTs and ZnO spongelike photoanodes fabrication will be discussed in paragraph 4.3 and 4.4. Here the adopted procedure for obtaining the microfluidic dye sensitized solar cell is reported.

To fabricate the counter electrodes for DSCs, two small pin-holes for inlet/outlet connections were drilled in the FTO glass (7  $\Omega/\text{sq}$ , Solaronix) through powder blasting technique. Substrates were then cleaned with the same rinsing method described in detail below. A thin layer of platinum was deposited by thermal evaporation. A 0.125 mm Pt wire (99.99% purity, Goodfellow) was putted in a W crucible (ME5.005W, Testbourne) and connected with a high current circuit controlled by a variac. The evaporation current was in the range 90-110 A, as measured by a clamp meter. Deposition occurs in high vacuum conditions (pressure lower than  $5\text{E-}7$  mbar), guaranteed by a series of a mechanical and a turbomolecular pump. The distance between the metal source and the substrate was 10 cm. The thickness of the deposited layer was measured by a quartz crystal microbalance and the deposition rate was maintained constant at 0.01 nm/s. The inlet/outlet ports for electrolyte (Iodolyte AN 50, Solaronix) filling were connected via low density polyethylene tubes and closed for operation with PDMS caps.

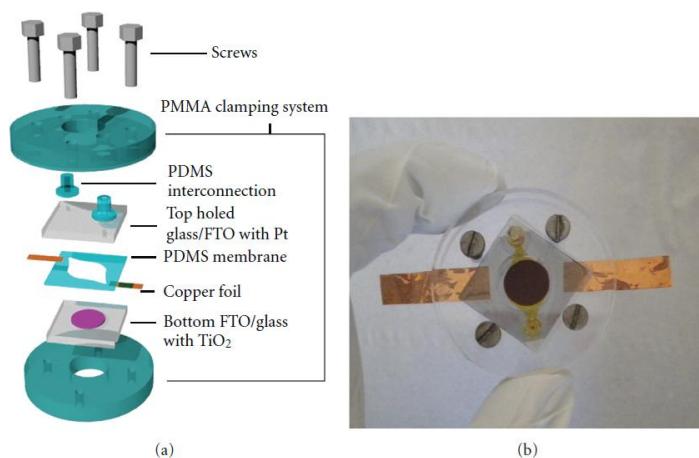


**Fig. 4.1** (a) Scheme of the microfluidic DSC with the detail of all the elements constituting the Cell and (b) a photograph of the final device.

The operating chamber was defined through a PDMS membrane, prepared by casting technique. PDMS pre-polymer and curing agent (Sylgard 184, Dow Corning) were mixed in a 5:1 weight ratio and degassed in low vacuum for 1 h. The mixture was then poured into the mould and cured in a convection oven for 1h at 70 °C. The membrane was then peeled off from the mould and reversibly sandwiched between the electrodes. Accurate control in the volume of the mould and on PDMS weight during casting process allowed a precise control in membrane thickness ( $200\text{ }\mu\text{m} \pm 15\text{ }\mu\text{m}$ ) and uniformity. The PDMS membrane laterally defines the active chamber of the cell. A double-drop membrane layout was chosen to promote air bubble evacuation during electrolyte filling. The device is closed by an external housing

system (made of two polymethyl methacrylate frames) that clamps the two electrodes and allows fluids handling. A 50  $\mu\text{m}$  retaining ring is designed on the membrane to follow the profile of the chamber ensuring sealing by completely deforming when closing the device with screws. The complete deformation of the retaining ring grants the final distance between the electrodes to coincide with the thickness of the membranes. In this way the sealing procedure is reversible, allowing inspection and control also after the experiments. All cells had an active area of 0.78  $\text{cm}^2$  and measurements were performed with a 0.22  $\text{cm}^2$  mask. Copper foils (50  $\mu\text{m}$  thick, area 1.5  $\text{cm}^2$ ) were used for electric connections at the electrodes, dielectrically isolated by the PDMS membrane.

## 4.2 Device characterization

When the microfluidic DSC assembling procedure was carried out, all the cells were characterized by electrical and electrochemical points of view. A theoretical background on photovoltaic parameters and characterization techniques is provided in 2.1.3. I-V electrical characterizations under AM1.5G illumination (1000  $\text{W}/\text{m}^2$ ) were carried out using a class A solar simulator (91195A, Newport) and a Keithley 2440 source measure unit. Incident photon-to-electron conversion efficiency measurements were performed using a 150 W Xenon halogen lamp equipped with a dual grating Czerny Turner monochromator and measuring the DC current through a Keithley 2440 source measure unit. Open circuit voltage decay measurements were performed using a 760D electrochemical workstation (CH Instruments). Electrochemical impedance spectra were acquired using the same electrochemical workstation in dark condition at different applied bias voltages; the amplitude of the AC signal was 10 mV and the frequency range was  $10^{-1} - 10^5$  Hz. The collected spectra were fitted using an equivalent circuit (a detailed description is reported in the paragraph 2.1.3.4) in order to obtain information about transport and recombination of charges.

## 4.3 $\text{TiO}_2$ based photoanodes

In this paragraph the fabrication step of titanium dioxide photoanodes are described and the morphological characterization is reported. Usually, the NT array grown onto the opaque Ti foil, once crystallized and dye-sensitized, can be used as DSC photoanode employing a backside illumination set-up [4,5]. In this configuration, the cell is illuminated from the counter electrode side, so the number of incident photons that can be absorbed by dye molecules is partially reduced by the absorption and the reflection on the Pt thin film. Moreover the iodine-based electrolytic solution between the two electrodes can absorb in the UV-region, further reducing the device performances. A possible alternative is to fabricate front-side illuminated NT-based DSC starting by Ti thin films deposited on transparent conductive substrate [4]. In this case, the relatively low film thickness attainable with common sputtering or evaporation techniques in reasonable time limits the maximum NT length achievable. To overcome these constraints, self standing  $\text{TiO}_2$  NT membranes can be anodically grown on Ti foil, detached and bonded on transparent sheet. Employing this approach, the characteristic blocking layer usually present at the interface between the bottom of the NTs and the bulky Ti foil can be avoided [6], thus reducing the recombination at this interface.

### 4.3.1 Fabrication/Technology

Titanium dioxide nanotube arrays were grown by a two-step anodic oxidation of Ti foil following the recipe described in chapter 3. After the anodization, the oxidized Ti foils were repeatedly rinsed in ethanol to remove the residual fluoride contaminants (see 3.2.3) and other impurities adsorbed from the electrolytic solution during the growth process. Different strategies have been presented in the literature to detach  $\text{TiO}_2$  NT membrane from Ti foil such as mechanical splitting, electrochemical extraction, chemical dissolution or physical etching [7]. Here, instead, a self-detachment procedure is proposed: following repeated rinsing of the sample the  $\text{TiO}_2$  barrier layer at the end of the tubes was delaminated and the NT array separated from the bulk.

The sol of  $\text{TiO}_2$  NPs used to obtain a good interface between the FTO and the  $\text{TiO}_2$  NT bottom was prepared by sol-gel technique. In a typical synthesis, Titanium (IV) isopropoxide was hydrolyzed using glacial acetic acid and excess of DI-water, according to a procedure similar to that previously described in literature [8]. The reaction media were modified introducing the non-ionic surfactant Tween 20, which helps in obtaining a better connectivity and homogeneity when the sol is casted to form a thin film. The sol was aged for 48 h at ambient temperature and subsequently concentrated in a rotary evaporator at 40 °C for 2 h under vacuum. The final sol containing amorphous  $\text{TiO}_2$  nanoparticles was homogeneous and stable for weeks.

FTO/glasses (7  $\Omega/\text{sq}$ , Solaronix) were cleaned in acetone in an ultrasonic bath and then rinsed with ethanol. A cleaning in “piranha” solution (3:1 concentration of Sulfuric Acid: Hydrogen Peroxide) was employed to remove organic residues on the surface.

With the purpose of investigating the effect of titanium tetrachloride some substrates were incubated into a 50 mM  $\text{TiCl}_4$  aqueous solution for 20 min at 70 °C, rinsed many times in DI-water, dried under  $\text{N}_2$  flow and heat treated again at 450 °C.

The as-prepared photoanodes were incubated for 18 h into a 0.3 mM N719 ethanolic dye solution at room temperature to obtain a dye molecules monolayer covering the semiconductor material.

In order to compare the properties of the  $\text{TiO}_2$  NTs and the sponge-like ZnO with the most commonly used material in DSCs,  $\text{TiO}_2$  nanoparticle-based photoanodes were also prepared, using commercial  $\text{TiO}_2$  paste. FTO covered glasses were cleaned and a  $\text{TiO}_2$  layer (Ti-Nanoxide D37 paste, Solaronix) with a circular shape was deposited on FTO by tape casting technique and dried at 50 °C for 30 min on a hot plate. A sintering process at 450 °C for 30 min allowed the formation of nanoporous  $\text{TiO}_2$  film with a mean thickness of  $(7.5 \pm 0.5) \mu\text{m}$ , as measured by profilometry (P.10 KLA-Tencor Profiler).

Another approach to exploit  $\text{TiO}_2$  nanotubes lie in the fabrication of  $\text{TiO}_2$  NT/NP composite electrodes. After the electrochemical growth, NTs were detached by the metal substrate exploiting a slight bending of the foil and ground into a fine powder using a jade mortar and pestle. NT powder was mixed under continuous grinding into commercial NP dispersion (Ti-Nanoxide D37, Solaronix), made up of 11wt.% of  $\text{TiO}_2$  nanoparticles (around 30 nm diameter) and a low amount of light-scattering nanoparticles (LS-NPs, with diameter in the range 100-300 nm). FTO covered glasses were cleaned as previously described and the  $\text{TiO}_2$  NT/NP composite pastes, fabricated including different NT content (0 wt%, 5 wt% and 10 wt%), were deposited onto FTO covered glasses with a squeezing method. The samples were dried at 70°C for 10 minutes then annealed at 450 °C for 1 hour to improve the anatase crystalline phase of the composite material and to electrically interconnect the NPs and the

NTs. Photoanodes were heated at 70 °C and soaked overnight (in dark condition) into a 0.25 mM N719 dye solution (Ruthenizer535bis-TBA, Solaronix) in ethanol at room temperature and then rinsed in ethanol again to remove the un-adsorbed dye molecules.

#### 4.3.1.1 $\text{TiO}_2$ nanotubes

The various steps involved in the fabrication process of the NTs-based transparent photoanode are described in Fig. 4.2. When the anodized Ti foil was removed from the electrochemical cell (Fig. 4.2a), NT membranes could be detached by the metal substrate without any crack following a self-detaching mechanism based on repeated rinsing in DI-water and ethanol (Fig. 4.2b). This is a very simple procedure since it does not involve any chemical etching or mechanical splitting, unlike what has been proposed up to now. Subsequently the free-standing membranes were removed (Fig. 4.2c) and attached (Fig. 4.2d) on the transparent conductive substrates employing a binding medium. In order to investigate the effect of the adhesion layer two different materials were employed: a  $\text{TiO}_2$  sol produced in the CSHR@PoliTo laboratories or a  $\text{TiO}_2$  nanoparticles commercial paste, previously casted on the FTO surface.

Depending on the adhesion material employed the experimental steps to obtain a good interface between NTs and FTO surface are different.

In the case of  $\text{TiO}_2$  nanoparticles commercial paste (Ti-Nanoxide D37, Solaronix), it was deposited on FTO by tape casting technique and the NT membrane was transferred on it and dried at 50 °C for 30 min on a hot plate.

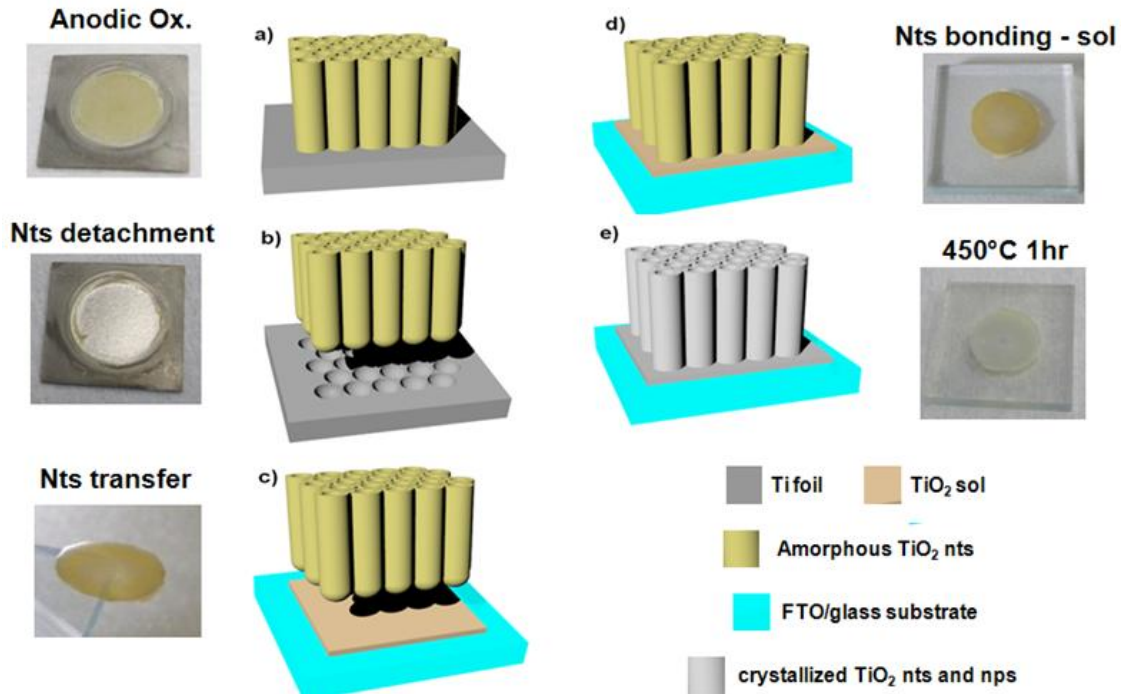


**Fig. 4.2** Schematic of the fabrication process flow of transparent photoanode employing  $\text{TiO}_2$  NT array

When using the sol-gel approach, instead, a 10  $\mu\text{l}$  drop of  $\text{TiO}_2$  sol was casted on FTO cleaned surface and the NTs membrane was transferred on it. Afterwards, samples were left at room temperature overnight.

Finally (Fig. 6e), a thermal treatment at 450  $^{\circ}\text{C}$  for 1 h is performed for all the samples in order to crystallize both the nanotube array and the binding film of  $\text{TiO}_2$  nanoparticles.

#### 4.3.1.1.1 Nanotubes array bonding on transparent substrate

A FESEM micrograph of the multilayered structure is shown in Figure 4.3a showing the  $\text{TiO}_2$  nanoparticles commercial paste as adhesion layer (with a mean thickness of 4  $\mu\text{m}$ ). In Figure 4.3b, a higher magnification of the NTs/NPs interface confirms the good adhesion between the two layers. This process for membrane bonding is easier than others previously reported [9-10] since just one thermal step is required for membrane crystallization, for  $\text{TiO}_2$  NP interconnection and for NPs/NTs interface formation.

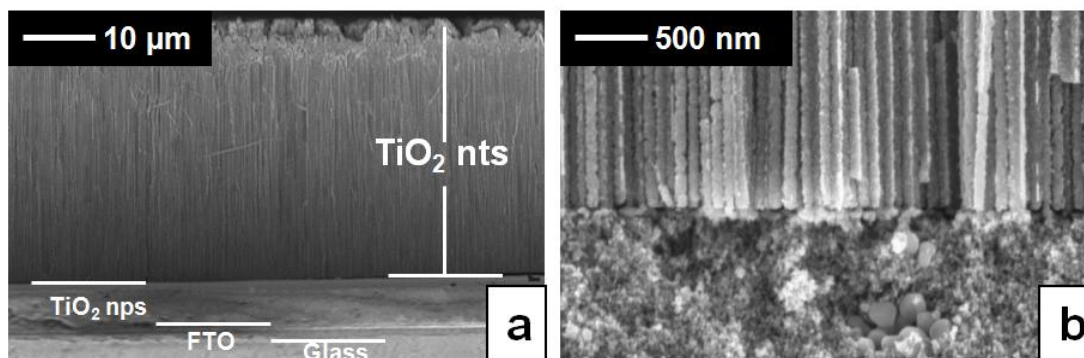


**Figure 4.3** FESEM micrographs showing the cross section of the crystallized NT array: the multilayered structure (a) and an higher magnification (b) of the  $\text{TiO}_2$  NTs/NPs interface.

Following the same detachment procedure described in 4.3.1.1 NTs membrane were transferred on FTO/glass substrate and a drop of  $\text{TiO}_2$  nanoparticle solution, previously casted on the FTO surface, was used as binding medium. At last, thermal treatment is performed to crystallize both the nanotube array and the binding film of  $\text{TiO}_2$  nanoparticles with crystals of about 15 nm, as measured by FESEM analysis. Fig. 4.4 shows a FESEM micrograph of the final multilayer structure consisting of glass / FTO /  $\text{TiO}_2$ -np /  $\text{TiO}_2$ -nt layers.

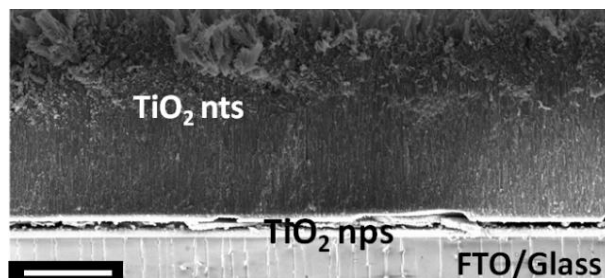


**Fig. 4.4** Cross-sectional view of the multilayer structure consisting of glass / FTO /  $\text{TiO}_2$ -np /  $\text{TiO}_2$ -nt layers (scale bar 10  $\mu\text{m}$ ).

#### 4.3.1.1.2 *TiO<sub>2</sub> nanotubes/nanoparticles composite*

TiO<sub>2</sub> NT/NP composite photoanodes were fabricated including different NT content into the NP network. The NPs expose large surface areas for the dye anchoring, while the incorporated nanotubes can improve the electron lifetime (acting as shortcuts for electron transport at the electrode as depict in figure 4.5a-b) and scatter the incident photons thus enhancing the light harvesting. After mixture into nanoparticle paste, NTs are completely included into the particle network as shown in figure 4.5d.

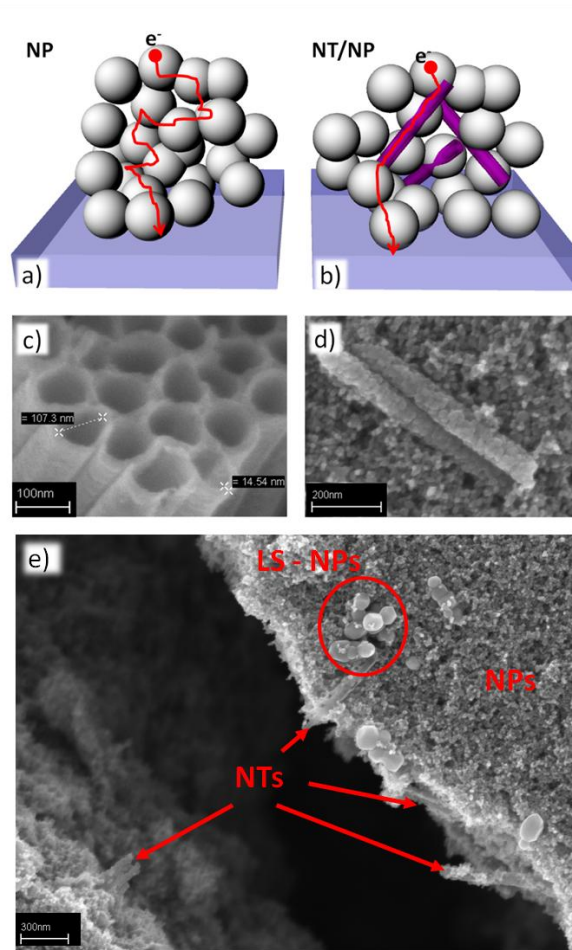


**Fig. 4.5** 3D representation of electrons pathway in NP (a) and NT/NP (b) composite electrodes; FESEM micrographs showing (c) the as-grown TiO<sub>2</sub> NTs and (d, e) the TiO<sub>2</sub> NTs (5 wt%) mixed with the NP paste at different magnifications.

Figure 4.5e shows a lower magnification of a deep fissure transversely the NT/NP composite film in which it is possible to distinguish the two components of the porous layer (NPs and LS-NPs) and the presence of NTs included into the network.

The  $\text{TiO}_2$  NTs were broken in shorter tubes during grinding and mixing of the powder into the paste, with length ranging from 500nm up to 2  $\mu\text{m}$  (see figure 4.5d-e). These NTs incorporated in the NPs network could act as scattering centers for the incoming light and consequently contribute to increase the light harvesting and the optical path in the film [11,12].

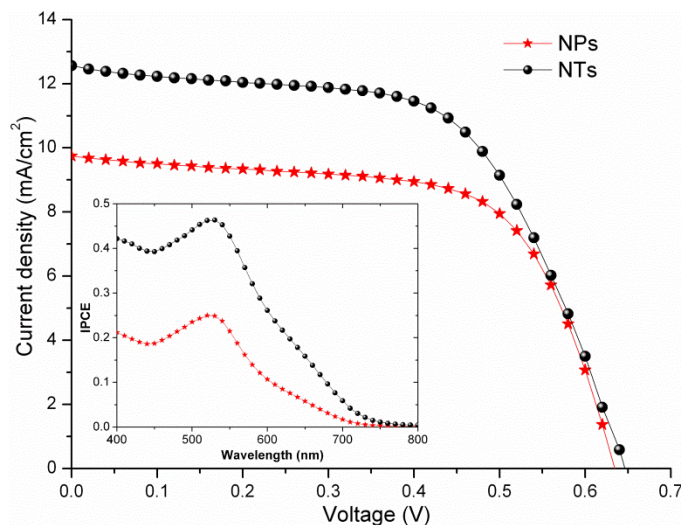
$\text{TiO}_2$  NT/NP composite films were fabricated squeezing the paste on FTO substrates in order to obtain an 8  $\mu\text{m}$  thick layer (measured by a profilometer). XRD analysis of the samples after annealing show diffraction spectra in perfect agreement with the reference patterns for anatase  $\text{TiO}_2$  (JCPDS 89-4921, result not shown here).

### 4.3.2 Evaluation of photovoltaic parameters

#### 4.3.2.1 NTs bonding using commercial $\text{TiO}_2$ paste

The drawback of this approach lies in the limitation in the choice of the membrane thickness for transparent DSC electrode fabrication. NT membrane thinner than 25  $\mu\text{m}$  were observed to dash in many pieces after the single thermal treatment due to the stress releasing across the entire NT array. On the other hand, if the length of the tubes is increased above a certain limit, the dye molecules nearest to  $\text{TiO}_2$  NT bottom adsorb a consistent part of the incident light resulting in a reduced carrier generation in the outer part of the tube and an increase of the recombination rate (the so-called filtering effect) [13]. For the above reasons a 40  $\mu\text{m}$  thick  $\text{TiO}_2$  NT membrane was chosen as the optimal value in order to avoid fractures and to maximize the dye loading without incurring in the filtering effect.

The NT-based photovoltaic cells were assembled employing the microfluidic architecture and fully characterized, and their performances have been compared to those of NP-based DSCs. In Figure 4.6 the current density vs. voltage curves measured for the two kinds of cells are reported. In Table 1 are summarized the measured photovoltaic parameters and the evaluated overall conversion efficiency (see Eq. 4 in 2.1.3.1). The cells fabricated with NTs exhibit higher light conversion efficiency due to a higher current density with respect to the NP-based ones.

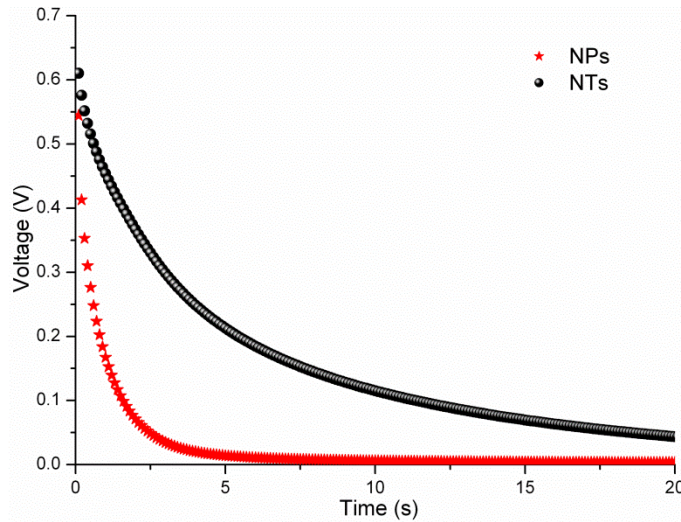


**Figure 4.6** Current density-voltage curves of  $\text{TiO}_2$  NP and  $\text{TiO}_2$  NT-based DSCs. Related IPCE spectra are shown in the inset.

**Table 1.** Photovoltaic parameters of TiO<sub>2</sub> NP and TiO<sub>2</sub> NT-based DSCs.

<i>Cell</i>	<i>J<sub>SC</sub> (mA/cm<sup>2</sup>)</i>	<i>V<sub>OC</sub> (V)</i>	<i>FF</i>	<i>PCE (%)</i>
NPs	9.75	0.634	0.65	3.99
NTs	12.56	0.646	0.59	4.82

The increase of the  $J_{SC}$  values is also noticeable in the IPCE spectra, shown in the inset of Figure 4.4 and can be ascribed to a most efficient charge collection in the NT-based photoanode. In fact, in the NP-based DSC the electron transport pathways result longer and intricate due to the random orientation and assembly of nanoparticle network, leading to retarded electron collection by the FTO substrate. On the contrary the 1-dimensional NT structure favors the electron transport, resulting in an improvement of the collection efficiency. Moreover the reduced number of defects (such as grain boundaries) of the NT array with respect to the NP layer is also responsible for a decrease of the recombination rate. This result is confirmed by the OCVD measurements performed on the cells reported in Figure 4.7. A slower decay of the photovoltage (meaning a higher charge lifetime, see Eq. 7 in 2.1.3.3 ) can be clearly observed for the NT-based cell with respect to the NP-based one: the former, with its lower number of trap-sites exhibits slower recombination kinetics.

**Figure 4.5** Open circuit voltage decay curves of TiO<sub>2</sub> NP and TiO<sub>2</sub> NT-based DSCs.

A further confirmation of the reduced recombination in NTs-based devices came from the EIS analysis. As shown in Figure 4.8a, the peak related to the photoanode contribution is significantly shifted towards lower frequencies for the NT-DSC with respect to the NP-based cell. In the latter, the oxide characteristic frequency  $f_{ph}$  moves towards higher frequency, with a partial overlap with the peak related to the counter electrode. Since the  $f_{ph}$  value is inversely proportional to the electron lifetime, it is clear that the NT-based DSC exhibits a superior performance in terms of charge recombination. Exploiting the EIS analysis it is also possible to evaluate the transport properties of the two photoanodes and to relate them to the charge

collection efficiency, responsible for the higher photocurrent observed in NT-based DSC. Using Eqs. 9-10 (see 2.1.3.4), the electron lifetime and diffusion coefficient values were calculated, and the results of this analysis are reported in Figure 4.8b as a function of the chemical capacitance  $C_\mu$ . The evaluated charge lifetimes of the nanotubes array are one order of magnitude higher with respect to those related to the nanoparticles, thus confirming the reduced recombination rate thanks to the low-dimensional nature of NTs. Moreover the direct pathway for the electrons in the nanotubes leads to an increase of the diffusion coefficient values. As a direct consequence, the diffusion length at cell open circuit voltage, evaluated using Eq.11 (see 2.1.3.4), was found to be 86  $\mu\text{m}$  and 13  $\mu\text{m}$  for the NT and NP-based DSC, respectively. The obtained value for the diffusion length of NT-based cell is in perfect agreement with other results already reported in literature [14].

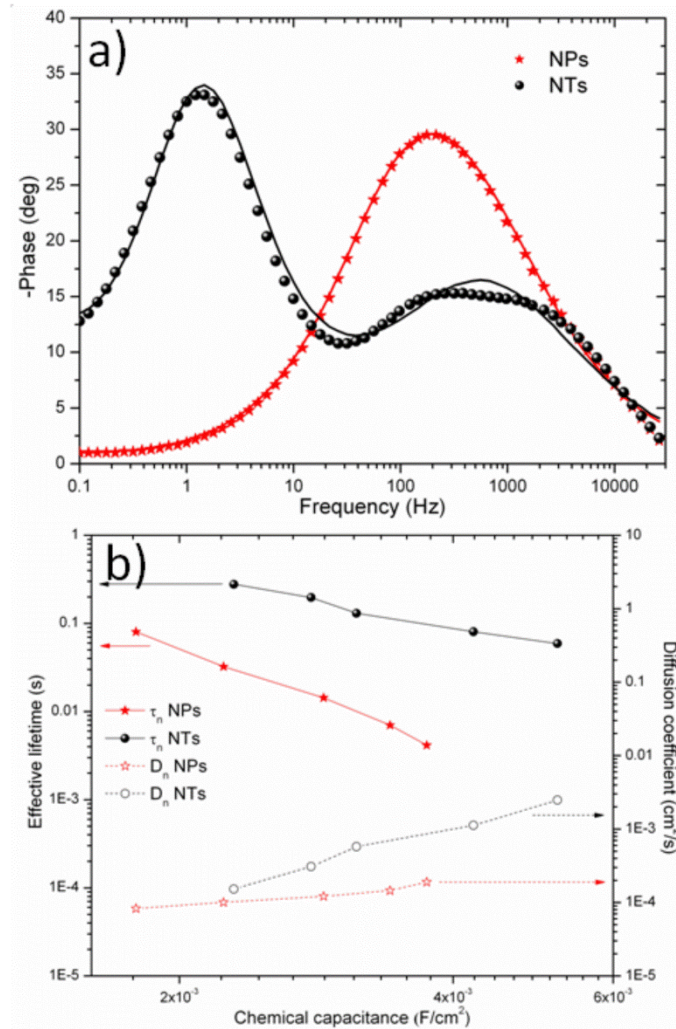


**Figure 4.8** (a) Bode representation of phase impedance measured for  $\text{TiO}_2$  NP and  $\text{TiO}_2$  NT-based DSC at open circuit voltage; the point are experimental data and the continuous lines are fitting curves. (b) Dependence of the calculated electron lifetime and diffusion coefficient in function of voltage for  $\text{TiO}_2$  NP and  $\text{TiO}_2$  NT-based DSC.

#### 4.3.2.2 Nanotube bonding using homemade $\text{TiO}_2$ sol

The employing of  $\text{TiO}_2$  sol instead of commercial paste allow to overcome the thickness limitation described above mainly thanks to the reduced stress releasing of the binding material during the thermal treatment. We compared the results obtained for the three different nanotube lengths (12, 22 and 30  $\mu\text{m}$ ). With the purpose of increase the performance of this electrode the influence of the  $\text{TiCl}_4$  treatment was investigated.

In Fig. 4.9 the results of I-V measurements, performed on the cells fabricated using the NT array membranes employing the microfluidic architecture, are reported. The photovoltaic parameters are summarized in Table 2. Looking at these values, it can be noticed an increase of the photocurrent density while increasing the nanotube thickness (from 10.07 to 14.77  $\text{mA}/\text{cm}^2$  passing from 12 to 30  $\mu\text{m}$ ). This improvement has to be attributed to the increase of the total surface available for the dye anchoring. Moreover the  $\text{TiCl}_4$  treatment led to a further improvement of the photovoltaic performances for all the samples under study. In fact, a downward shift of the  $\text{TiO}_2$  conduction band occurs due to the effect of this treatment [15], so an enhancement of the electron injection efficiency is obtained; moreover a higher number of charge separation interfaces is originated, leading to an intensified light absorption [16]. The overall effect is an increase of the  $J_{\text{SC}}$  values, and consequently of the photoconversion efficiency. A maximum value for the PCE equal to 7.56% has been obtained for the cell fabricated with 30  $\mu\text{m}$  thick nanotube membrane treated with  $\text{TiCl}_4$ .

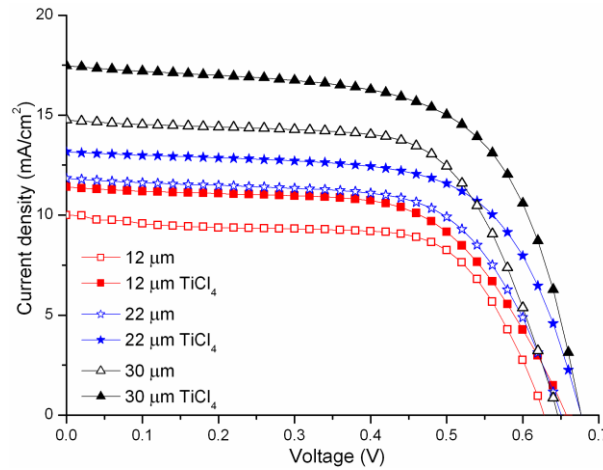


**Fig. 4.9** Current density-voltage curves of  $\text{TiO}_2$  NTs-based DSCs with and without  $\text{TiCl}_4$  treatment for different nanotube lengths.

**Table 2** Photovoltaic parameters of  $\text{TiO}_2$  NTs-based DSCs with and without  $\text{TiCl}_4$  treatment for different nanotube lengths.

Cell	$J_{\text{sc}}$ ( $\text{mA}/\text{cm}^2$ )	$V_{\text{oc}}$ (V)	FF	PCE (%)
12 $\mu\text{m}$	10.07	0.628	0.66	3.64
12 $\mu\text{m}$ $\text{TiCl}_4$	11.41	0.657	0.62	4.65
22 $\mu\text{m}$	11.84	0.651	0.64	4.97
22 $\mu\text{m}$ $\text{TiCl}_4$	13.17	0.677	0.65	5.82
30 $\mu\text{m}$	14.77	0.646	0.66	6.26
30 $\mu\text{m}$ $\text{TiCl}_4$	17.47	0.677	0.64	7.56

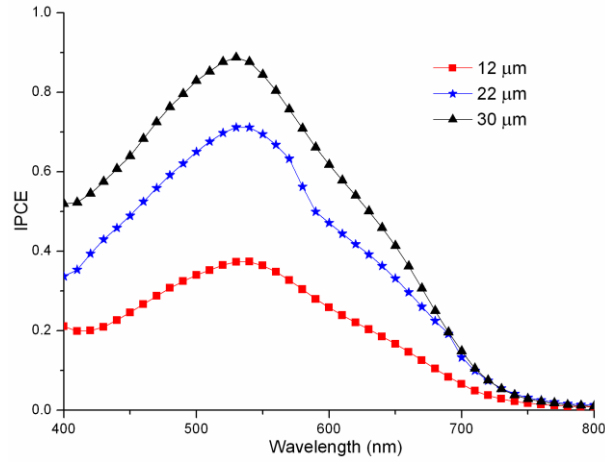


**Fig. 4.10** Incident photon-to-electron conversion efficiency spectra of  $\text{TiCl}_4$ -treated nts-based DSCs for different nanotube lengths.

The observed increase of short-circuit current density with the increased nanotube length was also confirmed by IPCE measurements, reported in Fig 4.10 for the  $\text{TiCl}_4$ -treated cells. The spectra show an upward shift in the wavelength range from 400 to 750 nm, with a maximum IPCE value of 0.89 measured at 530 nm for 30  $\mu\text{m}$  length nanotubes.

The effect of the NT length on the recombination kinetics in the fabricated devices was studied through open circuit voltage decay measurements and the results are reported in Fig.4.11. No difference in the exponential decay was observed for the different NT membrane thickness, meaning that the electron lifetime is not dependent on nanotube length. A slower decay of the photovoltage (meaning an increase of the charge lifetime) was instead observed for the  $\text{TiCl}_4$ -treated cells (as shown in the inset of Fig. 4.11): this is an evidence of a reduced recombination rate due to the nanoparticle coverage on the nanotube walls that acts as barrier for the interfacial recombination[15,17].

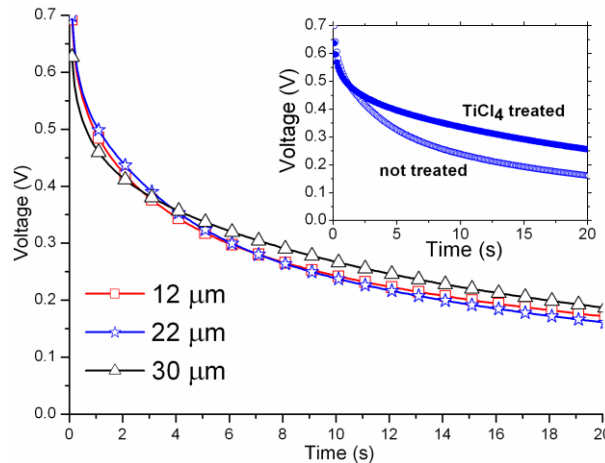


**Fig. 4.11** Open circuit voltage decay curves of not-treated nts-based DSCs for different nanotube lengths. In the inset the comparison between the cells fabricated with 22  $\mu\text{m}$  thick nt membranes with and without  $\text{TiCl}_4$  treatment is reported.

In fact, as suggested by O'Regan and co-workers [18], the NPs could occupy nanotube surface impurities, defects and ground boundaries (that are the sites on which the recombination processes mainly occur).

In order to study in detail the recombination and transport properties of the NT membranes, electrochemical impedance spectroscopy analysis was performed. From the equivalent circuit fitting of the experimental curves, the effective electron lifetime  $\tau_n$  and the diffusion length  $L_n$  values in the oxide were extracted and the results are reported in Fig. 4.12. The same parameters have been evaluated for a cell fabricated with a 8  $\mu\text{m}$ - thick  $\text{TiCl}_4$ -treated layer of  $\text{TiO}_2$  NPs (also shown in Fig.4.12). As already observed from the OCVD measurements, it is evident an increase of the carrier lifetime in the NTs-based DSCs due to the  $\text{TiCl}_4$  treatment, while comparable values were obtained for the diffusion length, meaning that the charge transport properties of the NTs are adequate for electron collection even without the treatment [15].

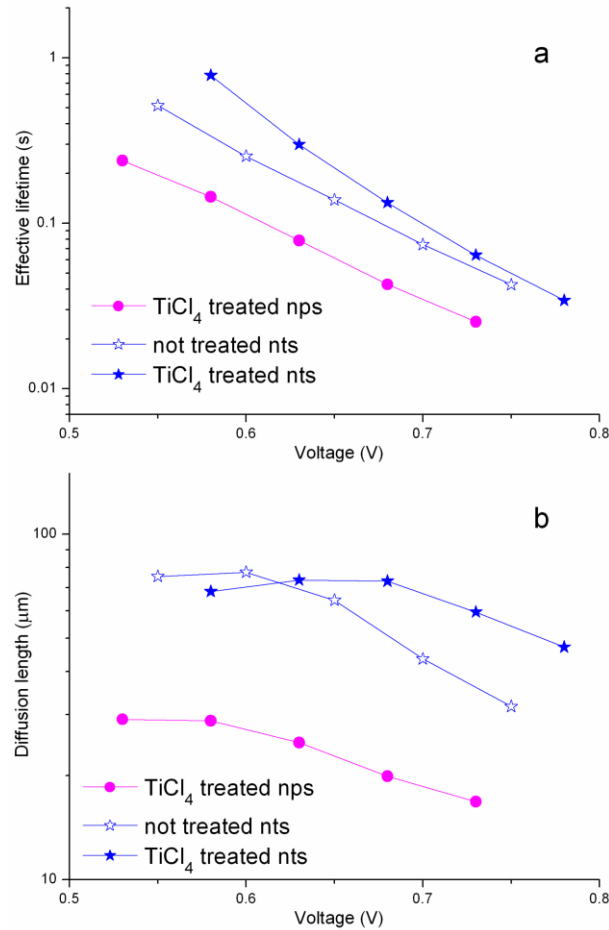


**Fig. 4.12** (a) Effective electron lifetime and (b) diffusion length dependence on the bias voltage for the cells fabricated with 22  $\mu\text{m}$  thick nt membranes with and without  $\text{TiCl}_4$  treatment. For comparison, the same parameters extracted for a cell fabricated with 8  $\mu\text{m}$  of  $\text{TiCl}_4$ -treated  $\text{TiO}_2$  nanoparticles are reported.

A significant increase of both electron lifetime and diffusion length values was observed for the NTs-based cells with respect to the NPs-based one. In fact the number of surface states is proportional to specific area and the NT surface is a order of magnitude lower with respect to the NPs one. For this reason the NT array presents a reduced number of defects and trap sites (such as grain boundaries) with respect to the NP layer, and the charge recombination rate is subsequently greatly reduced [19]. Moreover, thanks to the 1D structure, the charge transport is improved in the NTs-based DSCs, while in the NPs-based ones the transport mechanisms result more complicated due to a longer pathway for the electrons in the nanoparticle network. A slight dependence of the diffusion length on the bias voltage can be observed in Fig. 4.12b. At applied voltage higher than the  $V_{oc}$  in fact the  $L_n$  decreases approaching the thickness of the film. As suggested by Snaith and co-workers [20] this behavior can be ascribed to the reduced collection efficiency occurring under these conditions due to the increased recombination rate. The improved transport properties of the NTs-based cell are also confirmed by the effective diffusivity values  $D_n$ , calculated through the Eq. 10 (see 2.1.3.4). We found, at cells open circuit voltage, the values of  $4 \cdot 10^{-4} \text{ cm}^2/\text{s}$ ,  $3 \cdot 10^{-4} \text{ cm}^2/\text{s}$  and  $0.8 \cdot 10^{-4} \text{ cm}^2/\text{s}$  for the NTs treated cell, NTs untreated cell and NPs cell, respectively.

#### 4.3.2.3 $\text{TiO}_2$ nanotubes/nanoparticles composite

DSCs based on  $\text{TiO}_2$  NT/NP composite photoanodes were fabricated including different NT content (0 wt%, 5 wt% and 10 wt%) into the NP network. The devices were assembled employing the microfluidic architecture and the results of the I-V measurements are reported in figure 4.13: the curves show an increase of the short-circuit current density ( $J_{sc}$ ) for the composite photoanodes with respect to the NP-based one.

The PCE was found to be 5.76% when using 5 wt% of NTs, meaning a 10% enhancement with respect to pure NP electrode.  $V_{oc}$  and FF seem to be almost independent from  $\text{TiO}_2$  NT inclusion into the composite photoanode.

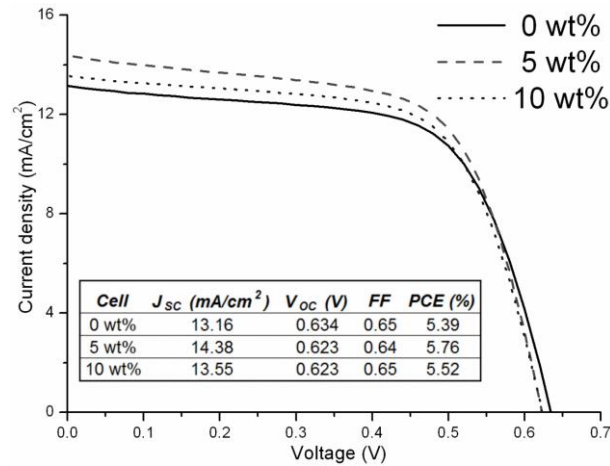


**Fig. 4.13** Current density-voltage curves of DSCs based on  $\text{TiO}_2$  NT/NP composite photoanodes fabricated with different NT content under standard AM1.5G illumination; the photovoltaic parameters are summarized in the table reported in the inset

The increase of the  $J_{SC}$  values is also evident in the IPCE spectra, shown in the figure 4.14: this enhancement could be ascribed to a most efficient charge collection in the NT/NP photoanode [21] and also to light scattering due to the presence of nanotubes [22].

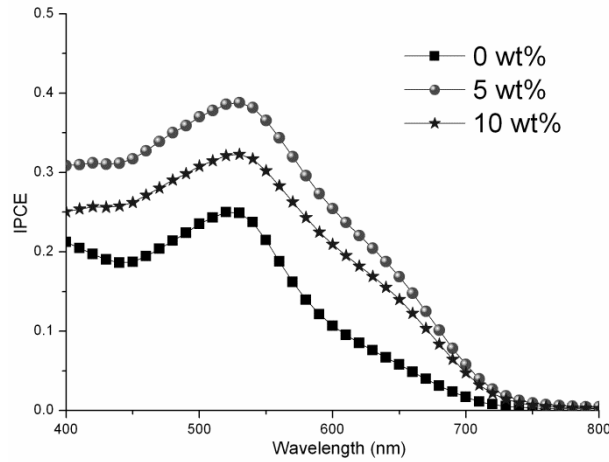


**Fig. 4.14** IPCE spectra of DSCs based on  $\text{TiO}_2$  NT/NP composite photoanodes fabricated with different NT content.

In order to study the recombination mechanism into the composite film, Open Circuit Voltage Decay measurements were carried out. The OCVD curves, reported in figure 4.15, clearly show that the composite photoanode-based DSCs exhibit reduced recombination (slower decay) with respect to the standard NP-based (faster decay).

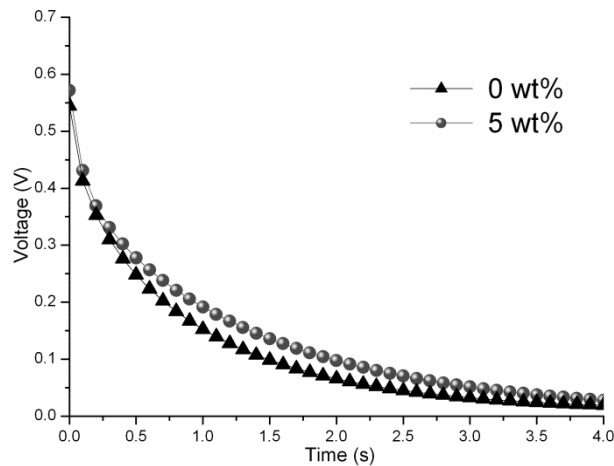


**Fig. 4.15** Open circuit voltage decay curves of the DSCs fabricated with NP-based photoanode (0 wt%) and NT/NP composite photoanode (5 wt%).

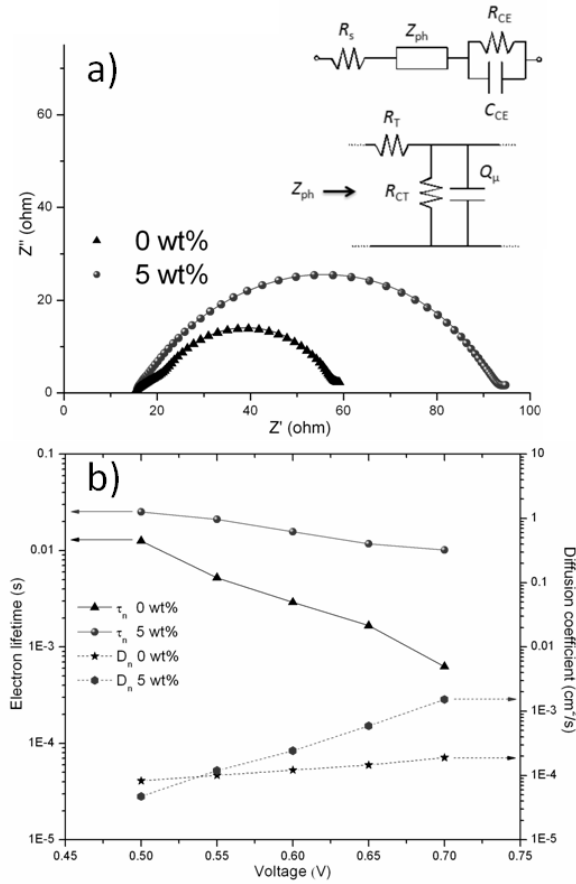


**Fig. 4.16** a) Measured (symbols) and fitted (solid lines) impedance spectra at 0.6V of DSCs fabricated with NP-based photoanode (0 wt%) and NT/NP composite photoanode (5 wt%). The equivalent circuit exploited for the fitting of the curves is reported in the inset. b) Electron lifetime and diffusion coefficient dependence on the bias voltage for the DSCs fabricated with NP-based photoanode (0 wt%) and NT/NP composite photoanode (5 wt%).

In order to quantify the electron lifetime values for the different NT content into the NP network, Electrochemical Impedance Spectroscopy measurements were performed.

In figure 4.16a the EIS curves measured at 0.6V for the two kinds of different cell are reported, together with the results of the fitting. It can be noticed that the second arc, related to recombination mechanisms, is wider and taller for the composite photoanode with respect to the NP-based one, evidencing the lower recombination rate, as already observed by OCVD measurements. From the fitting parameters, using the Eq. 9 (see 2.1.3.4) the electron lifetime values were obtained, and in figure 4.16b they are presented as function of bias voltage. The typical exponential dependence on the applied voltage is evident in the semi-logarithmic plots. An improvement of the charge lifetime was evidenced in the NT/NP composite photoanode: in particular, the lifetime values of the two cells, at 0.6V, were found to be about 16 ms and 3 ms for the composite-based cell and the NP-based cell, respectively. Moreover the former cell exhibits higher diffusion coefficient values, meaning increased transport properties, which are

responsible for the enhancement of the collection efficiency already observed in the IPCE spectra. These results demonstrate the reduced recombination rate and the improved charge transport properties related to the insertion of NTs into the NP network, as already observed in other works [23,24].

#### 4.4 Sponge-like ZnO based photoanodes

ZnO films were obtained as described in chapter 3 (3.3.1). Briefly, the substrates were cleaned, placed in a RF magnetron sputtering system pumped down to a pressure in the range of  $4.3 \times 10^{-5}$  and  $5.3 \times 10^{-5}$  Pa. The Ar plasma was created (Ar flow of 10 sccm at a pressure of 0.67 Pa) by applying an RF power of 100 W at 13.56 MHz between the two sputtering electrodes. Deposition times ranging between 2 – 10 hours allow to obtain films with a thickness from 5 up to 18 .

After the fabrication, photoelectrodes were heated at 70 °C and soaked into a 0.25 mM N719 ethanol-based sensitizing solution (Ruthenizer535bis-TBA, Solaronix) for different times (10 min, 20 min, 30 min, 1 h, 2 h, 5 h and 24 h) at room temperature and then rinsed in pure ethanol to remove the un-adsorbed dye molecules.

##### 4.4.1 Evaluation of photovoltaic behavior

Here are reported all the results obtained integrating Sponge-like ZnO nanostructures as photoanodes into DSCs.

In order to investigate the coral-shaped ZnO photovoltaic performances, different dye immersion times, different pH of the dye solution and different film thicknesses have been tested. The experimental parameters, the representative results of the electrical characterizations and the evaluated photoconversion efficiencies are summarized in Tab.3.

**Table 3** Characteristics of the fabricated ZnO-based DSSCs and results of photovoltaic characterization.

<i>Sample</i>	<i>ZnO thickness (<math>\mu\text{m}</math>)</i>	<i>Dye impregnation time</i>	<i>Solution pH</i>	<i><math>J_{sc}</math> (<math>\text{mA}/\text{cm}^2</math>)</i>	<i><math>V_{oc}</math> (V)</i>	<i>FF</i>	<i><math>\eta</math> (%)</i>	<i><math>R_2</math> (<math>\Omega</math>)</i>
A	5	10 minutes	6.5	6.81	0.59	0.58	2.47	52.43
B	5	30 minutes	6.5	7.75	0.60	0.58	2.84	45.39
C	5	1 hour	6.5	8.23	0.62	0.58	2.99	38.43
D	5	2 hours	6.5	8.95	0.62	0.57	3.09	27.80
E	5	5 hours	6.5	7.45	0.62	0.52	2.50	47.83
F	5	24 hours	6.5	5.87	0.67	0.48	1.90	92.20
G	5	24 hours	9.0	7.66	0.58	0.58	2.56	44.02
H	8	2 hours	6.5	11.12	0.61	0.53	3.59	19.42
I	8	5 hours	6.5	9.08	0.62	0.53	2.98	40.92
J	12.5	2 hours	6.5	13.44	0.60	0.54	4.58	10.33
L	15	2 hours	6.5	14.37	0.566	0.59	4.83	6.51
M	18	2 hours	6.5	15.26	0.582	0.59	5.25	3.22

#### 4.4.1.1 Immersion time

In Fig.4.17, the experimental curves for current density versus voltage analysis and impedance spectroscopy characterization for cells with 5  $\mu\text{m}$  thick ZnO photoanodes subjected to different immersion times in N719 solution (ranging between 10 min and 24 h, samples A-F) are reported.

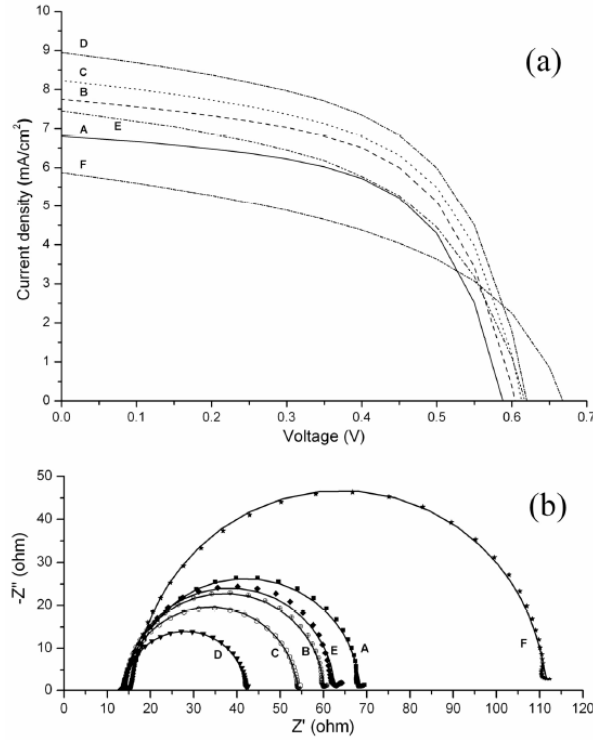


**Figure 4.17.** Current density-voltage curves (a) and impedance spectra (b) of ZnO-based DSSCs for different impregnation times in dye solution (samples A-F, see Table 1). In (b) the points are experimental data while the continuous lines are fitting curves.

The photovoltaic conversion efficiency values, evaluated from I-V curves, are reported in Fig.4.18 as a function of the incubation time in dye solution. It emerges a non-monotonic behavior, with a most favorable sensitization time of 2 hours. This trend has also been confirmed by efficiency measurements performed on a different set of solar cells fabricated with impregnation times in the range 2-5 hours.

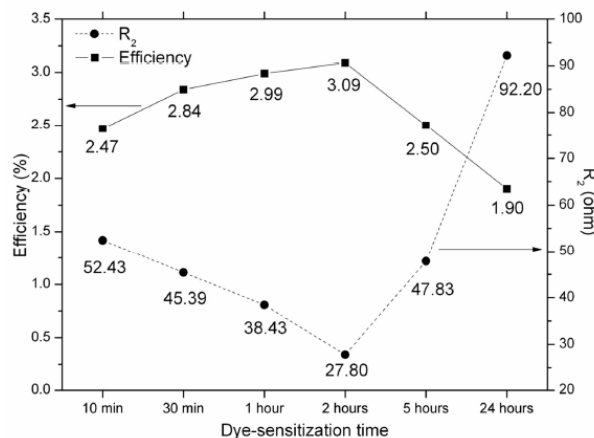


**Figure 4.18.** Efficiency behavior of 5  $\mu\text{m}$  ZnO-based DSSCs with different impregnation time in dye solution. The corresponding oxide-electrolyte interfacial resistance  $R_2$  obtained by fitting the impedance spectra are also shown.

The lowering of cell efficiency during prolonged treatments is due to a progressive degradation of ZnO surface. In fact, the modeling of EIS spectra evidences an initial decrease of the charge-transfer resistance  $R_2$  related to electron recombination (central arc of the impedance spectra), as emphasized in Fig.4.18. For immersion times longer than the optimal value, the recombination processes related to the interface between the un-sensitized zones of the oxides and the electrolyte gain importance. The initial rise in efficiency for short incubation times is related to the slow kinetic of dye adsorption on the semiconductor surface. For low coverage of ZnO surface with dye molecules, the efficiency is reduced both because the number of photo-generated carriers is lower and because the recombination between the un-sensitized ZnO and the electrolyte is higher. The unoccupied dye-absent sites on semiconductor surface are supposed to increase the rate of interfacial electron transfer (recombination) from the conduction band of ZnO to  $\text{I}_3^-$ . The decrease in efficiency when the optimal incubation time is exceeded can be related to the formation of molecular aggregates between dye molecules and dissolved  $\text{Zn}^{2+}$  ions originating from the ZnO surface. The aggregates give rise to a filtering effect (inactive dye molecules), as previously reported by Keis et al. [25]. In particular, three mechanisms are involved: adsorption of dye, dissolution of Zn surface ions and formation of aggregates in the pores of the film.

In order to better analyze the  $\text{Zn}^{2+}$ -dye aggregates formation, optical absorbance measurement in the UV-visible range were performed on the sensitized ZnO photoanodes for different soaking times. The resulting spectra are reported in Fig.4.19. The typical N719 adsorption peaks (located at 400 and 535 nm) clearly increase while increasing the impregnation time from 10 min to 5 hours, as confirmed visually by the color of the film, which becomes more intense for longer dipping. After 24 hours of incubation, the behavior of the absorbance curve drastically changes: the overall increase in absorbance evidences a higher content of dye molecules, but the shift of the peak at 400 nm and the arising of new peaks (as shoulders of the peak centered at 535 nm) indicate the formation of new aggregates. Such molecular complexes show strong adsorption properties but are unable to inject electrons in the conduction band of the semiconductor, as confirmed by IPCE spectra reported in Fig.4.20. In fact, the curve related to 24 hours of incubation time shows the lowest values of photo-conversion, while the 2 hour-cell shows the best performance.

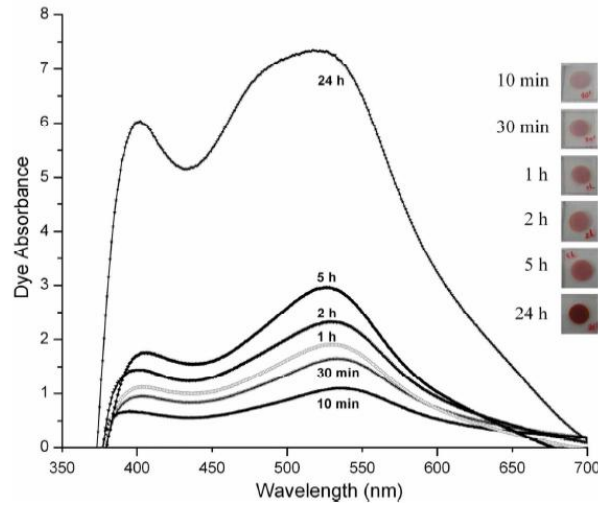


**Figure 4.19** UV-visible absorbance curves obtained for the N719 dye on the ZnO photoanodes (visualized in the insert), for different incubation times in dye solution.

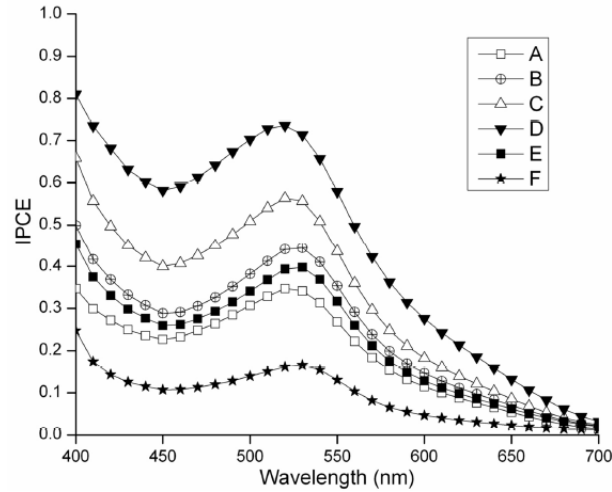


**Figure 4.20** IPCE curves of 5 μm ZnO-based DSSCs for different impregnation time in dye solution.

#### 4.4.1.2 Effect of PH

Since the long term formation of  $\text{Zn}^{2+}$ /dye aggregates is partially suppressed when a more basic dye solution is used [25], the effect of pH of the sensitizing mixture was experimentally evaluated adding 0.3 mM sodium hydroxide to the N719 solution. The pH was thus modified from 6.5 (normal solution) to 9 (hydroxide-containing solution) and the photovoltaic parameters are summarized in table 3. The 5 μm ZnO sample incubated on the basic solution for 24 hours showed an overall efficiency of 2.56%, significantly higher than the corresponding value (1.90%) obtained with a dipping in the slightly acid solution for the same time (see Tab.3). The deprotonation of the solution reduces the kinetics of  $\text{Zn}^{2+}$  ion release, allowing longer sensitization suppressing the formation of aggregates.

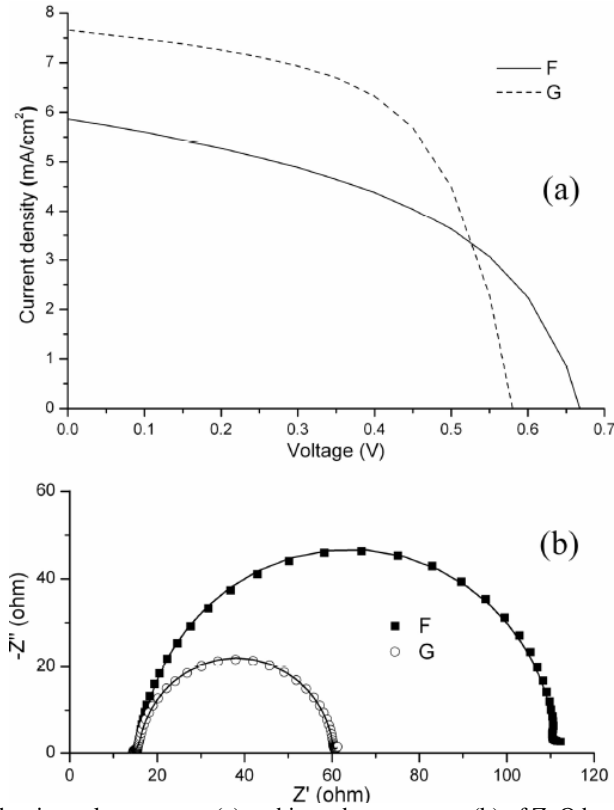


**Figure 4.21** Current density-voltage curves (a) and impedance spectra (b) of ZnO based DSSCs varying dye solution pH for 24 h immersion time (samples F and G, see Table 1). In (b) the points are experimental data while the continuous lines are fitting curves.

The degradation mechanism of the ZnO layer brings to an increase of the charge recombination process, and this effect is reduced while sensitizing the photoelectrode in the basic solution. This feature is evident by comparing samples F and G, as shown in I-V and EIS spectra in Fig.4.21. The charge-transfer resistance ( $92.2 \Omega$ ) of the sample F subjected to a 24 hours incubation in normal (slightly acid) solution is almost two times higher with respect to the shortly-incubated cells, and is sensibly reduced for sample G ( $44 \Omega$ ) after the same long incubation in the basic mixture. Thus, for an efficient long dye-sensitization process of ZnO electrodes, dyes with no acidic protons are preferred in order to suppress the dissolution of Zn surface ions and formation of  $\text{Zn}^{2+}$ /dye aggregates. Our experimental evidences are in agreement with the arguments proposed by Keis and co-workers [26]. For shorter incubation times, the same beneficial effect is not evidenced, since the de-aggregation effect conflicts with the dye desorption, that usually occurs in basic environment.

#### 4.4.1.3 ZnO thickness

With the aim of exposing higher surface area to dye absorption in order to further increase the conversion efficiency, the ZnO thickness was varied from 5 to 18  $\mu\text{m}$ , by means of appropriate choice of the sputtering deposition time. In the thicker films an increase of the photogenerated charges injected in the conduction band of the oxide and a decrease of recombination processes,

due to a lower number of trap sites (lower number of sites unoccupied by dye molecules) are clearly observable (Fig.4.22). Using film of 12.5  $\mu\text{m}$  and the optimal incubation time of 2 hours, a solar energy conversion efficiency of 4.58% was obtained.

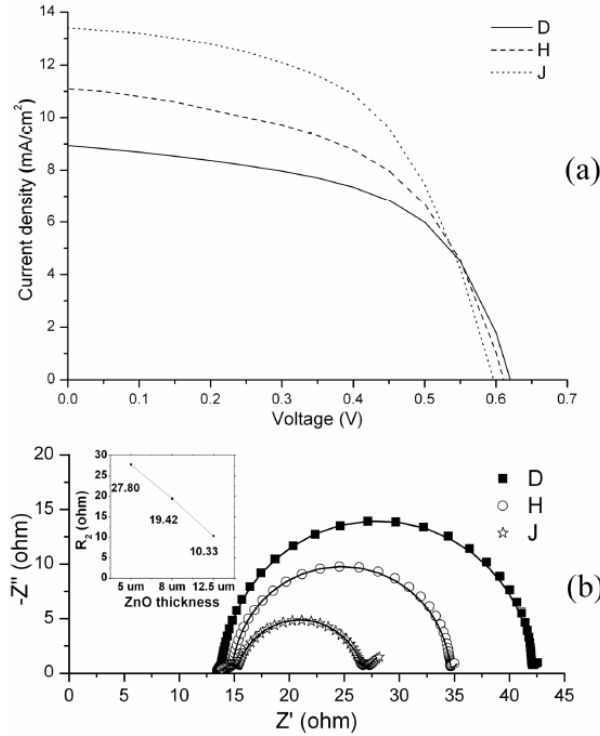


**Figure 4.22** Current density-voltage curves (a) and impedance spectra (b) of ZnO based DSSCs for different film thicknesses with 2 h immersion time in dye solution (samples D, H and J, see Table 1). In (b) the points are experimental data while the continuous lines are fitting curves. In (b) the insert shows the decreasing of the oxide-electrolyte interfacial resistance  $R_2$  while increasing ZnO thickness.

Photoanodes with a ZnO film with a thickness equal to 15  $\mu\text{m}$  were fabricated and several devices were tested and the relative error between different samples was within the 5%, meaning a very high reproducibility. An incubation time of two hours was found to be optimal for the sensitization also at higher thickness. In particular, an evident increase in  $J_{sc}$  is noticed, while  $FF$  is almost independent from the sensitization procedure.

With the optimized sensitization time of two hours, the photovoltaic behavior of the device as a function of the ZnO film thickness was tested. The results of the I-V characterization and the Bode representation of the EIS phase are reported in Fig.4.23. The increase in photoanode thickness from 12.5  $\mu\text{m}$  to 18  $\mu\text{m}$  in the microfluidic architecture allowed obtaining a higher efficiency, with an increase on the short circuit current. 18  $\mu\text{m}$  thick ZnO film allow to reach a maximum power conversion efficiency of 5.25 %.

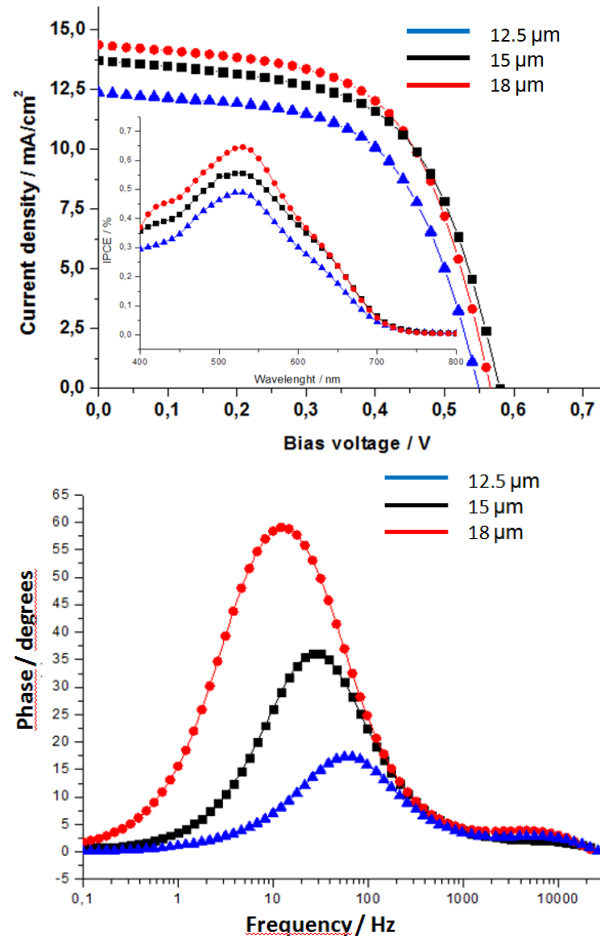


**Fig. 4.23** I-V and EIS (Bode plot, inset) characterization of ZnO-based DSCs fabricated with different photoanode thicknesses, 12.5  $\mu\text{m}$  (black) and 15  $\mu\text{m}$  (red). The sensitization time was 2 hrs.

All the photovoltaic parameters are summarized in Table 3. Thicker photoelectrodes are able to load a higher amount of dye, thus allowing the injection of a higher number of carriers in the conduction band of the semiconductor, and the charge transport is efficient enough to allow the collection of the electrons at the FTO electrode. More interestingly, the carrier lifetime show a dependence on the photoanode thickness. The experimental curves of EIS were fitted using an equivalent circuit in order to obtain information about transport and recombination of charges [27]. In particular, the electron lifetimes at open circuit voltage can be estimated from the frequency  $f$  giving the maximum in the Bode plot reported in Fig.4.23(b), as  $\tau=1/(2\pi f)$ . The evaluated charge carrier lifetimes at  $V_{oc}$  were equal to 12 ms and 40 ms for the 12.5  $\mu\text{m}$  and 15  $\mu\text{m}$  thick ZnO photoanodes, respectively, and reached 55ms for the 18  $\mu\text{m}$  thick ZnO. The dependence of electron lifetime on the photoanode thickness is probably related with the contribution of the back transfer of electrons at the FTO-electrolyte interface [28]. For thicker photoanodes, this parasitic effect loose importance, giving as a macroscopic result a higher overall carrier lifetime, as reported previously for mesoporous  $\text{TiO}_2$  films [29].

## 4.5 References

- [1] S. Ito, T. N. Murakami, P. Comte et al. *Thin Solid Films* 516 (2008) 4613.
- [2] M. K. Nazeeruddin, E. Baranoff, M. Grätzel. *Solar Energy* 85 (2011) 1172.
- [3] A. Lamberti, A. Sacco, S. Bianco, E. Giuri, M. Quaglio, A. Chiodoni, E. Tresso, *Microelectron. Eng.* 88 (2011) 2308.
- [4] M. Paulose, K. Shankar, O.K. Varghese, G.K. Mor, C.A. Grimes. *J. Phys. D: Appl. Phys.* 39 (2006) 2498.
- [5] H.Y. Hwang, A.A. Prabu, D.Y. Kim, K.J. Kim. *Solar Energy* 85 (2011) 1551.
- [6] S. P. Albu, A. Ghicov, S. Aldabergenova, P. Drechsel, D. LeClere, G. E. Thompson, J. M. Macak, P. Schmuki. *Adv. Mater.* 20 (2008) 4135
- [7] G. Liu, K. Wang, N. Hoivik, H. Jakobsen. *Sol. Energ. Mat. Sol. C.* 98 (2012) 24.
- [8] N. Venkatachalam, M. Palanichamy, V. Murugesan. *Mater. Chem. Phys.* 104 (2007) 454.
- [9] M. Dubey, M. Shrestha, Y. Zhong, D. Galipeau, H. He. *Nanotechnology* 22 (2011) 285201.
- [10] Q.W. Chen, D.S. Xu. *J. Phys. Chem. C* 113 (2009) 6310.
- [11] P. Wang, S. M. Zakeeruddin, J. E. Moser, M. K. Nazeeruddin, T. Sekiguchi, M. Grätzel. *Nat. Mater.* 2 (2003) 402.
- [12] Z.S. Wang, H. Kawauchi, T. Kashima, H. Arakawa. *Coord. Chem. Rev.* 248 (2004) 1381.
- [13] S. Ito, S.M. Zakeeruddin, R. Humphry-Baker, P. Liska, R. Charvet, P. Comte, M.K. Nazeeruddin, P. Péchy, M. Takata, H. Miura, S. Uchida, M. Grätzel. *Adv. Mater.* 18 (2006) 1202.
- [14] P. Roy, S. Berger, P. Schmuki, *Angew. Chem. Int. Ed.* 50 (2011) 2904.
- [15] P. M. Sommeling, B. C. O'Regan, R. R. Haswell, H. J. P. Smit, N. J. Bakker, J. J. T. Smits, J. M. Kroon, J. A. M. van Roosmalen. *J. Phys. Chem. B* 110 (2006) 19191.
- [16] J. Yan, F. Zhou, *J. Mater. Chem.* 21 (2011) 9406.
- [17] C.T. Yip, C.S. Mak, A.B. Djurišić, Y.F. Hsu, W.K. Chan. *Appl. Phys. A*, 92 (2008) 589.
- [18] B. O'Regan, J. R. Durrant, P. M. Sommeling, N. J. Bakker, *J. Phys. Chem. C* 111 (2007) 14001
- [19] H. Wang, M. Liu, M. Zhang, P. Wang, H. Miura, Y. Cheng, J. Bell, *Phys. Chem. Chem. Phys.* 13 (2011) 17359.
- [20] H.J. Snaith, R. Humphry-Baker, P. Chen, I. Cesar, S.M. Zakeeruddin, M. Grätzel, *Nanotechnology* 19 (2008) 424003.
- [21] R. Mohammadpour, A. Irajizad, A. Hagfeldt, G. Boschloo. *Phys. Chem. Chem. Phys.* 13 (2011) 21487.
- [22] W. Peng, M. Yanagida, L. Han, S. Ahmed. *Nanotechnology* 22 (2011) 275709.
- [23] K. M. Lee, V. Suryanarayanan, J. H. Huang, K. R. J. Thomas, J. T. Lin, K. C. Ho, *Electrochim. Acta* 54 (2009) 4123.
- [24] J. Sheng, L. Hu, S. Xu, W. Liu, L. Mo, H. Tian, S. Dai. *J. Mater. Chem.* 21 (2011) 5457.
- [25] K. Keis, J. Lindgren, S.E. Lindquist, A. Hagfeldt. *Langmuir* 16 (2000) 4688.
- [26] K. Keis, E. Magnusson, H. Lindström, S.E. Lindquist, A. Hagfeldt. *Solar Energy Materials and Solar Cells* 73 (2002) 51.
- [27] W. Chen, Y. Qiu, S. Yang. *Phys. Chem. Chem. Phys.* 12 (2010) 9494.
- [28] T. Stergiopoulos, A. Ghicov, V. Likodimos, D. S. Tsoukleris, J. Kunze, P. Schmuki, P. Falaras. *Nanotechnology* 19 (2008) 235602.

- [29] H.J. Koo, Y. J. Kim, Y. H. Lee, W. I. Lee, K. Kim, N.-G. Park. *Adv. Mater.* 20 (2008) 195.

## Chapter 5

### Technological processes for LiBs fabrication and characterization

In this chapter all the technological steps for the fabrication and characterization of Li-Ions microbatteries was reported.  $\text{TiO}_2$  and  $\text{ZnO}$  anodes were obtained by anodic oxidation and sputtering deposition combined with thermal oxidation respectively and implemented into LiBs. The devices were electrically characterized and the charge transport properties deeply investigated.

#### 5.1 Cell components and assembling

The electrodes for the evaluation of the electrochemical properties have been prepared by growing or depositing metal-oxide nanostructures onto metal foils: Ti foil for  $\text{TiO}_2$  Nts array and stainless steel sheet for coral-shaped  $\text{ZnO}$ . Their fabrication is discussed in the next paragraphs.

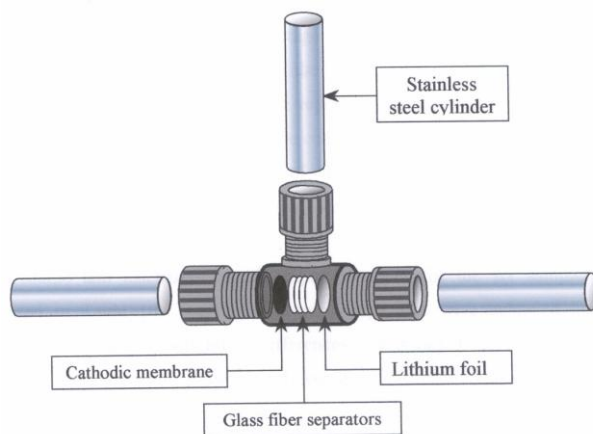


**Fig 5.1** Schematic picture of the three-electrodes test cell [1].

After their transfer in an Ar-filled dry glove-box, the disks are weighted before their use in the test cells and, by subtraction of the average weight of the Ti or SS disks, the weight of the coating semiconductor is calculated. The electrodes are used in three electrodes T-cells with

lithium metal (high purity lithium foils, Merck) as both the counter and the reference electrodes and two glass-wool (Whatman GF/A) discs as the separator. The so-called T-cell (see Fig. 5.1) is composed of a polyethylene T-shaped body in which three 304 stainless-steel cylinders with a diameter of 10 mm can be inserted.

The procedure of T-cell assembly has been performed in the dry box as follows. A lithium foil is attached on the side of a stainless-steel cylinder by applying a slight pressure on it, and the cylinder is then inserted into the T-cell through one of the two facing holes. From the opposite side two discs of carefully dried glasswool are inserted as separator before adding the cathodic membrane electrode and the second stainless-steel cylinder. The two cylinders are then tightened, and the holes are sealed using two threaded rings. Through the third central hole, the electrolytic solution is poured inside the cell before the last cylinder is inserted, allowing the excess electrolyte to exit, and finally sealed. For cyclic voltammetry experiments, the third cylinder is provided with an attached lithium foil as the reference electrode. This kind of container is air tight after a careful sealing, which allows the transfer of the cell outside the dry glove-box for the electrochemical measurements. The liquid electrolyte used is 1M LiPF<sub>6</sub> solution in a 1:1 mixture of ethylene carbonate (EC) and diethyl carbonate (DEC) [1].

## 5.2 Device characterization

The electrochemical response in liquid electrolyte of the samples was tested in polypropylene three-electrode T-cells assembled as follows: a TiO<sub>2</sub> NTs disk (area 200  $\mu\text{m}^2$ ) as the working electrode, a 1.0 M lithium perchlorate (LiClO<sub>4</sub>, Aldrich) in a 1:1 w/w mixture of ethylene carbonate (EC, Fluka) and diethyl carbonate (DEC, Aldrich) electrolyte solution soaked on a Whatman<sup>®</sup> GF/A separator and a lithium metal foil (high purity lithium foils, Chemetall Foote Corporation) as the counter electrode. For cyclic voltammetry (CV), a lithium foil was added at the third opening, in direct contact to the electrolyte, acting as the reference electrode.

Galvanostatic discharge/charge cycling tests (cut off potentials: 1.0–3.0 V vs. Li) and CVs (between 1.0 and 3.0 V vs. Li, different scan rates from 0.05 to 1.00 mV s<sup>-1</sup>) were carried out at ambient temperature on an Arbin Instrument Testing System model BT-2000. The discharge/charge cycles were set at the same rate ranging from 0.12C and 12C. Note that 1C corresponds to 0.08 mA with respect to a TiO<sub>2</sub> active mass of about 0.25 mg. To confirm the results obtained, the tests were performed at least three times on different fresh samples. Clean electrodes and fresh samples were used for each test. Procedures of cell assembly were performed in the inert atmosphere of a dry glove box (MBraun Labstar, O<sub>2</sub> and H<sub>2</sub>O content < 0.1 ppm) filled with extra pure Ar 6.0.

Electrochemical impedance spectroscopy (EIS) analysis was carried out through an electrochemical workstation (model 760D, CH Instruments) in three-electrodes configuration (using Li discs as both the reference and the counter electrodes) at different applied bias potentials in the frequency range between 100 kHz and 100 mHz (AC signal amplitude of 10 mV). The experimental data of EIS were fitted using an equivalent circuit in order to obtain information about the transport properties of NTs.

## 5.3 Anodes fabrication

### 5.3.1 TiO<sub>2</sub> nanotubes

As previously described in chapter 3, a very fast two-step electrochemical treatment (i.e., 20 min) led to the formation of densely packed TiO<sub>2</sub> NT carpet on Ti foil. The samples were then

rapidly annealed at 450 °C for 30 min to obtain the crystallisation of the material in the anatase phase directly onto the Ti foil. The length of the tubes was found to be approximately 6  $\mu\text{m}$  with external and internal diameters around 110 and 70 nm, respectively. In Figure 5.2a,b the cross sectional views of the crystallised  $\text{TiO}_2$  NTs carpet at different magnifications are presented.

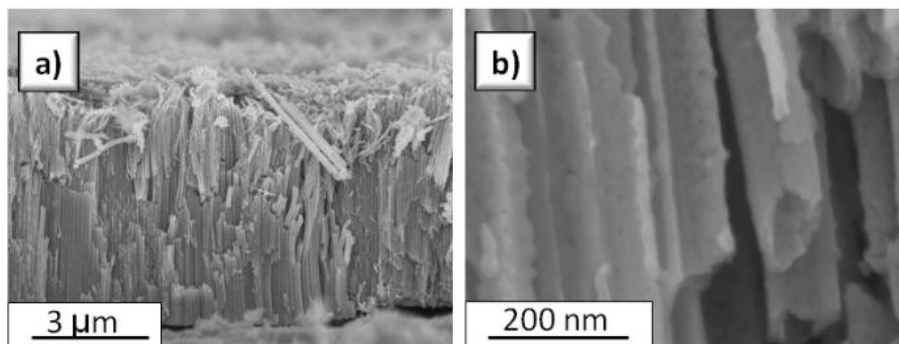


**Fig. 5.2** FESEM micrographs showing the cross sections of the NTs carpet at different magnifications

### 5.3.2 Sponge-like ZnO

The electrodes were fabricated by synthesizing sponge-like ZnO films onto circular stainless-steel (SS-316) substrates with an area of 0.78  $\text{cm}^2$ . The method adopted for the synthesis of the ZnO films consisted of the two-step procedure described in details in chapter 3. The deposition time was chosen to be 60 min, which resulted in 1  $\mu\text{m}$  thick films. The obtained ZnO samples were then thermally treated in a muffle furnace at a temperature of 380 °C for 30 min statically in ambient air.

FESEM micrographs reported in Fig. 5.3 show the characteristic morphology of the as-annealed ZnO film deposited on silicon substrate, observed in cross-section, while the inset report the top view.

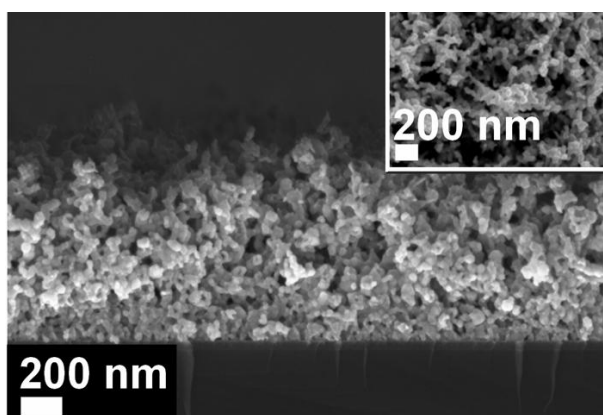


**Fig. 5.3** FESEM micrographs showing the morphology of the as-oxidized sponge-like ZnO films on silicon with thickness of 1 micrometer. The inset report the top view of the films.

## 5.4 Results and discussion

### 5.4.1 TiO<sub>2</sub> nanotubes

The evaluation of the electrochemical performances in laboratory scale lithium test cells was carried out at ambient temperature by means of cyclic voltammetry (CV), galvanostatic discharge/charge cycling at various current regimes and electrochemical impedance spectroscopy.

The cyclic voltammograms of the annealed sample (initial 10 cycles), performed at the scan rate of 0.05 mV s<sup>-1</sup> between 1.0 and 3.0 V vs. Li, show the behaviour expected on the basis of the following equation [2]:

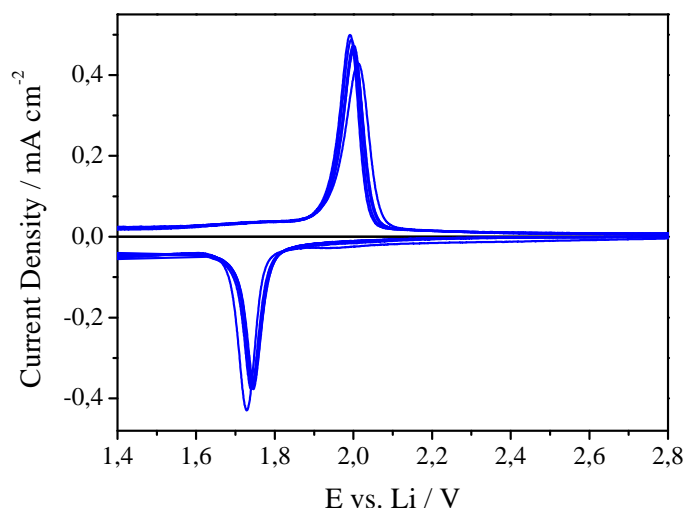
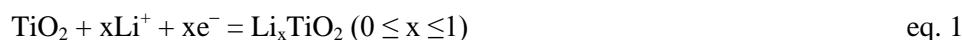


**Fig. 5.4** Cyclic voltammetry (cycles 1-10) of anatase TiO<sub>2</sub> NTs in 1.0 M LiClO<sub>4</sub> in 1:1 w/w EC:DEC with a scan rate of 0.05 mV s<sup>-1</sup> in the potential range of 1.0–3.0 V vs. Li.

In particular, the reduction/oxidation peaks appeared sharp and the Ti<sup>(IV)</sup>/Ti<sup>(III)</sup> redox couple was found to be centred at an average potential of about 1.8 V vs. Li, where lithium insertion/deinsertion process takes place. Looking at the symmetry of the CV curves reported in Fig. 5.4, we can confirm the very similar Li-ion insertion/deinsertion capability inside the nanotubes, revealing a good reversibility of the process. Moreover, the shape and position of the peaks were very similar and no appreciable change in the redox peak positions was evidenced during prolonged voltammetric cycling. This data confirmed the high stability of the materials towards reactivity with Li<sup>+</sup> ions.

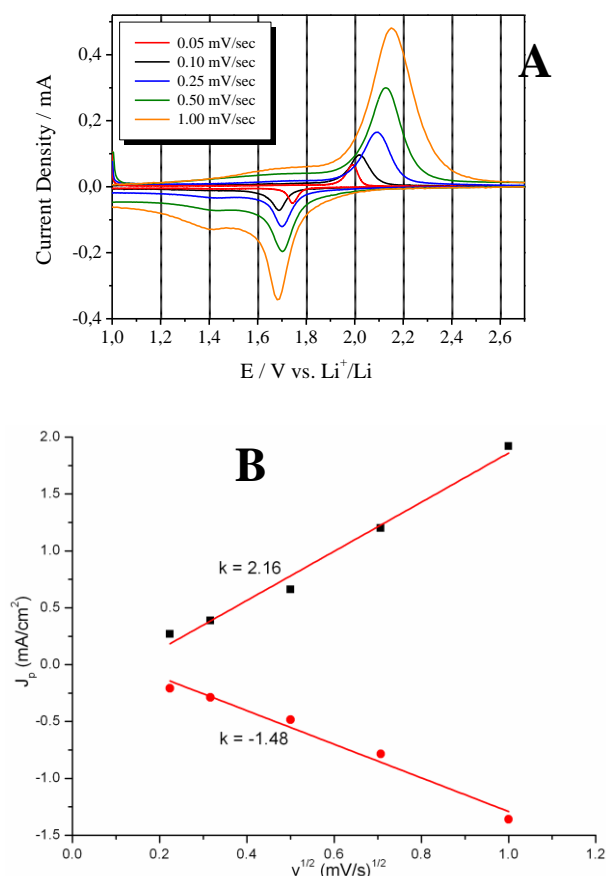


**Fig. 5.5** (a) CV analysis at different scan rates of anatase TiO<sub>2</sub> NTs in 1.0 M LiClO<sub>4</sub> in 1:1 w/w EC:DEC at ambient temperature, (b) cathodic and anodic peak current density dependence on the scan rate for the TiO<sub>2</sub> NT arrays. Each measure is done on fresh electrodes.

In addition, in order to evaluate the diffusion coefficient of Li<sup>+</sup> ions inside the TiO<sub>2</sub> nanotubes, which is a fundamental factor in order to achieve high rate capabilities, various CV measurements were performed at different potential scan rates, ranging from 1.0 to 0.05 mV s<sup>-1</sup>, on fresh anatase NT carpets (see Fig. 5.5a). Since the reaction kinetics during CV measurements is governed by the diffusion of the charges, the oxidation and reduction peak current densities  $J_p$  measured at different scan rates  $v$  are proportional to the square root of scan rate itself, as expressed by the following equation (eq. 2):

$$J_p = 2.69 \times 10^5 n^{3/2} C_0 D^{1/2} v^{1/2} = k v^{1/2} \quad \text{eq. 2}$$

where  $n$  is the number of electrons per molecule during intercalation,  $C_0$  is concentration of lithium ions and  $D$  is the diffusion coefficient of Li<sup>+</sup>. The constant  $k$  (related to the diffusion of lithium ions) can be evaluated by the slope of the  $J_p$ - $v^{1/2}$  curve reported in Fig. 5.5b.  $k$  values equal to 2.16 and 1.48 were found out for oxidation and reduction reactions, respectively,

which are much higher than those previously reported in literature [2, 3], thus indicating a highly efficient intercalation of  $\text{Li}^+$  ions into the anatase NT array.

The galvanostatic discharge/charge cycling behaviour of anatase  $\text{TiO}_2$  NT arrays at ambient temperature and at different current regimes is shown in Fig. 5.6(a-c).

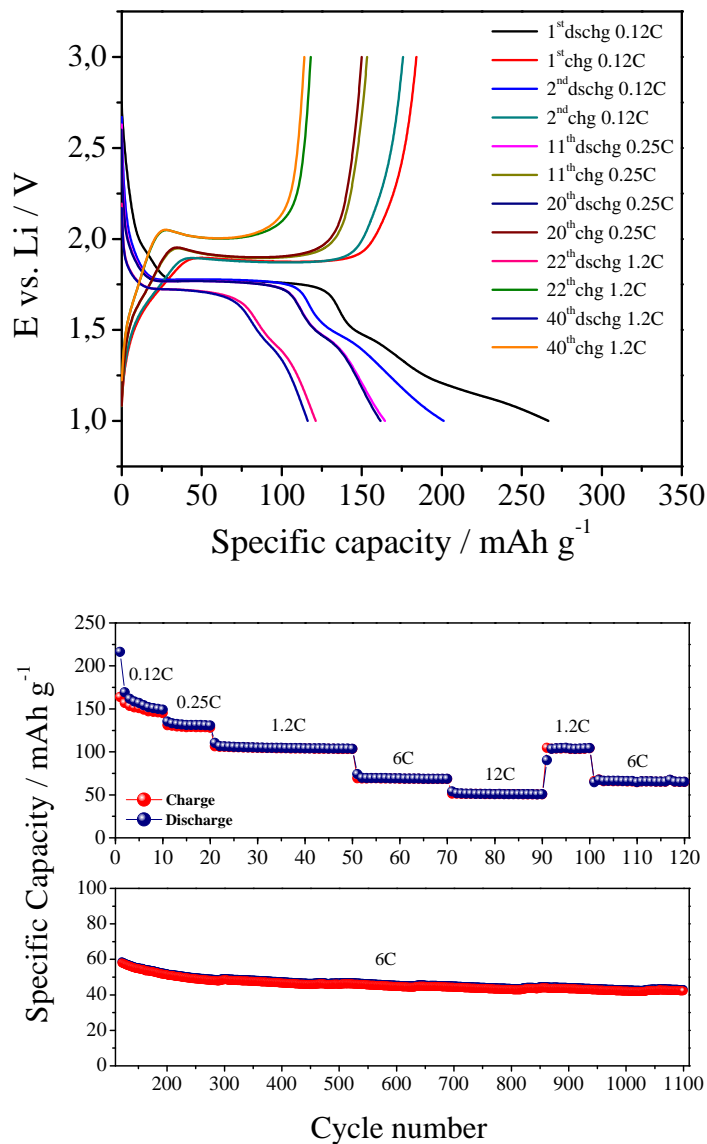


**Fig. 5.6** Typical ambient temperature galvanostatic discharge/charge cycling test of the  $\text{TiO}_2$  NTs based lithium cell, at different C-rates (from 0.12C to 12C): a) current vs. time profiles at various current regimes, b) specific discharge/charge capacity vs. cycle number, c) durability test at high 6C current regime.

The electrochemical process of this cell is the reversible removal-uptake of lithium ions to and from the  $\text{TiO}_2/\text{Li}_x\text{TiO}_2$  active materials (see eq. 1), which is expected to develop along an

average 1.8 V vs. Li flat plateau. This is shown in plot a) of Fig. 5.6 which depicts some typical current vs. time profiles: they clearly show the characteristic shape of anatase phase as reported in the literature [2]; in particular, in good accordance with the CV results, we can observe potential discharge/charge plateaus in the 1.9-1.75 V vs. Li range, that are attributed to the Li reversible insertion/deinsertion process between the tetrahedral and octahedral sites, typical of annealed TiO<sub>2</sub> nanotubes. The difference between discharge and charge potential values only slightly increases with the increase in the applied current, thus accounting for both limited internal resistance at the electrode/electrolyte interface and limited cell overpotential contributions. Plot b) in Fig. 5.6 shows the specific capacity vs. cycle number at ambient temperature and at different current rates from low 0.12C to very high 12C current regimes. The initial specific capacity approaches 170 mAh g<sup>-1</sup> at low 0.12C rate. The capacity retention is satisfactory: at 1.2C current rate the cell still delivers specific capacity values higher than 105 mAh g<sup>-1</sup>, while around 75 and approaching 60 mAh g<sup>-1</sup> at 6C and 12C current rates, respectively. Thus, the cell operates with the expected potential profiles delivering a sufficient fraction of the theoretical capacity even at very high rates as high as 12C. The decrease in the specific capacity observed when increasing the current rate can, in general, be ascribed to limitations in the Li<sup>+</sup> ion diffusion and in the electron transport through the porous nature of the active material grains. However, if one considers that the electrode prepared here consists of bare TiO<sub>2</sub> NTs with no addition of electronic conductivity enhancer during their preparation, the cycling performance appears highly valuable, particularly at very high C-rates. Finally, it is important to note that the system behaves correctly, with no abnormal drift even at high regimes; in fact, reducing the C-rate the specific capacity is completely restored (see, in Fig. 5.5b, the specific capacity values from 12C to 1.2C after the 90<sup>th</sup> cycle).

In order to confirm the stability of the electrodes and, particularly, to study the transfer rate of Li<sup>+</sup> into the TiO<sub>2</sub> nanotubes, electrochemical impedance spectroscopy measurements were performed during the first stages of cycling: after fabrication, after the first discharge cycle, after the first charge cycle, after the second discharge cycle, after the second charge cycle and finally after 5 cycles at 0.12C constant current. Fig. 5.7a shows the comparison between the impedance spectra of the fresh NTs cell, directly after assembly (measured at open circuit potential, that is about 3.0 V vs. Li), and after five galvanostatic cycles (measured at 2.4 V vs. Li); in Fig 5.7b, the spectra obtained after the first and the second discharges (measured at 1.5 V vs. Li) are presented, while the measurement after the first and the second charge processes (measured at 2.4 V vs. Li) are plotted in Fig. 5.7c. All the spectra show a semi-circle in the high-frequency range (clearly visible in the insets of each figure) that is associated to the charge transfer at the NTs-electrolyte interface, and a straight line at low frequency related with the diffusion of Li<sup>+</sup> ions into the semiconductor structure [3]. It can be noted (see Fig. 5.7a) that, after 5 cycles, the Nyquist plot presents a larger semi-circle with respect to the fresh spectrum, meaning an increased charge transfer time due to the repeated cycling; a slight increase of the high-frequency arcs is also visible after the second charge and discharge cycles (Fig. 5.7b and Fig 5.7c, respectively).

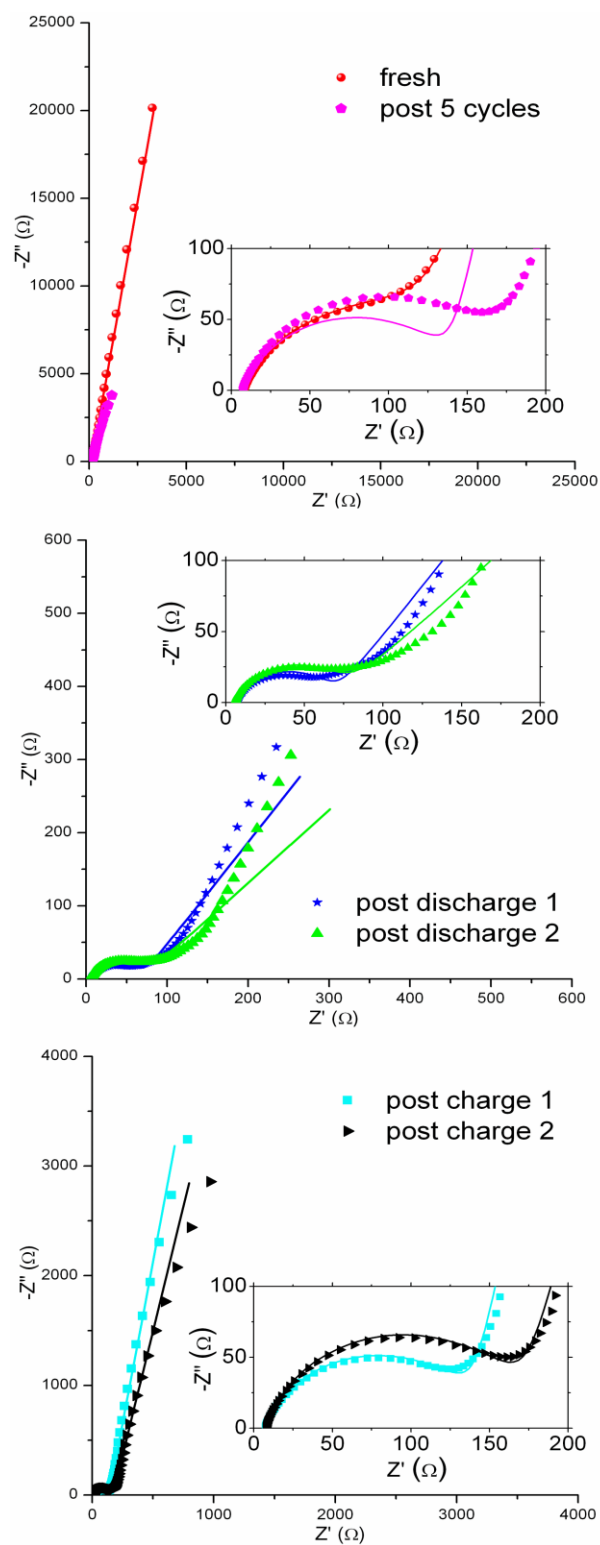


**Fig. 5.7** Measured (symbol) and fitted (solid line) EIS spectra of NT array at different stages of cycling. The high frequency zoom is reported in the inset of each figure.

It is noteworthy that the arcs related to the discharge cycles are always lower and narrower with respect to the charge ones, thus suggesting a mechanism of discharge intrinsically faster than the charge one. In order to quantitatively evaluate the charge transfer properties, the impedance spectra were fitted exploiting an equivalent circuit, consisting in a series resistance  $R_s$  (accounting for the electrolyte resistance), a parallel between the constant phase element  $Q_{dl}$  (representing the double layer capacitance at the oxide/electrolyte interface) and the resistance  $R_{ct}$  (corresponding to the charge transfer resistance) and the Warburg impedance  $W$  (associated to ion diffusion into the NTs) [4]. The resulting fitting curves are plotted in Fig. 5.7 and the evaluated parameters are reported in Table 1; in the same Table, the charge transfer time values are also presented, calculated through the following equation (eq. 3):

$$\tau_{ct} = (Q_{dl} R_{ct})^{1/\beta} \quad \text{eq. (3)}$$

where  $\beta$  is the exponent of the constant phase element  $Q_{dl}$ . As already observed, going on with cycling, an increment of the charge transfer time is observed, due to the increase of the charge transfer resistance; the fresh sample shows a  $\tau_{ct}$  equal to 0.5 ms, that is increased to about 0.7 ms after the second charge and remains quite constant after 5 cycles.

**Table 1** EIS parameters evaluated from the fitting of the experimental curves.

<b>Sample</b>	<b>Potential (V)</b>	<b><math>Q_{dl}</math> (<math>\Omega^{-1}\cdot s^\beta</math>)</b>	<b><math>\beta</math></b>	<b><math>R_{ct}</math> (<math>\Omega</math>)</b>	<b><math>\tau_{ct}</math> (<math>\mu s</math>)</b>
<b>fresh</b>	3.0	2.05E-05	0.78	125.8	495
<b>post discharge 1</b>	1.5	4.39E-05	0.75	59.6	358
<b>post charge 1</b>	2.4	2.00E-05	0.81	131.8	629
<b>post discharge 2</b>	1.5	4.61E-05	0.76	73.4	556
<b>post charge 2</b>	2.4	1.47E-05	0.83	163.0	697
<b>post 5 cycles</b>	2.4	1.44E-05	0.83	166.0	702

The very good stability and integrity of the nanostructured active material was confirmed in the durability test at high 6C current rate shown in Fig. 5.7c. A slight decrease of the specific capacity can be observed with cycling, though the decreasing degree is very limited (< 25 % after 1100 cycles). Thus, we demonstrated that vertically aligned  $TiO_2$  NTs prepared by anodic oxidation followed by rapid annealing can perform in lab-scale lithium cell up to > 1100 cycles with stable performance and good reversibility of discharge/charge process.

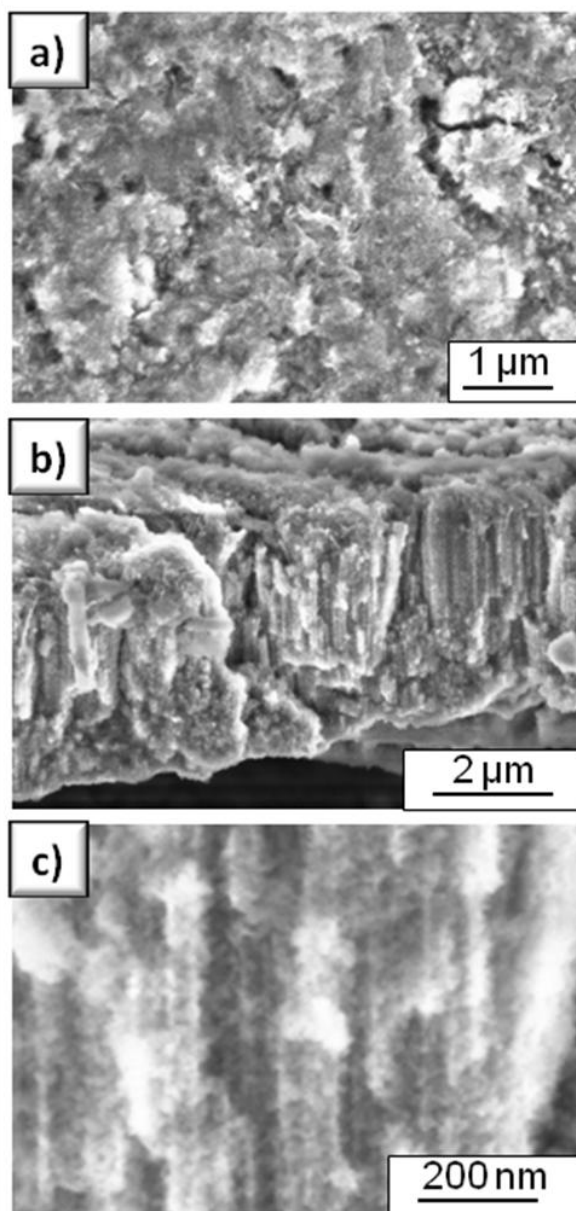


**Fig. 5.8** FESEM micrographs at different magnifications showing the top (a) and cross (b-c) morphology of the NTs sample after > 1100 repeated discharge/charge cycles in lithium cell.

Furthermore, the structural stability after long-term cycling of the NTs was found to be very good, with no pulverization of the electrode and/or no major damage to the electrode surface, as confirmed by FESEM analysis after the electrochemical durability test; the corresponding micrographs after > 1100 repeated discharge/charge cycles in liquid electrolyte are shown in Fig. 5.8. It is clearly evident that the original tubular morphology is mostly maintained, with no sign of huge fractures and/or pulverization of the electrode. Therefore, no deterioration of the electrical contact between the NT layer and the underlying metallic Ti substrate after the discharge/charge process should have happened, thus accounting for the very good stability during very long term cycling.

### 5.4.2 Sponge-like ZnO

In this section, the evaluation of the electrochemical behaviour in laboratory scale lithium test cells will be shown, to demonstrate that sponge-like ZnO nanostructures can be suitable as a promising Li-ion battery negative electrode.

**Fig. 5.9** shows the cyclic voltammetric profiles of the as-prepared sponge-like ZnO film vs. lithium metal between 0.02 and 3 V vs. Li under a constant scan rate of  $0.1 \text{ mV s}^{-1}$ . It shows the typical electrochemical behaviour towards Li of ZnO expected on the basis of previous reports [5]. In particular, the following equations are expected during the first cathodic scan towards 0.02 V vs. Li:



Thus, the formation of Zn metal and  $\text{Li}_2\text{O}$  (eq. 4) is followed by the formation of LiZn alloy (eq. 5) along with different minor irreversible processes. This reflects in the first cathodic CV profile, where at below 1.0 V vs. Li the reduction of ZnO into Zn occurs along with the growth of the SEI (solid electrolyte interphase) layer, that is the gel-type layer which deposits at the surface of the Zn nanoparticles upon the decomposition some of the electrolyte components [6]. The potentials at which these reactions take place are very close, thus only one broad intense peak is clearly visible centred at approx. 0.5 V vs. Li, along with a shoulder at about 0.75 V vs. Li. The LiZn alloy formation occurs at below 0.2 V vs. Li, as reflected by the corresponding peak in the CV profile during cathodic scan. In the subsequent anodic scan towards 3.0 V vs. Li, different oxidation peaks are observable, located in the 0–0.7 V vs. Li range, which are ascribed to the average potentials of the multi-step process of LiZn dealloying [5,6], finally leading to metallic zinc. The broad peak ranging from below 1.0 to slightly above 2.0 V vs. Li could be eventually ascribed to the formation of ZnO by the conversion reaction between  $\text{Li}_2\text{O}$  and Zn, even if controversial reports can be found in the literature [5,6]. After the first cycle, the curves tend to stabilise in shape and intensity of the redox peaks, accounting for more reversible electrode reactions.

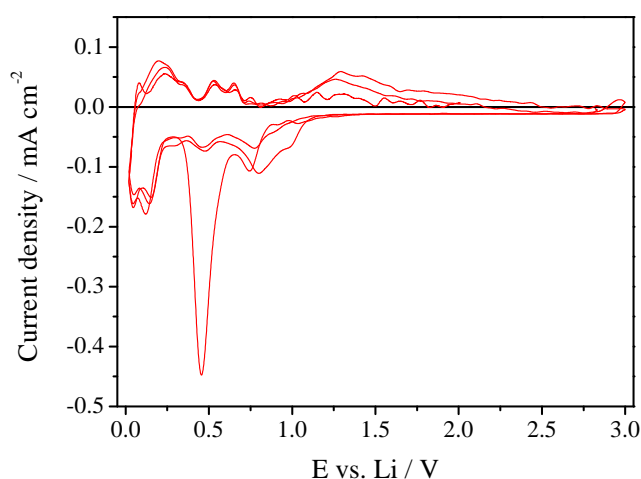


**Fig. 5.9** Cyclic voltammetry curves of ZnO in 1.0 M  $\text{LiClO}_4$  solution in 1:1 v/v mixture of EC/DEC with a scan rate of  $0.1 \text{ mV s}^{-1}$  in a voltage range of 0.02 – 3 V vs. Li.

To evaluate the electrochemical performance of our sponge-like zinc oxide film, the potential vs. time profiles (and corresponding specific capacity vs. cycle number plot) were obtained for an “oxide on stainless steel/Li” two-electrodes test cell cycled in the potential range between 0.02 and 3.0 V (versus Li/Li<sup>+</sup>) at constant 0.1 mA current ( $\sim 0.6$  C) for 100 cycles, in liquid electrolyte (1.0 M LiClO<sub>4</sub> solution in 1:1 v/v mixture of EC/DEC). The resulting behaviour is shown in the two plots (a and b) of Fig. 5.10. Plot a) shows the discharge/charge cycling profiles of our as-prepared sponge-like ZnO nanostructures. The profile well describe the presence of different steps related to the phase transitions involved in the Li insertion/de-insertion and the LiZn alloy formation.

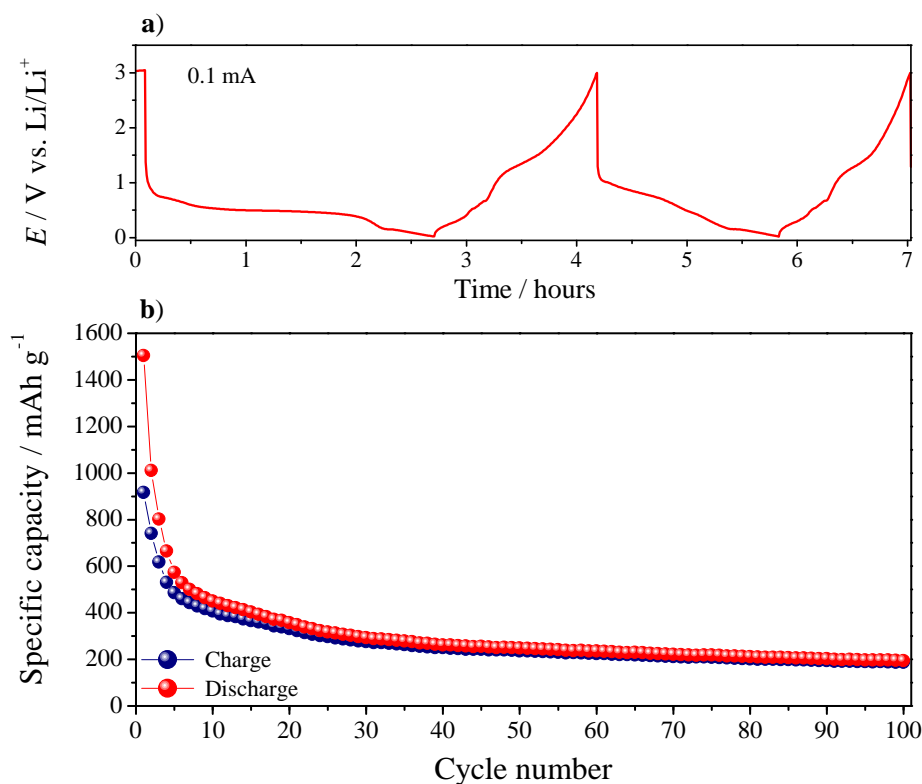


**Fig. 5.10** Typical ambient temperature galvanostatic discharge/charge cycling test of the sponge-like ZnO-based lithium cell, at 0.1 mA current ( $\sim 0.6$  C rate) in the 0.02 - 3 V vs. Li range: a) initial potential vs. time profiles, b) specific discharge/charge capacity vs. cycle number.

The first discharge curve, after an initial shoulder at above 0.7 V vs. Li, shows a large plateau at about 0.5 V vs. Li accompanied by a little but well-defined plateau below 0.2 V vs. Li. When ZnO active material nanoparticles are electrochemically discharged with Li metal, the destruction of the crystal structure occurs followed by the formation of metallic zinc nanoparticles and Li<sub>2</sub>O (eq. 1). In accordance with the results shown by CV analysis, this process gives rise to the large potential plateau above mentioned. Upon deep discharge, Zn can further react with Li to form a Li-Zn alloy (1:1) (eq. 2). The experimentally observed specific capacity upon the first deep discharge was 1504 mAh g<sup>-1</sup>, which much higher with respect to the theoretical specific capacity of about 978 mAh g<sup>-1</sup>. The extra lithium inventory consumption can be easily ascribed to the SEI layer formation [6]. During the following first

charge process, both the reverse reaction of eq. 2 and the partially reversible reaction of eq. 1 mainly occur [7, 8], even if the plateaus are less evident and 4 different slopes can be observed. The specific capacity delivered was  $917 \text{ mAh g}^{-1}$ , much lower than the first discharge in which some irreversible processes occur but approaching the theoretical value. After the first complete discharge/charge cycle, the profiles and plateaus (i.e., two-phase equilibrium in the material) are similar in shape, indicating that the reactions become more reversible, well matching the previous reports [5, 9]

As clearly evident in plot b) of Fig. 5.10 showing the prolonged cycling test of our sponge-like ZnO nanostructures, a huge capacity fade is clearly observable during the initial cycles, followed by a progressive slight decrease during cycling. In fact, even though the first discharge and charge capacities were found to be high, its reversible capacities fade rapidly: only about 38 % of the initial discharge capacity and 53 % of the initial charge capacity are retained at the end of the initial cycles. This fast capacity decay is typical of nanostructured ZnO materials, as shown by the results reported in the literature for nanostructures prepared by different routes [6, 9]. Nevertheless, by comparison with previous reports, is apparent that our sponge-like system exhibits a better initial capacity retention. After the initial cycles, a good reversibility of the electrochemical redox processes is observed.

As already stated by our research group for similar systems [10, 11], the expansion and shrinkage of the structure caused by the electrochemical redox reactions with lithium are difficult to accommodate, leading to strong stresses that may affect the electrode integrity and, consequently, the electrochemical performance. This was confirmed by FESEM analysis after cycling, the results of which are shown in Fig. 5.11. As clearly evident, the electrode surface appeared to be dramatically altered after only 10 complete cycles (image a) and the original film morphology has almost disappeared.

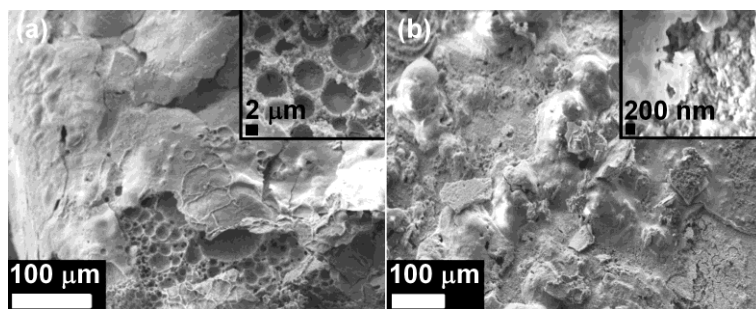


**Fig. 5.11** FESEM micrographs showing the surface morphology of (a) 1 µm thick ZnO film after 10 cycles and (b) after 100 cycles. The insets report some details of the surface at higher magnifications.

A double-layered structure was formed, the uppermost being composed of dense ZnO (confirmed by EDX analysis). This is in agreement with the observations reported by Kushima and co-workers [12], who stated that ZnO single-crystal nanowires were transformed into a nano-glass having multiple glassy nano-domains by a three-step reaction mechanism. An initial partial lithiation which induces multiple nano-cracks, thus dividing the NWs into multiple segments, is followed by rapid surface diffusion of lithium ions leading to a solid-state amorphisation along the open crack surface, which finally merge, leaving behind a glassy surface. This phenomenon is indicated as the main precursor to the electrochemically driven solid-state amorphisation in ZnO. On the contrary, the underlying surface is mainly composed of a residual film of nanostructured ZnO that however appeared less porous than in the as-

grown film (see for comparison the micrograph reported in Fig. 5.3). The SS-316 current collector surface was found to be also partially exposed, as can be observed in the inset of Fig. 5.11a where the circular holes formed at the surface are surrounded by nanostructured ZnO structures. The mechanical degradation of the electrode is thought to be determinant for the huge drop in electrochemical yielding, as it happens in bulk electrodes, most probably leading to a loss of electrical contact between all the isolated islands which can correspondingly induce a lower active area for the  $\text{Li}^+$  ions to enter inside the structure.

In the following cycles, the degradation process somewhat stabilized (see Fig. 5.11b which depicts the surface morphology of the electrode after 100 galvanostatic discharge/charge cycles) and the electrode morphology suffers no major modifications. In any case, no pulverization of the electrode could be observed, thus accounting for the almost stable cycling behaviour after the initial 50 complete cycles at around  $200 \text{ mAh g}^{-1}$  of reversible specific capacity.

## 5.5 References

- [1] C. Gerbaldi, Ph.D. Thesis “Mesoporous materials and nanostructured  $\text{LiFePO}_4$  as cathodes for secondary Li-Ions batteries”, Politecnico di torino, Italy, 2005
- [2] W.H. Ryu, D.H. Nam, Y.S. Ko, R.H. Kim, H.S. Kwon. *Electrochim. Acta* 61 (2012) 19.
- [3] D. Fang, K. Huang, S. Liu, Z. Li. *Journal of Alloys and Compounds* 464 (2008) L5.
- [4] T. Yiping, T. Xiaoxu, H. Guangya, C. Huazhen, Z. Guoqu. *Electrochim. Acta* 78 (2012) 154.
- [5] X.H. Huang, X.H. Xia, Y.F. Yuan, F. Zhou. *Electrochim. Acta* 56 (2011) 4960
- [6] J. Liu, Y. Li, X. Huang, G. Li, Z. Li. *Adv. Funct. Mater.* 18 (2008) 1448.
- [7] J.-H. Lee, M.-H. Hon, Y.-W. Chung, I.-C. Leu, *Appl Phys A* 102 (2011) 545.
- [8] Z.F. Zheng, X.P. Gao, G.L. Pan, J.L. Bao, J.Q. Qu, F. Wu, D.Y. Song. *Chin. J. Inorg. Chem.* 20 (2004) 488.
- [9] F. Belliard, P.A. Connor, J.T.S. Irvine. *Solid State Ionics* 135 (2000) 163.
- [10] A. Lamberti, M. Destro, S. Bianco, M. Quaglio, A. Chiodoni, C.F. Pirri, C. Gerbaldi. *Electrochim. Acta* 70 (2012) 62.
- [11] F. Di Lupo, A. Tuel, C. Francia, G. Meligrana, S. Bodoardo, C. Gerbaldi. *Int. J. Electrochem. Sci.* 7 (2012) 10865.
- [12] A. Kushima, X.H. Liu, G. Zhu, Z.L. Wang, J.Y. Huang, J. Li. *Nano Lett.* 11 (2011) 4535.

# Chapter 6

## Conclusions and considerations for future works

In this chapter, a broad recap of the results described in this thesis is presented. As declared in Chapter 1, the first objective of this work is devoted to the efficient synthesis of TiO<sub>2</sub> NTs membranes and ZnO sponge-like films on transparent conductive glasses in view of the evaluation of DSCs performances when these films are employed for the photoanode fabrication.

The second objective is to adapt the nanostructures developed for DSC as electrodes into LiBs, trying to overcome the limitation imposed by commonly used materials. Considerations and suggestions for future research on TiO<sub>2</sub> nanotubes, ZnO nanostructures and their integration into the studied electrochemical energy production and storage devices are also proposed.

### 6.1 Metal-oxide nanostructures

#### 6.1.1 TiO<sub>2</sub> nanotubes array

Vertically oriented TiO<sub>2</sub> NTs were obtained by anodic oxidation of a titanium foil and fully characterized in terms of stoichiometry, crystalline phase and morphology.

In order to achieve a debris-free and well ordered NTs array with open top surface and fast growth rate, NTs were synthesized in non-aqueous organic electrolytes containing ammonium fluoride and a two-step electrochemical process was implemented.

Chemical composition analysis of the NTs confirmed the optimal control of the oxide stoichiometry. The NTs array exhibited a specific surface area in line with the value measured for other TiO<sub>2</sub> nanostructures and suitable for the application in the selected electrochemical devices. TEM and XRD analysis revealed the completely amorphous nature of the NT array after anodic oxidation, while a crystalline anatase film was obtained after thermal treatment at 450 °C.

To further increase the specific surface area, that is one of the most important parameters for metal-oxide nanostructures employed as active elements into electrochemical devices, a possible strategy could be engineering the titanium foil surface via micro/nano-machining techniques. The nano/micro structuration of the substrate could also lead to improvements in

the mechanical properties of TiO<sub>2</sub> NTs membranes thanks to the compensation of internal stresses inside the film.

Additional optimization of the nanotubes by changing the anodization parameters could also lead to improvements in the material properties.

### 6.1.2 Sponge-like ZnO film

A simple method for the formation of sponge-like nanostructured zinc oxide films with a thickness up to 18 micrometers was described, starting from sputtered nanostructured zinc films. All the characterization results demonstrated that the films grown by sputtering were composed of zinc with oxide phases, likely due to the surface oxidation which occurred when exposing the samples to air, and to the presence of residual oxygen inside the vacuum chamber. XRD patterns revealed the wurtzite hexagonal structure of zinc. The optimum deposition conditions giving rise to a nanostructured zinc film with larger pores (suitable for the application in electrochemical devices) were found to be an Ar flow of 10 sccm, a RF power value of 100 W and a gas pressure of 0.67 Pa. ZnO nanostructured films were then obtained by simply treating the precursor zinc films on a hot plate in ambient air. By this method, the morphology of the zinc film is well preserved after the thermal treatment. The films showed a high density of branches, a relatively high specific area value and fine optical transmittance. TEM and XRD analysis proved the formation of pure wurtzitic polycrystalline ZnO nanostructures and no metallic phase could be detected.

In order to improve and better understand the oxidation process it could be very useful to start a complete investigation on the dependence from different temperatures and oxygen flux.

## **6.2 Dye sensitized solar cells**

### 6.2.1 TiO<sub>2</sub> nanotubes array

The integration of TiO<sub>2</sub> NTs in front-side illuminated DSC has been described: transparent photoanode were fabricated transferring a self-standing NTs membrane onto a FTO/glass sheet with an adhesion layer made of TiO<sub>2</sub> nanoparticles (commercial or produced in the CSHR@PoliTo Labs).

The approach presented for photoanode fabrication is innovative if compared to others previously reported in the literature: no chemical dissolution or mechanical splitting were involved for membrane separation and membrane crystallization/attachment steps were coupled in the same thermal treatment.

The cell performances and the electron transport properties dependence on TiCl<sub>4</sub> treatment and tube length were characterized and a maximum value for the power conversion efficiency (PCE) as high as 7.56 % was obtained for the cell fabricated with a 30 µm thick nanotube membrane treated with TiCl<sub>4</sub> bonded on FTO/glass substrate employing a TiO<sub>2</sub> sol. Information on the electron diffusion properties into the NTs was obtained by equivalent circuit fitting of the EIS (electrochemical impedance spectroscopy) spectra.

A significant increase of both electron lifetime and diffusion length values was observed for the NTs-based cell with respect to a standard TiO<sub>2</sub> nanoparticles (NPs)-based one. The improved charge collection efficiency was ascribed to the 1-dimensional structures that favor the electron transport while the reduced recombination rate (and a subsequent higher carrier lifetime value) could be attributed to the reduced presence of defects and trap-sites in the nanotubes with respect to the nanoparticles layer.

In addition, NTs were employed to fabricate composite NT/NP photoanodes by mixing NT powder into commercial NP dispersion (with different NT content). The resulting PCE was found to be higher for the composite photoanodes with respect to the NP-based one thanks to higher values of short circuit current density. The enhancement of  $J_{SC}$  was ascribed to a most efficient charge collection efficiency and to the scattering effect caused by the NT included into the NP network. Moreover, an increase of the electron lifetime was observed in the NT/NP photoanode by means of EIS analysis, accounting for a reduced number of trap sites with respect to the NP film.

The liquid electrolyte usually employed in DSC is still a drawback for long-term practical operation and causes substantial problems in bringing DSSC onto market. Solid-state flexible DSCs represent one of the most interesting proposed devices in the photovoltaic field. Coupling  $TiO_2$  nanotubes with a polymer electrolyte can lead to numerous advantages with respect to nanoparticle based electrode. NTs, due to their open structure, should allow the polymer electrolyte to easily penetrate inside the film, thus increasing the interfacial contact between the nanotubes/dye and the electrolyte. Moreover, the nanopores may provide preferential pathways for the quick diffusion of charges into the electrolyte.

### 6.2.2 Sponge-like ZnO film

High efficient ZnO-based DSCs were fabricated studying the dependence of the cell efficiency upon the dye incubation time, the chemical characteristics of the incubation solution and the film thickness. I-V electrical measurements showed an improvement in the overall solar cell efficiency from 1.90 % to 5.25 %, thanks to a controlled dye-sensitization procedure for different film thicknesses, as confirmed from IPCE (incident photon-to-current efficiency) measurements. EIS analysis and data modeling provided a much better understanding of the electron transfer processes at the ZnO/dye/electrolyte interface evidencing a high charge lifetime and diffusion coefficient values. A reduced recombination rate and an increased diffusion length with respect to a standard  $TiO_2$  nanoparticle-based DSC were achieved thanks to a more direct pathway for the electron collection.

The development of efficient flexible electrodes for DSCs can open new perspectives towards the integration of solar harvesters as active elements in low power electronics for small portable power sources. The biggest issue towards the fabrication of plastic-based devices is the development of binder-free nanostructured metal oxide layers, avoiding the high temperature treatment required for the sintering process in conventional nanocrystalline photoanodes. Low temperature water treatment is considered a way to overcome the limitation imposed by the thermal step, obtaining partial oxidation starting from Zn nanostructures.

In alternative, the fabrication of flexible photoanodes exploiting the same thermal process described in this work but depositing the ZnO nanostructures onto high-temperature resistant polymeric substrate (for example polyimide sheet) can be explored.

## **6.3 Li-ion batteries**

### 6.3.1 $TiO_2$ nanotubes array

Vertically oriented  $TiO_2$  nanotube arrays were tested for their electrochemical behaviour in lithium test cells. The results obtained by galvanostatic discharge/charge cycling at ambient temperature were found to be highly satisfying, particularly at very high current regimes: in fact, at a very high 6 C rate, both upon discharge and charge, the lithium cell having the  $TiO_2$

nanotubes as working electrode provided a stable specific capacity, with very high capacity retention after very long-term cycling (up to > 1100 cycles). Thus, high surface area, 1-D feature and good transport properties of the TiO<sub>2</sub> NTs led to interesting electrochemical performances.

In the next future, the present findings, along with the use of a proper solid polymer membrane as electrolyte, can surely provide a new and easy approach to fabricate nanostructured films with superior performance for the next generation of all-solid 3D micro and/or thin film Li-based cells.

### 6.3.2 Sponge-like ZnO film

The testing on ZnO sponge-like nanostructures as anode in lithium test cells showed a noticeable capacity fade occurring during the initial cycles, even though the first discharge and charge capacities were found to be high, followed by a progressive slight decrease upon prolonged cycling. Although this fast capacity decay is typical of nanostructured ZnO materials, that the prepared sponge-like system apparently exhibited a better initial capacity retention. After the initial cycles, a good reversibility of the electrochemical redox processes was observed, as confirmed by the increase in Coulombic efficiency which rapidly increased to above 90 % and, then, stabilized to above 96 % after the initial 50 cycles.

The expansion and shrinkage of the structure caused by the electrochemical redox reactions with lithium are difficult to accommodate, particularly in zinc oxide structures, leading to strong stresses that may affect the electrode integrity and, consequently, the electrochemical performance. This problem could be partially overcome by using a polymer electrolyte membrane separator and/or selecting a novel approach for the production of core-shell ZnO/C and/or ZnO/SnO<sub>2</sub> nanostructures.

*The energy harvesting and storage approaches proposed in this work are developed as independent technologies but they can be used together as a power system. Traditionally, a power pack is based on a silicon solar panel and a solid-state lithium battery considered as two independent devices, and the resulting one is heavy and not flexible. In order to combine them, hybridizing energy harvesting and storage units as an integrated power pack based on same nanostructured substrates could be a valuable strategy to obtain a portable and high-density energy system.*

## **6.3 List of publications related with this research project**

### Submitted:

**A. Lamberti**, N. Garino, A. Sacco, S. Bianco, D. Manfredi and C. Gerbaldi

Vertically aligned TiO<sub>2</sub> nanotube array for high rate Li-based micro-battery anodes with improved durability

Submitted to *Electrochimica Acta* (resubmitted after minor revision)

**A. Lamberti**, A. Sacco, S. Bianco, D. Manfredi, M. Armandi, M. Quaglio, E. Tresso and C. F. Pirri

An easy approach for the fabrication of TiO<sub>2</sub> nanotube-based transparent photoanodes for Dye-sensitized Solar Cells

Submitted to Solar Energy (resubmitted after minor revision)

**A. Lamberti**, A. Sacco, S. Bianco, M. Quaglio, D. Manfredi, C. F. Pirri  
Enhancement of electron lifetime in Dye-sensitized Solar Cell using anodically grown TiO<sub>2</sub>  
nanotube/nanoparticle composite photoanodes,  
Submitted to Microelectronic Engineering (resubmitted after minor revision)

G. Cicero, G. Musso, **A. Lamberti**, B. Camino, S. Bianco, D. Pugliese, F. Risplendi, A.  
Sacco, N. Shahzad, A. M. Ferrari, B. Ballarin, C. Barolo, E. Tresso, G. Caputo  
Combined experimental and theoretical investigation of the hemisquaraine/ TiO<sub>2</sub> interface for  
DSCs  
Submitted to Energy and Environmental Science (resubmitted after major revision)

R. Gazia, P. Motto, S. Stassi, A. Sacco, A. Virga, **A. Lamberti**, G. Canavese  
Photodetection and piezoelectric response from hard and flexible sponge-like ZnO-based  
structures  
Submitted to Nanoscale (under review)

Accepted:

**A. Lamberti**, A. Sacco, D. Hidalgo, S. Bianco, D. Manfredi, M. Quaglio and Candido F. Pirri  
TiO<sub>2</sub> nanotube array as efficient transparent photoanode in Dye-sensitized Solar Cell with  
high electron lifetime, Acta Physica Polonica A 2013

A. Sacco, **A. Lamberti**, I. Berardone, S. Bianco, R. Gazia, D. Pugliese, M. Quaglio, E.  
Tresso, C. F. Pirri Spongelike porous ZnO photoanodes for highly efficient Dye Sensitized  
Solar Cells, Acta Physica Polonica A 2013

F. Cappelluti, S. Ma, D. Pugliese, A. Sacco, **A. Lamberti**, G. Ghione and E. Tresso  
Consistent static and small-signal physics-based modeling of DSCs under different  
illumination conditions  
Phys. Chem. Chem. Phys. 2013

R. Gazia, G. Canavese, A. Chiodoni, **A. Lamberti**, S. Stassi, A. Sacco, S. Bianco, A. Virga,  
E. Tresso, C. F. Pirri  
Novel spongelike nanostructured ZnO films: properties and applications,  
Journal of Alloys and Compounds 2013

In press:

**A. Lamberti**, A. Sacco, S. Bianco, D. Manfredi, F. Cappelluti, S. Hernandez, M. Quaglio and  
C.F. Pirri Charge transport improvement employing TiO<sub>2</sub> nanotube array as front-side  
illuminated Dye-sensitized Solar Cell photoanode Phys. Chem. Chem. Phys., 2012 doi:  
10.1039/C2CP41788J

**A. Lamberti**, R. Gazia, A. Sacco, S. Bianco, M. Quaglio, A. Chiodoni, E. Tresso and C.F.  
Pirri Coral-shaped ZnO nanostructures for dye-sensitized solar cell photoanodes, Progress in  
photovoltaics: research and application, 2012 doi: 10.1002/pip.2251

Published:

**A. Lamberti**, M. Destro, S. Bianco, M. Quaglio, A. Chiodoni, C.F. Pirri and C. Gerbaldi  
Facile fabrication of cuprous oxide nanocomposite anode films for flexible Li-ion batteries via thermal oxidation  
Electrochimica Acta, (2012) 70:62

R. Gazia, A. Chiodoni, S. Bianco, **A. Lamberti**, M. Quaglio, A. Sacco, E. Tresso, P. Mandracci, C. F. Pirri. An easy method for the room-temperature growth of spongelike nanostructured Zn films as initial step for the fabrication of nanostructured ZnO,  
Thin Solid Films (2012) 524:107

A. Sacco, **A. Lamberti**, D. Pugliese, A. Chiodoni, N. Shahzad, S. Bianco, M. Quaglio, R. Gazia, E. Tresso, C. F. Pirri. Microfluidic housing system: a useful tool for the analysis of dye-sensitized solar cells components,  
Appl Phys A (2012) 109:377

A. Sacco, **A. Lamberti**, R. Gazia, S. Bianco, D. Manfredi, N. Shahzad, F. Cappelluti, S. Ma and E. Tresso. High efficiency Dye-sensitized Solar Cell exploiting sponge-like ZnO nanostructures,  
Phys. Chem. Chem. Phys. (2012) 14:16203

A. Sacco, **A. Lamberti**, M. Quaglio, S. Bianco, E. Tresso, A-L Alexe-Ionescu and C.F. Pirri  
Electric Characterization and Modeling of Microfluidic-Based Dye-Sensitized Solar Cell,  
International Journal of Photoenergy (2012) 2012:216780

**A. Lamberti**, A. Sacco, S. Bianco, E. Giuri, M. Quaglio, A. Chiodoni, E. Tresso  
Microfluidic sealing and housing system for innovative dye-sensitized solar cell architecture,  
Microelectronic Engineering (2011) 88:2308